# Theoretical and Computational Studies of the Lateral Phases on a Multicomponent Lipid-Bilayer Surface

Yongtian Luo

A dissertation
submitted in partial fulfillment of the
requirements for the degree of

Doctor of Philosophy

University of Washington

2019

Reading Committee:

Lutz Maibaum, Chair

Xiaosong Li

Bruce H. Robinson

Program Authorized to Offer Degree:
Department of Chemistry

University of Washington

## Abstract

Theoretical and Computational Studies of the Lateral Phases on a Multicomponent Lipid-Bilayer Surface

Yongtian Luo

Chair of the Supervisory Committee:
Assistant Professor Lutz Maibaum
Department of Chemistry

The lipid-bilayer membrane is the fundamental structure of a cell plasma membrane and has been largely studied by biophysical experiments, theoretical modeling and computer simulations. Two major aspects of lipid bilayer morphologies are studied, namely lateral phase separation and pattern formation (spatial organization of lipid molecules), and shape change or deformation of the membrane (undulation of the surface). In this dissertation, I apply theoretical modeling, analytical and numerical computation as well as molecular simulation to study the lateral phases on the surface of a multicomponent lipid bilayer, which is able to stay in a homogeneous state, phase separate, or transform into heterogeneous states including modulated phases and microemulsions. The focal point is a lipid-bilayer vesicle of finite size and spherical topology. I calculate phase diagrams which reveal the effects of intrinsic finite sizes of vesicles on their surface pattern and lateral phase generation. I also calculate the structure factor of vesicles, which is measured by scattering signals, and theoretically develop an approximate model-independent interconversion between the three-dimensional signal and the two-dimensional structure factor of planar membranes, and I also stress the finite size effect in this relation. It is also observed that the lipid domain formation is coupled with membrane curvature distribution on the surface. I apply the coupling through domain bending properties, and create phase diagrams in which changing

membrane mechanical properties can vary the lateral phases on a vesicle surface. In addition to the aforementioned continuum modeling, I also utilize coarse-grained molecular dynamics simulation to explore the phase behavior of asymmetric lipid bilayers consisting of a phase-separating leaflet and a homogeneous leaflet, in which the former would induce a tendency of phase separation in the latter. The molecular simulation, which keeps a record of each lipid molecule, could be a more biologically relevant model of plasma membranes.

# TABLE OF CONTENTS

# LIST OF FIGURES

# ACKNOWLEDGMENTS

I would like to thank my academic advisor, Professor Lutz Maibaum, for this opportunity to enter and work in the field of theoretical soft matter and biophysics, and also for his great support and help in the research projects. Also I would like to thank the other members of the Maibaum group, both past and present, from whom I have learned a lot in this process. And I would like to thank the members of the Amphiphiliphiles (Schick and Keller groups) and Theory Suite groups (Li, Masiello and McCoy groups) at the UW Chemistry Department for their generous inputs on my research. I would also like to thank Professor Bruce Robinson for having me be his TA. This work was facilitated through the use of advanced computational, storage, and networking infrastructure provided by the Hyak supercomputer system at the University of Washington.

# Chapter 1

# INTRODUCTION

## *1.1 Lateral phase separation and surface pattern formation in multicomponent lipid bilayer*

The lipid-bilayer membranes, as a fundamental structure and prototype of cell plasma membranes and artificial vesicles, e.g. those used for drug-delivery, are well-defined by their multiple lipid components. In a plasma membrane, the lipid bilayer is formed by an exoplasmic leaflet in direct contact with the aqueous environment outside the cell and a cytoplasmic leaflet facing the aqueous condition inside the cell. In each leaflet, the lipid molecules have their hydrophilic headgroups face water molecules outside the membrane and their hydrophobic tails point inward and are in contact with lipid tails from the opposite leaflet. In this way, the hydrophobic tails are covered by two hydrophilic layers on the surfaces, and the membrane becomes impermeable to water and is able to separate the internal structures of a cell from the surrounding environment. In general, biological membranes surrounding other structures such as organelles also play a similar role in separation. The fluid mosaic model described the lipid-bilayer membrane as a two-dimensional fluid in which lipid molecules flow laterally in the plane and proteins are embedded among them. The membrane proteins, as well as carbohydrates attached to them, play a critical role in fundamental biological functioning such as cell signaling.[1, 2, 3]

Treating the lipid-bilayer membrane as a 2D fluid surface, we focus on the lateral phases and surface patterns arising from separation of different lipid molecules. For a multicomponent lipid membrane to phase separate, it must at least consist of a high melting temperature species (usually higher than the room temperature), for example sphingomyelin or phospholipids with two saturated aliphatic tails such as DPPC (dipalmitoylphosphatidyl-

choline, di-16:0 PC, with 16 carbon atoms and 0 double bond in each tail) and DSPC (distearoylphosphatidylcholine, di-18:0 PC), and a low melting temperature species, for example phospholipids with two unsaturated tails such as DOPC (dioleoylphosphatidylcholine, di-18:1 PC) and DIPC (dilinoleoylphosphatidylcholine, di-18:2 PC). The lipids mix and form a homogeneous fluid phase at a temperature high enough as initially indicated by the fluid mosaic model. But when the temperature is lower than a phase transition temperature, the high-melting temperature lipids separate from the low-melting temperature ones and form a solid-ordered or gel phase, while the low-melting temperature lipids form a liquid-disordered phase. This coexistence of ordered and disordered phases could be sustained even if a third component, cholesterol, which contains a hydroxyl group and a small rigid planar hydrophobic body, is added into the system, when the solid or gel phase becomes a liquid-ordered phase which consists of high-melting temperature lipids along with cholesterols.[4, 5, 6, 7] This intriguing phase separation of a ternary lipid system has been observed most prominently by optical microscopy of membrane patches or giant unilamellar vesicles, and has also been found experimentally using techniques including infrared spectroscopy and fluorescence quenching[8, 9], nuclear magnetic resonance spectroscopy[10] and Förster resonance energy transfer[11, 12], etc. The small-angle neutron or X-ray scattering (SANS or SAXS) is also most helpful in probing small-scale vesicles or systems with a slight phase separation into multiple small domains.[13, 14, 15, 16, 17, 18] Such small domains of liquid-ordered phase are believed to be a possible origin of lipid rafts, which are functional domains where proteins are anchored on the surface of plasma membranes.[19, 20, 21] Both theoretical model studies[22, 23, 24, 25] and molecular simulations[26, 27, 28, 29, 30, 31] have confirmed these phase phenomena in ternary lipid-bilayer membranes.

When adding a fourth component into the system (an intermediate melting point lipid such as a hybrid lipid with a saturated tail and an unsaturated tail), one finds more diverse morphological patterns on the membrane surface. A heterogeneous state consisting of nanoscopic domains, and modulated phases composed of stripes or circular domains are suggested to happen in theory and are observed by some optical microscopy exper-

iments on either this kind of quaternary systems or some other compositionally tuned systems.[32, 33, 34, 35, 36, 37, 38, 39, 40, 41] When the domain sizes are below optical resolution, small-angle scattering such as SANS and SAXS is a more effective tool in detecting this heterogeneity.[42, 43, 44] Molecular dynamics simulations have also recently been used to probe the internal structure, component distribution and phase formation in a quaternary membrane[45, 46], and modulated phases are successfully reproduced by Monte Carlo simulations[47, 48, 49]. In addition, such abundant phase behaviors have also been recently captured by fluorescence microscopy on the surface of living cell membranes or giant plasma membrane vesicles[50, 51, 52, 53, 54], which consist of a much larger variety of lipid species, further suggesting the existence of these phases in plasma membrane *in vivo* and demanding theoretical methods to model the membrane surface in order to explain and predict these various surface patterns.

### *1.2 Theoretical models and tools, and their applications in the lipid membrane phase study*

Many theoretical models are applied to a binary surface composed of an ordered species and a disordered species, which respectively form liquid-ordered and liquid-disordered domains when phase separation happens or heterogeneity appears. These models can be manipulated in continuum or coarse-grained simulations to generate an equilibrium, most stable surface configuration.[55, 56, 57, 58] An elegant theoretical model from statistical mechanics, the Landau-Ginzburg model, can be set up in a phase-separating, continuous binary surface system where the free energy can be minimized and the corresponding equilibrium configuration can be found.[59, 60, 61, 62, 63] At high temperatures, the system is in a single homogeneous phase, and at low temperatures it is in coexistence of ordered and disordered phases. The model was originally used in magnetic systems[64] and other organic or inorganic systems[65] which present similar phase behaviors to those observed in lipid membranes. The physical meaning of the Landau-Ginzburg model as well as its parameters has been discussed in terms of Lennard-Jones model systems[66, 67]. Similar models have also been applied on pollen

grain surfaces which may undergo phase separation and form modulated phases in cell wall development.[68, 69]

By extending the standard Landau-Ginzburg model to allow for an effectively negative line tension (i.e. the energy cost of interface formation between liquid-ordered and liquid-disordered domains), modulated phases and a heterogeneous state regarded as a two-dimensional microemulsion are generated in addition to the homogeneous phase and two-phase coexistence state.[70, 71] The microemulsion state is a potential description and explanation of the heterogeneity that consist of nanoscopic domains which are short-lived and produced by thermal fluctuations, characterized by a certain intrinsic correlation length scale. In this way, some previous theoretical works have attributed a possible origin of lipid rafts to the emergence of the microemulsion state, in addition to many other possibilities.[72, 73, 74, 75, 76, 77] The application of the Landau-Ginzburg model to a flat lipid membrane surface is the subject of many previous theoretical studies. These works disregarded any finite size effect by assuming that the planar surfaces are infinitely large, while the effect of finite system size has long been found in other similar phase ordering systems[78, 79]. The lateral phase phenomenon on a spherical surface, whose size is limited by its finite radius, is a focal point of this dissertation.

Besides minimizing the extended Landau-Ginzburg free energy model and seeking an optimal surface configuration of the membrane system, calculating the static scattering structure factor of a two-dimensional material in planar or spherical topology, whose phase behavior can be similarly described by a simplified quadratic Landau-Ginzburg model, is performed. This type of material includes lipid membranes in the homogeneous or microemulsion state. The static structure factor is defined as the Fourier transform of the intermolecular pair correlation function.[80] The 2D structure factor of a flat membrane embedded in two dimensions is the scattering signal generated in a 2D wave vector space, which is usually modeled in simulations. On the other hand, it is the 3D structure factor of a membrane, usually a liposome or a vesicle, embedded in a three-dimensional wave vector space, that is mostly measured in a scattering experiment. Based on the calculation of these structure

factors, we are able to test the validity of a model-independent approximate relationship, which can transform a 2D structure factor into a 3D structure factor, and vice versa. We have derived this interconversion without referring to the specific expressions of structure factors, and thus this mathematical relationship is effective for the 2D and 3D structure factors of the same material with planar and spherical geometries respectively, regardless of the specific model describing it. The relationship turns out to be exact when the planar and spherical surfaces are both infinitely large, and is only approximate considering the finite sizes of the membrane patch and the spherical vesicle, illustrating the specific finite size effect in scattering studies. Dynamic structure factors[81, 82], however, are beyond the scope of this theoretical research.

A soft, deformable lipid membrane, especially a nonrigid vesicle, is of greater interest, more physically meaningful and biologically relevant than rigid spheres in the field of soft matter physics and biophysics. A classical expression of the energetics of membrane shape change is the Helfrich bending model, which considers the effects of both surface bending rigidity and spontaneous curvature.[83, 84, 85, 86, 87] Lipid distributions are sensitive to local curvatures.[88, 89, 90] It has been long observed that in a phase-separating membrane, ordered and disordered lipid domains would possess different bending curvatures. Specifically, liquid-ordered domains are flatter and liquid-disordered domains are more curved.[4, 91, 92] There have been multiple theoretical attempts to couple the surface bending curvature with the surface compositional organization, usually through an explicitly coupling term added on to a standard Landau-Ginzburg free energy plus a Helfrich bending energy, when writing the full free energy expression.[55, 75, 93, 94] There are also attempts which assume that the bending modulus and the spontaneous curvature are linearly dependent on surface compositional distribution.[47, 57, 58, 92] In this dissertation we use the latter method with implicit shape-composition couplings through bending properties. Using a quadratic approximation, we derive a full free energy expression that is composition-dependent and can be regarded as a Landau-Ginzburg model which may allow for an effectively negative interface line tension that is necessary to give rise to microemulsion and modulated phases on a rigid spherical

vesicle. We calculate ground state phase diagrams of deformable vesicles that are qualitatively comparable to similar phase diagrams obtained through the explicit coupling, and estimate values of several physical properties that can be compared with experimental and simulation values. The theoretical study of the dynamics of surface change is also of great significance in many previous studies[55, 63, 85, 92, 95, 96], but is beyond the scope of this ground state exploration.

The composition-curvature coupling through bending rigidity is partly induced by a bilayer thickness mismatch between domains, where ordered domains are typically thicker and disordered domains are thinner because ordered lipid tails are straighter and are more densely packed. The coupling through spontaneous curvature in plasma membranes or model vesicles is partly due to the asymmetric distribution of lipid species across the bilayer, resulting in a nonzero spontaneous curvature. For instance, it is known that in eukaryotic plasma membranes, the sphingomyelin and phosphatidylcholine (PC) are abundant in the outer leaflet, and phosphatidylethanolamine (PE) and phosphatidylserine (PS) are enriched in the inner leaflet.[75, 97] Various experimental evidence indicates that in a phase-separating lipid bilayer, either compositionally symmetric or asymmetric, ordered domains in a leaflet would align in registration with ordered domains in the opposite leaflet and disordered domains would also be in registration.[17, 54, 97, 98, 99, 100, 101] Some molecular dynamics simulations have confirmed this registration, while anti-registration may happen if there is a large contrast between ordered and disordered domain thicknesses or if the membrane size is too small.[102, 103] This coupling might be caused by interactions between lipid tails of similar degrees of saturation from opposing leaflets, and the flip-flop of cholesterols between liquid-ordered domains of the two leaflets. Furthermore, in a bilayer consisting of a naturally non-phase-separating leaflet and a phase-separating leaflet, the former may be observed to undergo an induced phase separation by the latter because of the inter-leaflet coupling.[104, 105] Inspired by this observation, we investigate the effect of asymmetric lipid-bilayer compositions on the phase behavior of opposing leaflets, performing molecular dynamics simulations to seek any sign of the induced phase separation. This work is a good

complement to the investigation of lipid vesicle phase behaviors.

### *1.3 Specific aims and methods*

This dissertation is divided into four parts, corresponding to the four aspects of research projects outlined in the previous section. The first project is on the phase diagrams of rigid spherical lipid-bilayer vesicles. The second is on the structure factor calculation of this kind of vesicles and the development of a relationship between structure factors with different dimensionalities. The third is the ground-state phase diagram study of deformable spherical vesicles. Lastly the fourth is the supplementary project on molecular dynamics simulation of asymmetric lipid bilayers.

*Phase diagrams of spherical lipid vesicles*

We implement the extended Landau-Ginzburg model on spherical surfaces of different sizes to investigate their phase behaviors, including the homogeneous phase, two-phase coexistence, modulated phases and a microemulsion, as well as phase transitions between them. By employing spherical harmonic analysis, we use analytical and numerical computation methods, and Monte Carlo simulations to calculate phase diagrams, in which phase transitions happen as Landau-Ginzburg parameters change. We make both ground state diagrams and diagrams at finite temperature, demonstrating how thermal fluctuation and intrinsic finite size effect from the sphere would influence the phase distributions and boundaries in the diagrams. We illustrate that the finite size effect is most evident and significant when the spherical radius is small, which has the most distinct phase diagram when compared with the planar surface case, which we use as a reference point. This work has led to a recent publication.[106]

*Model-free comparison of 2D and 3D structure factors*

By using the equipartition theorem and a simplified form of the extended Landau-Ginzburg model, which is a quadratic expression in essence and is called a Gaussian model, we calculate

the two-dimensional structure factor of a planar surface through Fourier transforms, and the three-dimensional structure factor of a spherical surface through spherical harmonic analysis followed by a Fourier transform, using the plane wave basis set expansion in spherical harmonics[107]. The transformation of a 2D signal into three dimensions is done by taking an orientational average, assuming the resulting 3D signal is from an infinitely large spherical surface. And the backward conversion from a 3D signal into two dimensions is an inverse Abel transform[108], which is not exact if the spherical surface is not large enough. Both conversions are proved to be independent of the Gaussian model. This work has led to another recent publication.[109]

*Composition-curvature coupling and phase diagrams of soft, deformable lipid vesicles*

We combine the standard Landau-Ginzburg model and the Helfrich bending model to describe the full energetics of a deformable vesicle surface. Mechanical properties including bending modulus and spontaneous curvature are rewritten into linear functionals of the surface compositional order parameter. By applying spherical harmonic analysis for both the compositional field and the shape deformation[85], followed by the application of quadratic approximations and constraints on surface area and total amounts of components, we simplify the full free energy into a composition-only expression. We then calculate ground state phase diagrams using either the single-mode approximation or full-mode calculation. We also calculate physical observables including the interface width and line tension. Both phase diagrams and resulting physical properties are qualitatively comparable to literature results.[47, 94]

*Molecular dynamics modeling of asymmetric lipid bilayers*

As inspired by Reference [104], we create molecular dynamics simulation models of three different ternary monolayers, two non-phase-separating and one phase-separating by itself, with the same lipid types but different compositions. We also prepare these leaflets in various sizes to detect possible small size effects. We observe final simulation configurations to seek

any indication of induced phase separation in the asymmetric bilayers, and calculate intra- and inter-leaflet pair correlation functions to identify domain formation and registration. For comparison, we build bilayer models formed by various leaflets consisting of predefined lipid compositions and distributions. Inter-leaflet correlations calculated from these models are compared with simulation results, and can help to explain the observed simulation configurations and reveal any phase change caused by the inter-leaflet coupling.

# Chapter 2

# LANDAU-GINZBURG MODEL AND THE MULTICOMPONENT LIPID VESICLE PHASE DIAGRAMS

In this chapter we start with the introduction of our specific theoretical tool, the Landau-Ginzburg free energy model, to deal with the lipid molecule distributions and organizations on the surface of a lipid membrane. Using the extended Landau-Ginzburg expression, we perform Fourier and spherical harmonic transforms for planar surface and spherical surface respectively. We focus on the latter, and present three different methods of generating phase diagrams of lipid vesicles: single-mode analytical calculation and full-mode numerical calculation for ground states which are thermal fluctuation free, and Monte Carlo simulation for equilibrium states at finite temperature. Besides the effect of thermal fluctuations, we emphasize the finite size effect of spherical surfaces, and compare the effect with similar effect of a finite-sized plane.

## *2.1 Introduction of the Landau-Ginzburg model and its applications on flat and spherical surfaces*

The definition of the Landau-Ginzburg free energy model depends on an order parameter on membrane surface. We introduce a continuous scalar order parameter field $\phi(\boldsymbol{r})$ on the two-dimensional surface $S$ instead of keeping track of each single molecule. The parameter is assigned to be positive at point $\boldsymbol{r}$ if it is in the liquid-ordered phase and negative if it is in the liquid-disordered phase. It turns out that the continuous (second-order) phase separation can be indicated by the transition of a globally uniform order parameter $\phi = 0$ into a coexistence of a domain of $\phi > 0$ and another domain of $\phi < 0$, when the energy is

defined as

$$E[\phi(\boldsymbol{r})] = \int \mathrm{d}S \left\{ \frac{\alpha}{2} |\phi(\boldsymbol{r})|^2 + \frac{b}{4} |\phi(\boldsymbol{r})|^4 + \frac{\gamma}{2} |\nabla\phi(\boldsymbol{r})|^2 \right\} \tag{2.1}$$

with phenomenological parameters $\alpha$, $b$ and $\gamma$ which are structural constants that reflect internal properties of the system. This is the standard Landau-Ginzburg free energy model, in which $\alpha$ and $b$ are temperature-related parameters, which also depend on the system's phase separation temperature as determined by its structure, and $\gamma$ is related to the interface line tension between domains on the surface when phase separation happens.

The order parameter $\phi$ is unitless, and the energy $E$ is scaled by $k_{\mathrm{B}}T$ and then units of all Landau-Ginzburg parameters ($\alpha$, $b$ and $\gamma$) are therefore determined by their positions in Equation (2.1). The parameters $b$ and $\gamma$ have to be positive so the free energy model does not diverge to negative infinity. When $\alpha$ is also positive, the system intuitively stays in a homogeneous phase marked by an order parameter which is globally $\phi = 0$ in the ground state. When $\alpha$ becomes negative (equivalent to raising the phase transition temperature), the system would either change the global order parameter into one of two degenerate values

$$\phi(\boldsymbol{r}) = \pm\sqrt{-\frac{\alpha}{b}} \tag{2.2}$$

when no constraints are applied on the surface composition, or change into a state of the coexistence of both $\phi = \pm\sqrt{-\alpha/b}$ if surface compositions of ordered and disordered species are conserved. This latter situation indicates a phase separation into liquid-ordered and liquid-disordered domains, and the positive $\gamma$ implies an energetic cost because of the positive line tension per unit interface length. In an ideal Landau-Ginzburg model on a flat, infinitely large surface, the line tension has been shown to be[62, 63]

$$\sigma = \sqrt{-\frac{8\gamma\alpha^3}{9b^2}} \tag{2.3}$$

and the interface width turns out to be

$$d = \sqrt{-\frac{2\gamma}{\alpha}}. \tag{2.4}$$

Both relations also apply to curved surfaces in an approximate way.

The extended Landau-Ginzburg model is defined as

$$E[\phi(\boldsymbol{r})] = \int \mathrm{d}S \left\{ \frac{\alpha}{2} |\phi(\boldsymbol{r})|^2 + \frac{b}{4} |\phi(\boldsymbol{r})|^4 + \frac{\gamma}{2} |\nabla\phi(\boldsymbol{r})|^2 + \frac{\epsilon}{2} \left|\nabla^2\phi(\boldsymbol{r})\right|^2 \right\} \tag{2.5}$$

where $b$ and $\epsilon$ are positive parameters. In this model, a negative $\gamma$ leads to an apparent line tension that appears negative. This can be realized by the effects of linactants (molecules binding to the interface) or by coupling composition to shape[77], which is the main subject of Chapter 4. The preference of more interfaces (domain walls, not interface between two separate phases) may lead to heterogeneous states such as microemulsion and modulated stripe phases in which each stripe domain is either liquid-ordered or liquid-disordered, illustrated by the sign of order parameter in the domain.

For the purpose of studying the lateral phase behavior of a two-dimensional surface depending on Landau-Ginzburg parameters $\alpha$ and $\gamma$, we minimize the energy to find the ground state or the equilibrium state at a finite temperature with thermal fluctuation at a certain parameter set ($\alpha$, $\gamma$). This analysis on a planar surface has already been done[70, 71] and the ground state analysis is briefly summarized here. We then present the free energy expression on a spherical surface.

### *2.1.1 Ground state phase boundaries of a planar surface*

On a square patch of edge length $L$, we use the Fourier transform to convert the order parameter $\phi(\boldsymbol{r})$ into Fourier modes $\tilde{\phi}(\boldsymbol{k})$,

$$\phi(\boldsymbol{r}) = \frac{1}{L^2} \sum_{\boldsymbol{k}} \tilde{\phi}(\boldsymbol{k}) e^{i\boldsymbol{k}\cdot\boldsymbol{r}}, \tag{2.6}$$

and the free energy functional is transformed into

$$E = \frac{1}{2L^2} \sum_{\boldsymbol{k}} (\alpha + \gamma k^2 + \epsilon k^4) |\tilde{\phi}(\boldsymbol{k})|^2 + \frac{b}{4L^6} \sum_{\boldsymbol{k},\boldsymbol{k}',\boldsymbol{k}''} \tilde{\phi}(\boldsymbol{k})\tilde{\phi}(\boldsymbol{k}')\tilde{\phi}(\boldsymbol{k}'')\tilde{\phi}(-\boldsymbol{k}-\boldsymbol{k}'-\boldsymbol{k}'') \tag{2.7}$$

in which Fourier wave vectors

$$\boldsymbol{k} = \left( \frac{2\pi i}{L}, \frac{2\pi j}{L} \right) \tag{2.8}$$

which is defined in a two-dimensional coordinate system where $i$ and $j$ are integers.

The homogeneous phase requires $\alpha > 0$ and $\gamma > 0$, for which we have the ground state order parameter and minimum energy ($E$ relabeled as $E_0$)

$$\phi = 0,\ E_0 = 0 \tag{2.9}$$

and in two-phase coexistence ($\alpha < 0$ but $\gamma > 0$), they become ($E$ relabeled as $E_2$)

$$\phi = \pm\sqrt{-\frac{\alpha}{b}},\ E_2 = -\frac{L^2\alpha^2}{4b}. \tag{2.10}$$

The modulated phase happens when $\gamma < 0$. Under the single-mode approximation, the phase is dominated by a single Fourier wave vector $\boldsymbol{k}^* \neq 0$ and the energy becomes

$$E = \frac{1}{L^2}(\alpha + \gamma(k^*)^2 + \epsilon(k^*)^4)|\tilde{\phi}(\boldsymbol{k}^*)|^2 + \frac{3b}{2L^6}|\tilde{\phi}(\boldsymbol{k}^*)|^4. \tag{2.11}$$

The wave vector magnitude and Fourier mode that minimize the energy expression are respectively

$$k^* = \sqrt{-\frac{\gamma}{2\epsilon}} \tag{2.12}$$

$$|\tilde{\phi}(\boldsymbol{k}^*)| = \sqrt{\frac{\gamma^2 - 4\alpha\epsilon}{12b\epsilon}}. \tag{2.13}$$

And the minimum energy is ($E$ relabeled as $E_1$)

$$E_1 = -\frac{L^2(\gamma^2 - 4\alpha\epsilon)^2}{96b\epsilon^2}. \tag{2.14}$$

By equating $E_0 = E_2$ we obtain the phase boundary (in a phase diagram) between the homogeneous phase and two-phase coexistence when $\gamma > 0$

$$\alpha = 0. \tag{2.15}$$

By equating $E_0 = E_1$ we obtain the phase boundary (in a phase diagram) between homogeneous and modulated phases when $\gamma < 0$

$$\alpha = \frac{\gamma^2}{4\epsilon}. \tag{2.16}$$

And we equate $E_1 = E_2$ for the boundary between modulated phase and two-phase coexistence when $\gamma < 0$:

$$\alpha = -\frac{\gamma^2}{2\epsilon}\left(1 + \sqrt{\frac{3}{2}}\right). \tag{2.17}$$

All boundaries are illustrated on the phase diagrams in Figure 2.1 used as references for spherical surface phase diagrams.

### *2.1.2 Landau-Ginzburg model on a spherical surface*

On the surface of a sphere of radius $R$, the extended Landau-Ginzburg free energy functional is rewritten as

$$\begin{aligned} E[\phi(\theta,\varphi)] &= \int \mathrm{d}S \left\{ \frac{\alpha}{2} |\phi(\theta,\varphi)|^2 + \frac{b}{4} |\phi(\theta,\varphi)|^4 + \frac{\gamma}{2} |\nabla\phi(\theta,\varphi)|^2 + \frac{\epsilon}{2} \left|\nabla^2\phi(\theta,\varphi)\right|^2 \right\} \\ &= R^2 \int \mathrm{d}\Omega \left\{ \frac{\alpha}{2} |\phi(\theta,\varphi)|^2 + \frac{b}{4} |\phi(\theta,\varphi)|^4 + \frac{\gamma}{2} |\nabla\phi(\theta,\varphi)|^2 + \frac{\epsilon}{2} \left|\nabla^2\phi(\theta,\varphi)\right|^2 \right\}. \end{aligned} \tag{2.18}$$

The integral is over solid angle $\Omega$, and the scalar order parameter field is now defined as a function of polar angle $\theta$ and azimuthal angle $\varphi$, $\phi(\Omega) = \phi(\theta,\varphi)$. The spherical surface area is $S = 4\pi R^2$ and $\mathrm{d}S = R^2\mathrm{d}\Omega$, and $\nabla$ and $\nabla^2$ are angular parts of the gradient and Laplace operators where

$$\nabla^2 = \frac{1}{R^2\sin^2\theta}\frac{\partial^2}{\partial\varphi^2} + \frac{1}{R^2\sin\theta}\frac{\partial}{\partial\theta}\left(\sin\theta\frac{\partial}{\partial\theta}\right). \tag{2.19}$$

To achieve the goal of studying lateral phase behavior, the spherical harmonic transform is first performed and the order parameter is expanded in terms of spherical harmonic functions

$$\phi(\theta,\varphi) = \sum_{l=0}^{\infty}\sum_{m=-l}^{l} w_{l,m}Y_{l,m}(\theta,\varphi) \equiv \sum_{l,m} w_{l,m}Y_{l,m}(\theta,\varphi) \tag{2.20}$$

where $w_{l,m}$ is the amplitude of the spherical harmonic mode of integer degrees $l$ and $m$

$$w_{l,m} = \int \mathrm{d}\Omega\, Y^*_{l,m}(\theta,\varphi)\phi(\theta,\varphi) \tag{2.21}$$

which has the property

$$w^*_{l,m} = (-1)^m w_{l,-m} \tag{2.22}$$

for $\phi$ is always real.

From the National Institute of Standards and Technology Digital Library of Mathematical Functions[110] we find the following equations

$$\int \mathrm{d}\Omega\, Y^*_{l,m}(\theta,\varphi) Y_{l',m'}(\theta,\varphi) = \delta_{l,l'}\delta_{m,m'} \tag{2.23}$$

$$\nabla^2 Y_{l,m}(\theta,\varphi) = -\frac{l(l+1)}{R^2} Y_{l,m}(\theta,\varphi) \tag{2.24}$$

which can be used to transform the quadratic terms in the integral of Equation (2.18)

$$\int \mathrm{d}\Omega\ |\phi|^2 = \int \mathrm{d}\Omega\, \phi^*\phi = \sum_{l,m} |w_{l,m}|^2 \tag{2.25}$$

$$\int \mathrm{d}\Omega\, |\nabla\phi|^2 = -\int \mathrm{d}\Omega\, \phi^*\nabla^2\phi = \sum_{l,m} \frac{l(l+1)}{R^2} |w_{l,m}|^2 \tag{2.26}$$

$$\int \mathrm{d}\Omega\ \left|\nabla^2\phi\right|^2 = \int \mathrm{d}\Omega\, (\nabla^2\phi)^*\nabla^2\phi = \sum_{l,m} \frac{[l(l+1)]^2}{R^4} |w_{l,m}|^2. \tag{2.27}$$

The transform of the quartic term requires the expansion of $\phi^2$ in terms of spherical harmonic functions with spherical harmonic modes $u_{l,m}$ following Equations (2.20) and (2.21):

$$|\phi(\theta,\varphi)|^2 = \sum_{l,m} u_{l,m} Y_{l,m}(\theta,\varphi) \tag{2.28}$$

$$u_{l,m} = \int \mathrm{d}\Omega\, Y^*_{l,m}(\theta,\varphi)\, |\phi(\theta,\varphi)|^2 = \sum_{l_1,m_2}\sum_{l_2,m_2} w_{l_1,m_1} w_{l_2,m_2} \int \mathrm{d}\Omega\, Y^*_{l,m}(\theta,\varphi) Y_{l_1,m_1}(\theta,\varphi) Y_{l_2,m_2}(\theta,\varphi). \tag{2.29}$$

Then we can substitute into Equation (2.29) the following integral of the multiplication of three spherical harmonic functions[110],

$$\int \mathrm{d}\Omega\, Y_{l_1,m_1}(\theta,\varphi) Y_{l_2,m_2}(\theta,\varphi) Y_{l,m}(\theta,\varphi) = \sqrt{\frac{(2l_1+1)(2l_2+1)(2l+1)}{4\pi}} \begin{pmatrix} l_1 & l_2 & l \\ 0 & 0 & 0 \end{pmatrix} \begin{pmatrix} l_1 & l_2 & l \\ m_1 & m_2 & m \end{pmatrix}, \tag{2.30}$$

and follow Equation (2.25) to obtain

$$\int \mathrm{d}\Omega\ |\phi|^4 = \int \mathrm{d}\Omega\,(|\phi|^2)^2 = \sum_{l,m}|u_{l,m}|^2$$
$$= \sum_{l,m}\left|\sum_{l_1,m_1}\sum_{l_2,m_2}\sqrt{\frac{(2l_1+1)(2l_2+1)(2l+1)}{4\pi}}\begin{pmatrix} l_1 & l_2 & l \\ 0 & 0 & 0\end{pmatrix}\begin{pmatrix} l_1 & l_2 & l \\ m_1 & m_2 & m\end{pmatrix} w_{l_1,m_1}w_{l_2,m_2}\right|^2 . \tag{2.31}$$

Together with the quadratic results, it transforms Equation (2.18) into

$$E = \frac{R^2}{2}\sum_{l,m}\left\{\alpha + \frac{\gamma}{R^2}l(l+1) + \frac{\epsilon}{R^4}[l(l+1)]^2\right\}|w_{l,m}|^2$$
$$+ \frac{bR^2}{4}\sum_{l,m}\left|\sum_{l_1,m_1}\sum_{l_2,m_2}\sqrt{\frac{(2l_1+1)(2l_2+1)(2l+1)}{4\pi}}\begin{pmatrix} l_1 & l_2 & l \\ 0 & 0 & 0\end{pmatrix}\begin{pmatrix} l_1 & l_2 & l \\ m_1 & m_2 & m\end{pmatrix} w_{l_1,m_1}w_{l_2,m_2}\right|^2 \tag{2.32}$$

which includes Wigner 3j symbols.

## *2.2 Computation and simulation methods for spherical surface phase diagrams*

We further analyze the Landau-Ginzburg model in spherical harmonic space to find the spherical harmonic mode set $\{w_{l,m}\}$ that minimizes (at ground state) or equilibrates (at finite temperature) the energy, which is equivalent to $\phi$ in real space. Ground state calculations are operated and treated analytically or numerically. We assume the ground state has a rotational symmetry in the absence of thermal fluctuations, and a modulated phase consists of parallelly aligned stripes circling around the same direction, so the order parameter for any phase or state becomes independent of the azimuthal angle $\varphi$ and so the spherical harmonic modes are independent of $m$, which indicates that only $w_{l,0}$ terms are nonzero (must be real) for $\phi(\theta)$ in Equation (2.20). For each modulated stripe phase there exists a dominant spherical harmonic degree $l$, whose physical meaning is the number of interfaces, or equivalently $l+1$ is the number of domains on the spherical surface. Under this

simplification, the single- and full-mode approximations treat the homogeneous phase (and two-phase coexistence) in identical way, and both cannot search for microemulsion because of the lack of thermal fluctuation, but they deal with a modulated phase in different ways. The single-mode approximation allows only one spherical harmonic mode $w_{l,0}$ to be nonzero for each modulated phase of dominant spherical harmonic degree $l$, while the full-mode approximation allows $w_{l,0}$ from $l = 0$ to a predefined $l_{\max}$ to vary, but the most pronounced $|w_{l,0}|$ resulting from the Landau-Ginzburg free energy minimization determines the dominant $l$. We also show how Monte Carlo simulations are used to sample the equilibrium state with thermal fluctuations, and how the lateral phase or state dependent on both $\theta$ and $\varphi$ can be identified by indicators like the visual surface pattern and the thermal equilibrium means $\langle w_{l,m} \rangle$ and variances $\langle |\delta w_{l,m}|^2 \rangle$ of spherical harmonic modes. These indicators are used to find the dominant $l$ for modulated phases and are illustrated in several examples.

We use multiple Landau-Ginzburg free energy forms of Equation (2.32) in the analysis of the ground state at single-mode and full-mode approximations and thermal equilibrium state separately. In each case, Landau-Ginzburg parameters $\epsilon$ and $b$ are both set to be constant 1, and the resulting phase or state at each parameter set ($\alpha$, $\gamma$) is pinpointed on a phase diagram of $\alpha$ vs. $\gamma$ in which $-3.0 \leqslant \alpha \leqslant 3.0$ and $-3.0 \leqslant \gamma \leqslant 1.0$ and intervals between neighboring sampling points are $\Delta\alpha = 0.1$ and $\Delta\gamma = 0.1$. We do the same ground state calculations and Monte Carlo simulations for each of the three radii $R = 1$, 3 and 10 over the same parameter ranges of phase diagram.

### *2.2.1 Single-mode analytical calculation at ground state*

Based on the reasoning for ground state, we have in single-mode approximation

$$\phi(\theta) = w_{l,0} Y_{l,0}(\theta) \tag{2.33}$$

$$E = \frac{R^2}{2}\left\{\alpha + \frac{\gamma}{R^2} l(l+1) + \frac{\epsilon}{R^4}[l(l+1)]^2\right\} w_{l,0}^2 + \frac{bR^2}{4} \sum_{l'=0}^{2l} \frac{(2l+1)^2(2l'+1)}{4\pi} \left| \begin{pmatrix} l & l & l' \\ 0 & 0 & 0 \end{pmatrix} \right|^4 w_{l,0}^4. \tag{2.34}$$

If $l = 0$, the single-mode state is a homogeneous phase or two-phase coexistence, and their free energies are respectively $E = 0$ for $\phi = 0$ and

$$E = -\frac{\pi\alpha^2 R^2}{b} \tag{2.35}$$

for $\phi = \pm\sqrt{-\alpha/b}$. For each modulated phase of dominant $l > 0$, the Landau-Ginzburg free energy expression is the full Equation (2.34) which can be minimized with respect to the only $w_{l,0}$. At each point ($\alpha$, $\gamma$) on the phase diagram, Equation (2.34) is minimized and calculated for each modulated phase by having $l = 1$ to $l_{\max} = 21$ in an analytical way. Comparing them with $E = 0$ (homogeneous, when $\alpha > 0$) and $E = -\pi\alpha^2 R^2/b$ (two-phase coexistence, when $\alpha < 0$), we find the state giving the minimum energy as the ground state at this point and mark it on the phase diagram. Resulting single-mode diagrams for different radii are shown in Figure 2.1 (a), with phase regions separated by three major phase boundaries and boundaries between modulated phases of different dominant $l$.

### *2.2.2 Full-mode numerical calculation at ground state*

The order parameter and Landau-Ginzburg free energy expression in full-mode approximation are

$$\phi(\theta) = \sum_{l=0}^{l_{\max}} w_{l,0} Y_{l,0}(\theta) \tag{2.36}$$

$$\begin{aligned} E =& \frac{R^2}{2}\sum_{l=0}^{l_{\max}} \left\{\alpha + \frac{\gamma}{R^2} l(l+1) + \frac{\epsilon}{R^4}[l(l+1)]^2\right\} w_{l,0}^2 \\ &+ \frac{bR^2}{4}\sum_{l=0}^{2l_{\max}} \left[\sum_{l_1=0}^{l_{\max}}\sum_{l_2=0}^{l_{\max}} \sqrt{\frac{(2l_1+1)(2l_2+1)(2l+1)}{4\pi}} \begin{vmatrix} l_1 & l_2 & l \\ 0 & 0 & 0 \end{vmatrix}^2 w_{l_1,0} w_{l_2,0}\right]^2 \end{aligned} \tag{2.37}$$

where we choose a predefined upper limit $l_{\max} = 21$. For each phase diagram point ($\alpha$, $\gamma$), we search for the spherical harmonic set $\{w_{l,0}\}$ of $l_{\max} + 1$ spherical harmonic modes that minimize Equation (2.37). Starting from an initial set (e.g. all $w_{l,0} = 0$), the target $\{w_{l,0}\}$ is found through numerical optimization techniques including the Broyden-Fletcher-Goldfarb-Shanno (BFGS) algorithm and Sequential Least Squares Programming (SLSQP) (whichever

gives a lower minimum energy is applied), with the help of the SHTOOLS Python spherical harmonics library[111]. If $w_{l,0} = 0$ holds for all $l$, the system is in a homogeneous phase. If $l = 0$ gives rise to the largest $|w_{l,0}|$ (here $|w_{0,0}|$), the system is in two-phase coexistence. Otherwise if the largest $|w_{l,0}|$ is at $l > 0$, the system is in a modulated stripe phase dominated by the mode $l$. The full-mode results are in presented Figure 2.1 (b), which has a better correspondence with the flat patch phase diagram at large radius.

### *2.2.3 Monte Carlo simulation at finite temperature*

The procedure of finding the thermal equilibrium energy and the surface configuration of a spherical harmonic set $\{w_{l,m}\}$ in equilibrium using Monte Carlo simulation is more straightforward, which involves the full spherical harmonic expansion (Equation (2.20)) and Landau-Ginzburg free energy expression (Equation (2.32)). The real and imaginary parts of each $w_{l,m}$, $c_{l,m}$ and $s_{l,m}$ respectively, are sampled separately over $l = 0$ to $l_{\max} = 21$ and $m = 0$ to $l$ for each $l$. Here $w_{l,0}$ is already real and because of Equation (2.22), the real and imaginary parts only vary independently when $m > 0$. Again with the help of SHTOOLS Python library[111], we can substitute the real and imaginary parts into Equation (2.32) with the same upper limit $l_{\max}$, and sample the configuration in a Metropolis algorithm at each ($\alpha$, $\gamma$) starting from all spherical harmonic modes $w_{l,m} = 0$. The Monte Carlo sampling temperature is $T = 0.1$, whose function is only to introduce some thermal fluctuations, and the step size added onto sampled modes is defined to be

$$0.1 \times \sqrt{\frac{T}{\alpha R^2 + \gamma + \epsilon/R^2}} \times X \tag{2.38}$$

where $X \sim N(0, 1)$ is a random number drawn from the standard normal distribution, if $\alpha R^2 + \gamma + \epsilon/R^2 > 0$, or the step size is simply $0.1 \times X$ if $\alpha R^2 + \gamma + \epsilon/R^2 \leqslant 0$, while the total step number in one simulation is

$$10^6 \times (l_{\max} + 1)^2. \tag{2.39}$$

The resulting spherical harmonic configuration is transformed back to real space $\phi(\theta, \varphi)$ to plot the visual pattern on a spherical surface, which could be almost homogeneous globally (uniform, microemulsion or two-phase coexistence, which has a different global $\phi \neq 0$) or with clear stripes (modulated phase). Along the process of Monte Carlo simulation, we calculate the ensemble thermal equilibrium averages $\langle w_{l,m} \rangle$ and variances $\langle |\delta w_{l,m}|^2 \rangle$ (actually $\langle c_{l,m} \rangle$, $\langle s_{l,m} \rangle$, and $\langle (\delta c_{l,m})^2 \rangle = \langle c_{l,m}^2 \rangle - \langle c_{l,m} \rangle^2$ and $\langle (\delta s_{l,m})^2 \rangle = \langle s_{l,m}^2 \rangle - \langle s_{l,m} \rangle^2$), the latter of which distinguishes a microemulsion from the homogeneous phase. The two-phase coexistence has the most distinct $\langle w_{l,m} \rangle$ with $\langle w_{0,0} \rangle$ apparently different from 0, representing an overall shift in $\phi$. The phase diagrams with thermal fluctuation are shown in Figure 2.1 (c) with microemulsion regions included, and phase indicators of seven sampling points on the diagram for $R = 10$ are extracted and shown in Figures 2.2 and 2.3.

## *2.3 Results*

### *2.3.1 Single-mode ground state phase diagrams*

Figure 2.1 (a) summarizes ground state phase diagrams obtained by the single-mode approximation. All diagrams share the same ranges and discretizations of Landau-Ginzburg parameters ($\alpha$, $\gamma$). The three columns are results from spherical surfaces of radii $R = 1$, 3 and 10, respectively. The ground state calculation is able to capture phase regions of homogeneous phase, two-phase coexistence (both marked by text labels) and modulated phases marked by their characteristic dominant spherical harmonic degree $l^*$. Phase boundaries are separations between regions of different colors. Also plotted are mean-field phase boundaries separating the major states on planar surface, which is provided by reference[70] and was derived previously. Among them the solid horizontal line $\alpha = 0$ at $\gamma > 0$ separates the homogeneous and "two-phase coexistence" regions, while the solid parabola separates homogeneous and modulated phases and the dashed line separates "two-phase coexistence" and modulated regions. A solid boundary represents a continuous (second-order) phase transition and the dashed curve is a first-order transition. They are presented for illustrating how

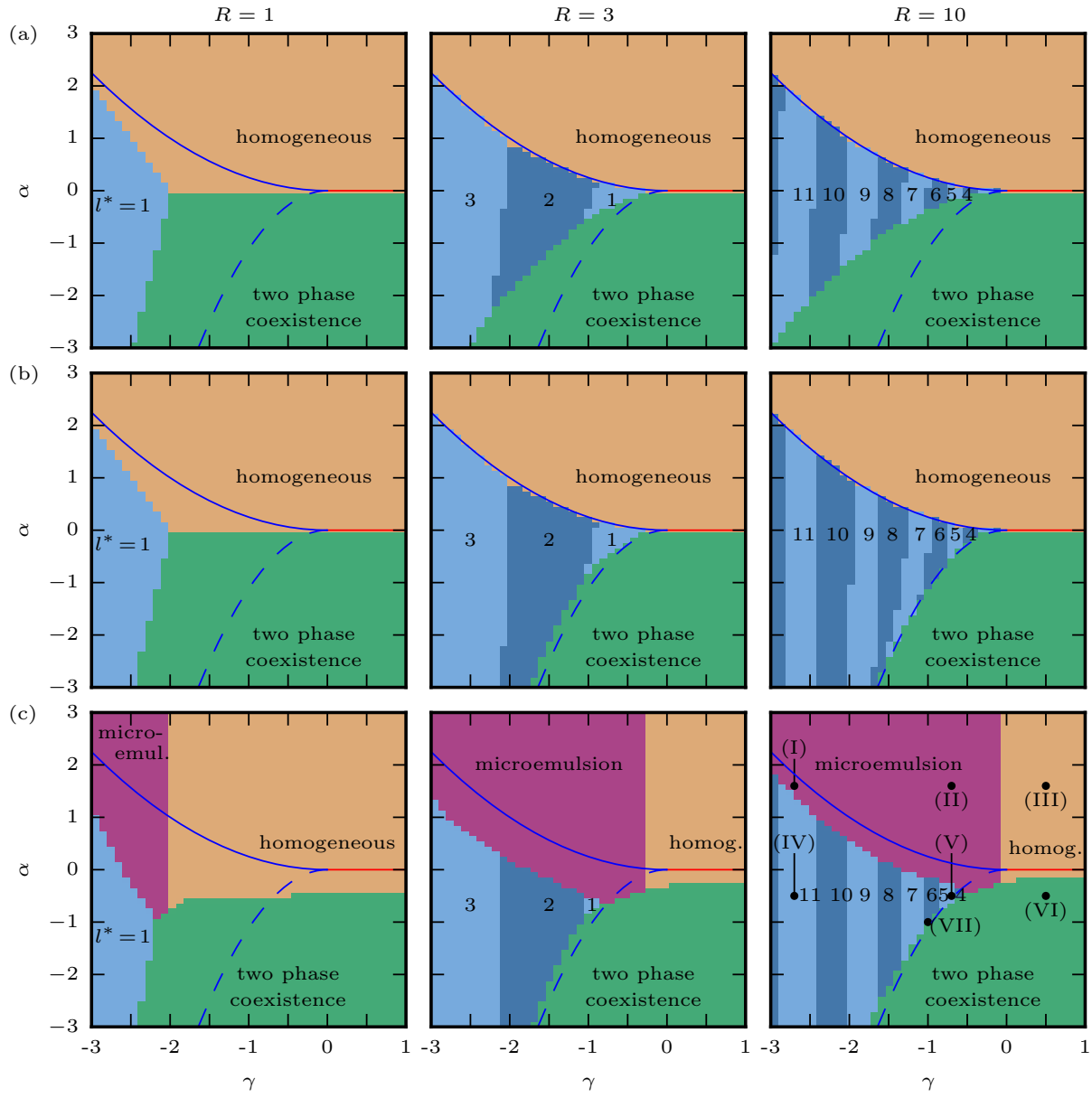


Figure 2.1: Lateral phase diagrams of spherical surfaces of radii $R = 1$, 3 and 10 (the first to third columns) generated by (a) analytical single-mode ground state calculation (b) numerical full-mode ground state calculation and (c) Monte Carlo simulation at finite temperature, as plotted in terms of Landau-Ginzburg parameters $\alpha$ vs. $\gamma$. Each modulated phase is labeled by its dominant spherical harmonic degree $l^*$. Also plotted are ground state phase region boundaries predicted for a planar surface for comparison (solid horizontal line at $\gamma > 0$: $\alpha = 0$; solid parabola at $\gamma < 0$: $\alpha = \gamma^2/(4\epsilon)$; dashed curve: $\alpha = -\gamma^2/(2\epsilon) \times (1 + \sqrt{3/2})$). Points (I)–(VII) from $R = 10$ diagram in (c) are extracted for phase indicators as shown in detail in Figures. 2.2 and 2.3 (I: $\alpha = 1.6$, $\gamma = -2.7$; II: $\alpha = 1.6$, $\gamma = -0.7$; I: $\alpha = 1.6$, $\gamma = 0.5$; IV: $\alpha = -0.5$, $\gamma = -2.7$; V: $\alpha = -0.5$, $\gamma = -0.7$; VI: $\alpha = -0.5$, $\gamma = 0.5$; VII: $\alpha = -1.0$, $\gamma = -1.0$).

the spherical geometry affects the distribution of phase regions and change phase boundaries from planar geometry especially at a small size.

The $R = 1$ phase diagram has the most obvious deviation from flat case, which in the Landau-Ginzburg parameter ranges only shows the $l^* = 1$ dominated modulated phase where one interface separates two domains, and the triple point is roughly at $\alpha = 0.0$ and $\gamma = -2.0$. The $l^* = 1$ phase is essentially different from two-phase coexistence as reflected by its lower energy in its region. At a certain point ($\alpha$, $\gamma$) the domain size (stripe width) in modulated phase is determined by Landau-Ginzburg parameters and is independent of spherical size. This is approximately half the correlation wavelength in planar geometry and is thus

$$\lambda^* = \frac{\pi}{k^*} \tag{2.40}$$

where $k^* = \sqrt{-\gamma/(2\epsilon)}$ (Equation (2.12)) is the characteristic Fourier wave vector of an infinitely large flat patch[70]. The number of interfaces is then an integer approximately equal to

$$l^* = \frac{\pi R}{\lambda^*} - 1 = Rk^* - 1 = R\sqrt{-\frac{\gamma}{2\epsilon}} - 1. \tag{2.41}$$

So intuitively at fixed ($\alpha$, $\gamma$) we expect fewer stripes and interfaces on a smaller sphere, but more stripes on a larger sphere which is able to show larger $l^*$, which corresponds to the trend observed on phase diagrams from $R = 1$, 3 to 10. The phase boundaries are straight, and we have calculated their equations, which are confirmed to be linear, by processing a similar ground state analysis to that of a planar surface. As the radius increases, there emerge more modulated phases, each of which is separated by straight boundaries from homogeneous and coexistence regions, and also from other modulated regions dominated by other $l^*$. The largest dominant $l^*$ observed is 12, indicating that truncating the spherical harmonic expansion at $l_{\max} = 21$ does not result in significant deviations. The whole piecewise linear boundary between homogeneous and modulated regions approaches and eventually almost overlaps the planar counterpart boundary, and the triple point also shifts to $\gamma = 0.0$ as in the flat case. This is because the spherical surface becomes more planar as $R$ increases and is effectively flat when its size is large at $R = 10$. The other piecewise linear boundary

between "two-phase coexistence" and modulated regions, however, constantly resists to approach the planar first-order transition boundary. This could be explained by the existence of metastable states around the first-order boundary. The single-mode method could have erroneously selected a metastable two-phase coexistence to be the global minimum state instead of actual modulated phases, leading to the reduction of modulated regions and expansion of the coexistence region. Above all, the diagrams all demonstrate that a positive $\alpha$ leads to a uniform state and a negative $\alpha$ leads to phase separation, and from a negative $\gamma$ emerges heterogeneous modulated phase giving rise to a variety of surface patterns.

### *2.3.2 Full-mode ground state phase diagrams*

Ground state phase diagrams from full-mode calculation as illustrated in Figure 2.1 (b) present similar phase region distributions and a trend of change on diagrams with increasing spherical size. The facts of homogeneous and "two-phase coexistence" regions diminishing and more abundant modulated phases emerging with increasing $R$ both reflect the ability of larger spherical surfaces to accommodate more domains and interfaces. Meanwhile, the increasing extent of major phase boundaries and triple point overlapping the planar boundaries and triple point, respectively, demonstrates the increase of surface flatness. Both single-mode and full-mode ground state calculations actually generate identical phase diagrams for $R = 1$, because the $l^* = 1$ modulated phase only involves one spherical harmonic mode in both single-mode and full-mode descriptions. The first-order transition boundary separating two-phase coexistence and modulated phases is shown to also approach and overlap the dashed curve from the planar case, indicating the better effectiveness of full-mode calculations in avoiding metastable states and finding the global minimum near a first-order phase transition compared to the single-mode approximation. We can then use full-mode diagrams as more accurate ground state phase diagrams to contrast with the thermally fluctuated case at finite temperature.

### *2.3.3 Finite temperature phase diagrams with thermal fluctuations*

Clear effects of thermal fluctuation in Monte Carlo simulations are illustrated in the finite temperature phase diagrams in Figure 2.1 (c). The microemulsion region emerges from inside the homogeneous region, separated from the homogeneous phase by a vertical Lifshitz line[75, 70] which is located at around $\gamma = -2.0$ for $R = 1$ and $\gamma = 0.0$ for $R = 3$ and 10. Thus an accompanying triple point split also occurs, with the two resulting triple points shifting toward the planar ground state triple point at the origin but never overlapping. The whole continuous transition boundaries surrounding homogeneous and microemulsion phase regions are lowered down because thermal fluctuations disturb phase separation and favor a mixed state, thus effectively lowering down the characteristic phase transition temperature of the system, and so the boundaries never overlap ground state boundaries.

The effects of thermal fluctuations, including the disruption of axisymmetric ground states so that the surface patterns depend on both $\theta$ and $\varphi$, can be visually demonstrated by the simulated irregular spherical surface patterns $\phi(\theta, \varphi)$ as well as plots of thermal equilibrium averages and variances of their spherical harmonic modes, $\langle w_{l,m} \rangle$ and $\langle |\delta w_{l,m}|^2 \rangle$ (actually those of real and imaginary parts $c_{l,m}$ and $s_{l,m}$), in Figure 2.2, which are for points (I)–(VI) extracted from the $R = 10$ phase diagram in Figure 2.1 (c). The phases and states giving rise to these patterns include microemulsions (I and II), homogeneous phase (III), modulated phases (VI and V) and one of two coexisting phases (VI), which is generated due to the condition that the order parameter scalar field $\phi(\theta, \varphi)$ is not constrained and thus is easily distinguished from the $l = 1$ modulated phase. Here the coexisting phase has the global scalar field $\phi$ shift to a positive value at random, which at the beginning of the Monte Carlo simulation is equally likely to shift to a negative value into the other coexisting phase. In states other than two-phase coexistence, the global average of $\phi$ is all around 0 without an overall shift. The modulated phases are also easily identifiable with stripe domains, each of a positive or a negative $\phi$. The domains are clearly irregular and are not in a parallel alignment as in the ground state. The surface patterns of homogeneous phase and microemulsions are

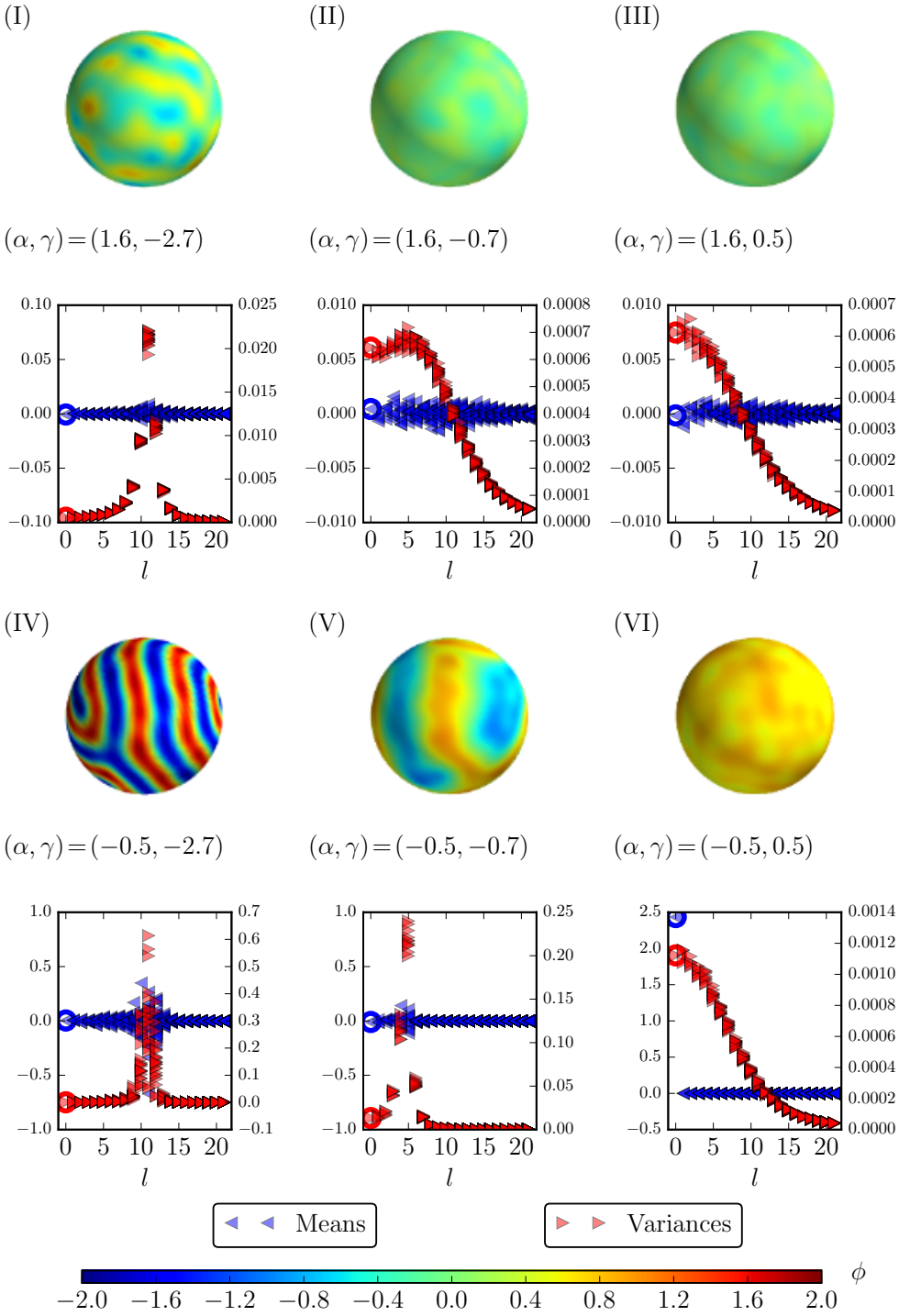


Figure 2.2: Phase indicators generated by Monte Carlo simulation at points (I)–(VI) in Figure 2.1 (c) for $R = 10$. Below each spherical surface pattern is a combined plot of thermal equilibrium means and variances of order parameter spherical harmonic modes. Scales of means are given on the left side and scales of variances are on the right. Phases include microemulsions (I and II), homogeneous phase (III), modulated phases (IV and V) and two-phase coexistence (one of two coexisting phases, VI). Circled are means and variances at $l = 0$. The color bar scales the magnitude of order parameter on the surface.

indistinguishable unless the microemulsion is near the phase transition boundary between microemulsion and modulated phases and has obvious phase fluctuations.

In order to further differentiate among the phases, we utilize spherical harmonic means and variances as phase indicators. Plotted below surface patterns are the means and variances of real and imaginary parts of spherical harmonic modes as a function of spherical harmonic degree $l$ at each of the points, with leftward pointing blue triangles for means and rightward pointing red triangles for variances. Means are valued at around 0 for most of the states, but are pronounced at around dominant $l^*$ of a modulated phase, and most pronounced at $l^* = 0$ for the coexisting phase (VI). Here $\langle w_{0,0} \rangle$ (circled in blue) shifts to a positive number, which is about 2.5, equivalent to the overall shift of $\phi$ to a positive value (about 0.7) as observed from its surface pattern. This can be confirmed by noticing that at this point $\alpha = -0.5$ and $b$ is always 1, so that the spherical harmonic mode is $l^* = 0$ and the order parameter is

$$w_{0,0} = \pm\sqrt{-\frac{\alpha}{b}} \approx \pm 0.7 \tag{2.42}$$

$$\phi = \pm\sqrt{-\frac{4\pi\alpha}{b}} \approx \pm 2.5. \tag{2.43}$$

The more helpful indicator is the distribution of variances, which illustrates a monotonically decreasing trend with increasing $l$ (when $\langle |\delta w_{0,0}|^2 \rangle$ circled in red is where the maximum is located) for a single homogeneous phase (III) or one of the coexisting phases (VI), for they are both uniform. There are single peaks at some nonzero $l^*$ for other phases (when $\langle |\delta w_{0,0}|^2 \rangle$ circled in red is obviously not maximum), which are identified as dominant $l^* = 11$ of (I) and (IV), and $l^* = 5$ of (II) and (V). The dominant $l^*$ of a microemulsion determines the length scale of compositional order parameter fluctuations. Within the Landau-Ginzburg parameter ranges of these phase diagrams, two points (e.g. a modulated phase and a microemulsion) sharing the same $\gamma$ could also share the same dominant $l^*$, suggesting they have the same characteristic correlation length scale of domains or fluctuations. This is also why boundaries between modulated phases in Figure 2.1 (c) all look vertical.

Surface patterns and other indicators of point (VII) in Figure 2.1 (c), which is exactly at the boundary between modulated phases and two-phase coexistence on the same diagram,

are included in Figure 2.3, which contains two possible states: (a) one of two coexisting phases (here $\phi$ shifts to a negative value globally) and (c) a modulated phase of dominant $l^* = 6$. When the first-order transition happens at this point, the coexistence state and the modulated phase change discontinuously into each other. The coexisting phase in (a) showing a global negative order parameter is also confirmed by its negative $\langle w_{0,0} \rangle$ (circled in blue in the plot of means). However, its distribution of variances does not monotonically decrease with $l$ but rather gives a peak at a nonzero $l^*$ ($\langle |\delta w_{0,0}|^2 \rangle$ circled in red is not maximum), indicating that it is in fact a microemulsion of the same dominant $l^* = 6$. This suggests that on the phase diagram with thermal fluctuations, the Lifshitz line between homogeneous and microemulsion regions can be extended into the two-phase coexistence region, separating a subregion from it at small $\gamma$ ($\gamma < -2.0$ for $R = 1$, $\gamma < -0.2$ for $R = 3$ and $\gamma < 0.0$ for $R = 10$) where each of the coexisting phases is a microemulsion. A similar extension of the Lifshitz line was also addressed on the phase diagram of planar geometry[70]. The equally possible modulated phase in (c), on the other hand, is well identified by its phase indicators.

Figure 2.3 (b) plots the Landau-Ginzburg free energy changes in a hysteresis loop as $\gamma$ increases or decreases across point (VII), displaying free energies of states in (a) and (c) and both global minimum states and metastable states around it. We first keep $\alpha = -1.0$ and decrease $\gamma$ from $-0.6$ to $-1.6$, in which process the initial state is two-phase coexistence at a starting energy around $E = -280$. In the direction of leftward pointing triangles, the system crosses the boundary marked by (a) and stays in two-phase coexistence which is metastable and has a similar energy as the initial energy, until $\gamma$ reaches $-1.5$ when the systems goes through a first-order transition into a metastable modulated phase with a more negative energy. When $\gamma$ reaches -1.6, the system transitions to the global minimum modulated phase, as its energy coincides with the trend in the other direction. We then increase $\gamma$ from $-1.7$ to $-0.7$, in which the initial state is a modulated phase with a much lower energy around $E = -570$. In the direction of rightward pointing triangles, the system experiences continuous transitions between global minimum modulated phases as the energy increases continuously. It still increases even after crossing the boundary marked by (c), and has a

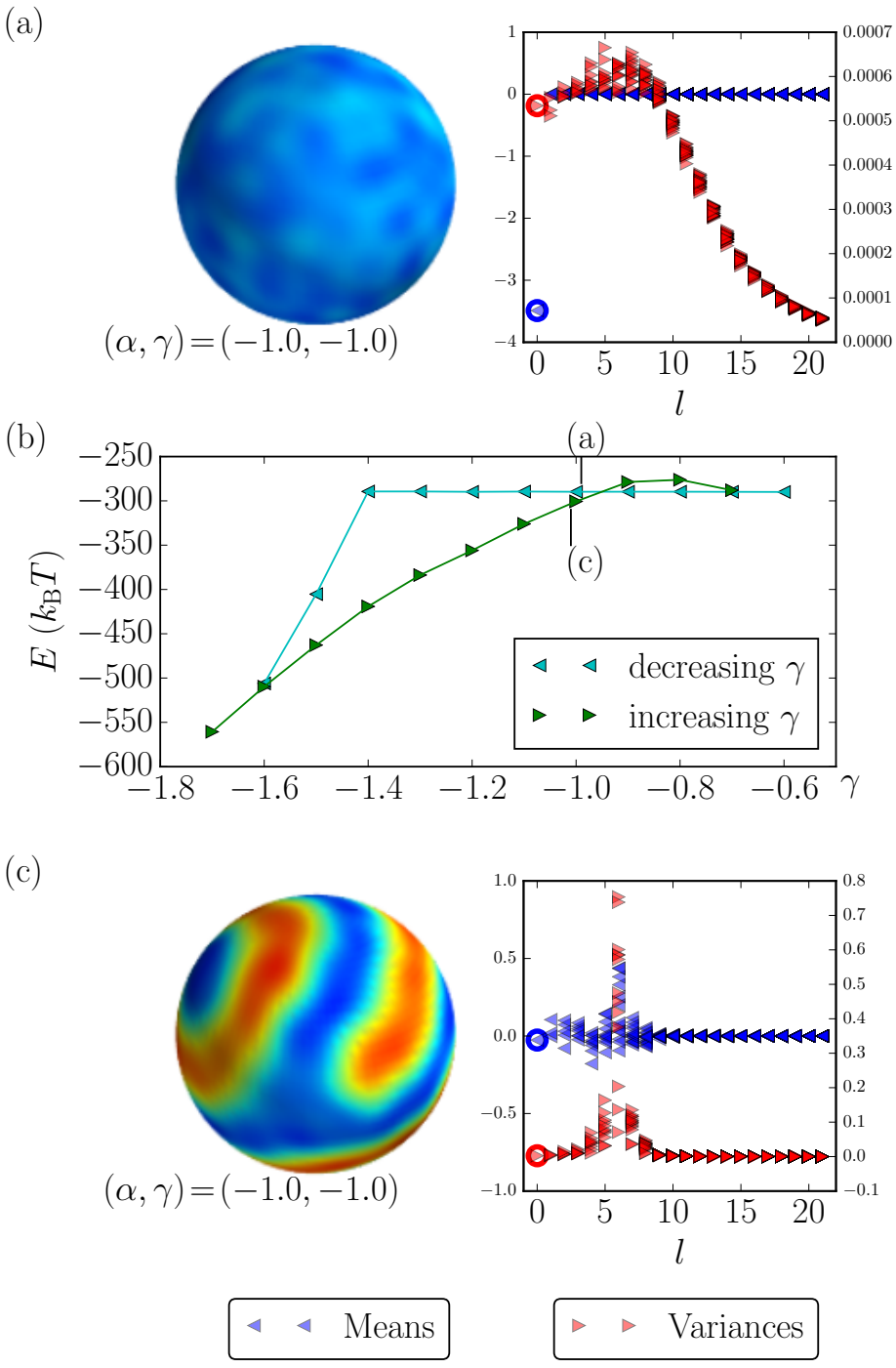


Figure 2.3: Phase indicators (surface patterns, means and variances of spherical harmonic modes as in Figure 2.2) of two possible phases at point (VII) ($\alpha = -1.0$, $\gamma = -1.0$) from phase diagram for $R = 10$ in Figure 2.1 (c). (a) is one of two coexisting phases and (c) is a modulated phase. (b) is the Landau-Ginzburg free energy hysteresis loop with $\alpha = -1.0$ and $\gamma$ increased or decreased across the phase boundary where free energies of (a) and (c) are marked. Circled in (a) and (c) are means and variances at $l = 0$, and scales and color schemes are the same as in Figure 2.2.

higher energy indicating a metastable modulated phase. But a first-order transition also happens at $\gamma = -0.7$, and the system reduces to the two-phase coexistence which is the global minimum at this point. The cross made by the two trends is identified as the location of the phase boundary, which is rounded to the nearest tenth $\gamma = -1.0$.

In addition to the first-order transition illustrated in Figure 2.3, some theoretical works made use of the Brazovskii theory[112] and predicted that the transition between an ordered modulated phase and a disordered microemulsion is also first-order at finite temperature as induced by thermal fluctuation[68]. This discontinuity, if it exists, is unnoticeable in our results because the transition does not show any sign of hysteresis, as this first-order character could be too weak to detect[113]. In this case there is no change in the average value of the order parameter across the transition, whereas in the case considered in Figure 2.3 the average changes discontinuously from zero in the modulated phase to $\pm\sqrt{-\alpha/b}$ in one of the coexisting microemulsion phases. The average of the order parameter can also be used to test the continuity of the transition from a homogeneous fluid to two-phase coexistence, where it changes continuously from zero to $\pm\sqrt{-\alpha/b}$ as $\alpha$ turns more negative.

### *2.4 Discussion*

Though the determination of a lateral phase in the ground state does not require the calculation of variances $\langle|\delta w_{l,m}|^2\rangle$ of spherical harmonic modes, we can still calculate them in analytical or numerical ways. We use the full-mode ground state Landau-Ginzburg expression (Equation (2.37)) and calculate a Hessian matrix whose elements are second derivatives of this energy $E$ with respect to $w_{l,0}$

$$H_{i,j} = \frac{\partial^2 E}{\partial w_{i,0} \partial w_{j,0}} \tag{2.44}$$

where integers $i$ and $j$ are between $l = 0$ and $l_{\max} = 21$. At each parameter set ($\alpha$, $\gamma$), to calculate the Hessian matrix, we can either analytically calculate the expression of $H_{i,j}$ in Mathematica and substitute $w_{l,0}$ modes with their ground state results. Another method that gives the same result is to evaluate $E$ at ($\alpha$, $\gamma$) with modes $w_{i,0}$ and $w_{j,0}$ slightly changed with

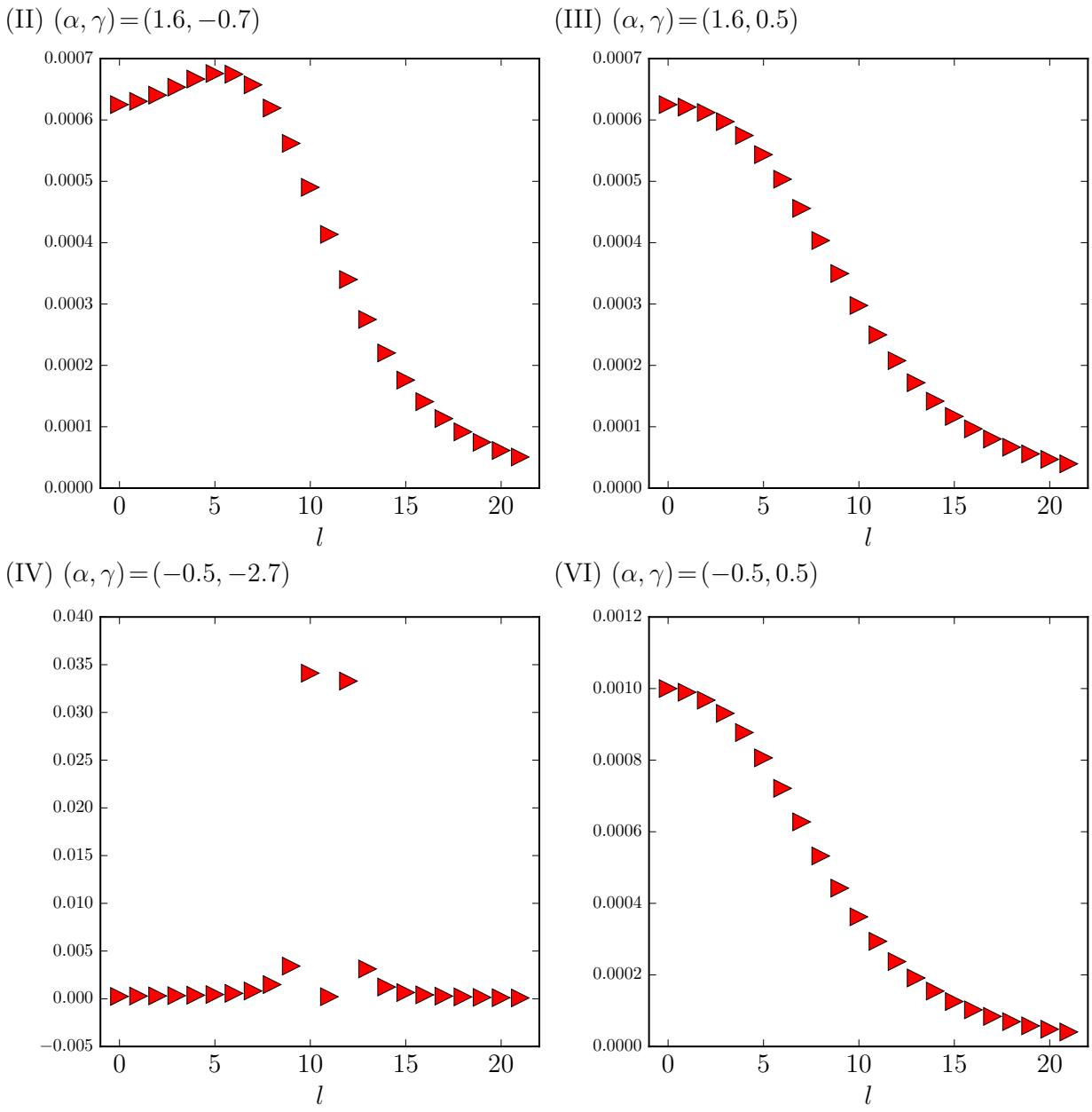


Figure 2.4: Analytical and numerical calculations of ground state spherical harmonic variances at points (II), (III), (IV) and (VI) in Figure 2.1 for $R = 10$. The ordinate is the variance $\langle |\delta w_{l,0}|^2 \rangle$ and the abscissa is the spherical harmonic degree $l$. The microemulsion (point (II)), homogeneous phase (point (III)) and two-phase coexistence (point (VI)) have similar patterns to Monte Carlo results. The modulated phase (point (IV)) shows a double-peak pattern, similar to the axisymmetric Monte Carlo result.

a small deviation $h_i$ and $h_j$ respectively, and then estimate each $H_{i,j}$ using the approximate expression as follows:

$$\frac{E(w_{i,0}+h_i, w_{j,0}+h_j) + E(w_{i,0}-h_i, w_{j,0}-h_j) - E(w_{i,0}+h_i, w_{j,0}-h_j) - E(w_{i,0}-h_i, w_{j,0}+h_j)}{4h_ih_j}. \tag{2.45}$$

Then we calculate the inverse of the Hessian matrix, whose diagonal elements multiplied by $k_{\mathrm{B}}T = 0.1$ are spherical harmonic variances of this system at ground state at the Monte Carlo temperature $T = 0.1$. Figure 2.4 shows examples of the resulting variances for radius $R = 10$ at points (II), (III), (IV) and (VI) in Figure 2.1. The results of the homogeneous phase (III), microemulsion (II) and a homogeneous phase of two-phase coexistence (VI) are comparable to the Monte Carlo simulations at finite temperature. The modulated phase (IV), however, illustrates a double-peak pattern in stark contrast to the simulation result. In fact, we find that if in a Monte Carlo simulation we also apply the constraint of $m = 0$ and make the system $\varphi$ independent, the modulated phase variance resulting from simulation also has two peaks, located at $l = l^* - 1$ and $l = l^* + 1$ while $l^*$ is the dominant spherical harmonic degree, which is exactly what we observe here in Figure 2.4. This is probably caused by the small change in $w_{l^*,0}$ in this axisymmetric system once it enters a stable modulated phase. It has a degenerate state in which all $w_{l,0}$ become $-w_{l,0}$, but both the calculation and axisymmetric Monte Carlo simulation with $m = 0$ are unable to sample both configurations and give a large variance in $w_{l^*,0}$, which on the other hand can be grasped by the regular non-axisymmetric Monte Carlo simulation.

A careful inspection of the inverse Hessian matrix at point (IV) ($\alpha = -0.5$, $\gamma = -2.7$) indicates that not only are there strong positive correlations between $w_{l^*-1,0}$ and itself, and between $w_{l^*+1,0}$ and itself (illustrated by variances $\langle|w_{l^*-1,0}|^2\rangle$ and $\langle|w_{l^*+1,0}|^2\rangle$ respectively), but also there is a strong negative correlation between $w_{l^*-1,0}$ and $w_{l^*+1,0}$ (as illustrated by covariance $\langle w_{l^*-1,0}w_{l^*+1,0}\rangle$). Figure 2.5 shows the matrix multiplied by $k_{\mathrm{B}}T = 0.1$, each element of which at ($l_1$, $l_2$) is equal to $\langle w_{l_1,0}w_{l_2,0}\rangle$. The diagonal elements are the variances shown in Figure 2.4 (IV). Besides the positive variance peaks at $l_1 = l_2 = l^* - 1 = 10$ and

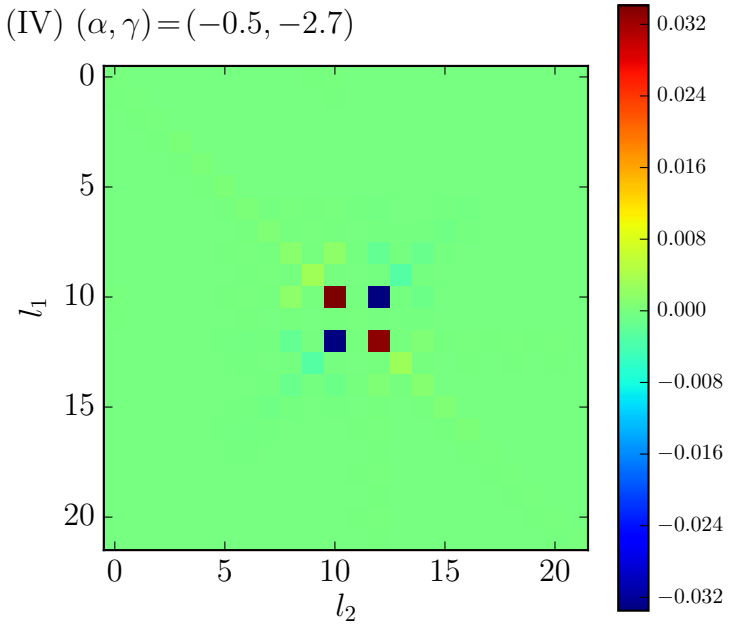


Figure 2.5: Inverse Hessian matrix multiplied by $k_{\mathrm{B}}T = 0.1$ calculated analytically, at point (IV) from Figures 2.1, 2.2 and 2.4. Both ordinate and abscissa are spherical harmonic degrees $l$. The elements are variances ($l_1 = l_2$) or covariances ($l_1 \neq l_2$) of spherical harmonic modes $w_{l,0}$ . The correlations at $l_1 = l_2 = l^* - 1$ and $l_1 = l_2 = l^* + 1$ are strongly positive, and the correlation between $l^* - 1$ and $l^* + 1$ is strongly negative, making the variance $\langle |w_{l^*,0}|^2 \rangle \approx 0$.

$l_1 = l_2 = l^* + 1 = 12$, there are two relatively very negative values at ($l_1 = l^* - 1$, $l_2 = l^* + 1$) and ($l_1 = l^* + 1$, $l_2 = l^* - 1$), which means the covariance $\langle w_{l^*-1,0} w_{l^*+1,0} \rangle$ is strongly negative, making two "pits" in the range of the matrix. Because of the positive variances at ($l^* - 1$, $l^* - 1$) and ($l^* + 1$, $l^* + 1$) and negative covariances of ($l^* - 1$, $l^* + 1$) and ($l^* + 1$, $l^* - 1$), the variance $\langle |w_{l^*,0}|^2 \rangle$ at $l_1 = l_2 = l^* = 11$ is nearly 0.

An advantage of the numerical approximation (Expression (2.45)) is that it can be used for an azimuthal $\varphi$ and spherical harmonic degree $m$ dependent situation, where $E$ is described by Equation (2.32) and the Hessian matrix element $\partial^2 E / (\partial w_{l_1,m_1} \partial w_{l_2,m_2})$ can be evaluated for any two $w_{l,m}$ modes in the full expression using a similar approximation, by replacing $w_{i,0}$ and $w_{j,0}$ with $w_{l_1,m_1}$ and $w_{l_2,m_2}$. This is then used for further calculating the inverse of the Hessian matrix and the spherical harmonic variance without the $m = 0$ constraint. This

may be able to reproduce the single-peak variances from regular Monte Carlo simulations. There are also more observations about modulated phase variances calculated in the full, non-axisymmetric situation, but this analysis is beyond the scope of this discussion.

The variation of phase diagrams and especially phase transition boundaries caused by the presence of thermal fluctuations at finite temperature is remarkable in the contrast of Figure 2.1 (b) and (c). One of the most important observations is the split of the triple point that leads to a new phase boundary presenting a direct transition between microemulsion and two-phase coexistence. This was initially captured in the planar case[114] and recently confirmed by a simulation work[115]. Among these phase diagrams of spheres of diverse sizes, we observe the resemblance of these phase phenomena to those on a planar surface when the radius is large, and how the finite size affects the diagrams most remarkably at a small radius. The emergence of the microemulsion region and the shift of Lifshitz line (the vertical boundary between homogeneous and microemulsion regions in a phase diagram) are caused by both effects. One way to estimate the shift is to establish a further simplified Landau-Ginzburg free energy model by having $b = 0$ in the extended Landau-Ginzburg free energy expression in Equation (2.18) for the homogeneous and modulated regions. See details in Chapter 3 for the use of this "Gaussian" model in the calculation of structure factors. Without the quartic term, Equation (2.32) is reduced to a homogeneous sum of squares of spherical harmonic modes $|w_{l,m}|^2$ with positive parameters $\alpha$ and $\epsilon$, which would stabilize the system even at $b = 0$. From the equipartition theorem, we express the variance of spherical harmonic modes of the order parameter as a function of integer $l$ in terms of the thermal energy scale $k_{\mathrm{B}}T$ as (see derivation in Chapter 3)

$$\mathrm{Var}(l) = \left\langle |w_{l,m}|^2 \right\rangle = \frac{k_{\mathrm{B}}T}{\alpha R^2 + \gamma l(l+1) + \epsilon[l(l+1)]^2/R^2}. \tag{2.46}$$

We expect to see a monotonically decreasing variance in the homogeneous phase, and a variance peaked at some nonzero $l$ in a microemulsion. The former has $\mathrm{Var}(0) > \mathrm{Var}(1)$, and the latter must have $\mathrm{Var}(0) < \mathrm{Var}(1)$. The boundary between the two states, the Lifshitz

line, is then solved by having Var(0) = Var(1) and turns out to be

$$\gamma = -\frac{2\epsilon}{R^2} \tag{2.47}$$

according to the Gaussian model. This theoretical boundary calculated from the simplification is then $\gamma = -2$ for $R = 1$, $\gamma = -2/9$ for $R = 3$ and $\gamma = -1/50$ for $R = 10$, quantitatively verifying the locations of Lifshitz line as $R$ varies, which are from the full extended Landau-Ginzburg model with thermal fluctuations.

For an analogous finite size effect on a flat patch, the modulated phase critical wave vector $k^* = \sqrt{-\gamma/(2\epsilon)}$ (Equation (2.12)) when $\gamma < 0$ as defined in [70] also determines the length scale of microemulsion fluctuations on a planar surface. However, this wave vector is accurate when the surface is infinitely large, and it is only an estimate at a finite edge length $L$. It is based on the variance of the Fourier mode $\tilde{\phi}(\boldsymbol{k})$ of order parameter $\phi(\boldsymbol{r})$ on the flat patch, which is related to the two-dimensional structure factor which can be calculated from a flat Gaussian model with $b = 0$ in the extended Landau-Ginzburg free energy[109]

$$S(k) = \frac{1}{L^2}\left\langle |\tilde{\phi}(k)|^2 \right\rangle = \frac{k_{\mathrm{B}}T}{\alpha + \gamma k^2 + \epsilon k^4}. \tag{2.48}$$

When $\gamma > 0$ the structure factor monotonically decreases with $k$ and it is required to be nonnegative so that it has a maximum at $k = 0$, indicating that the system is homogeneous; and when $\gamma < 0$ it shows a peak at the nonzero $k^* = \sqrt{-\gamma/(2\epsilon)}$, indicating that the system is a microemulsion with a characteristic half wavelength $\lambda^* = \pi/k^*$.

When $L$ is finite $k$ is no longer continuous because $\boldsymbol{k} = (2\pi i/L, 2\pi j/L)$ as in Equation (2.8) where $i$ and $j$ are integers and so its magnitude is $k = 2\pi\sqrt{i^2 + j^2}/L$. We can evaluate Equation (2.48) at $k = 0$ and at the smallest nonzero $k = 2\pi/L$ and compare them. If $S(0) > S(2\pi/L)$ then $S(k)$ has a maximum at $k = 0$ and the system is homogeneous even if $\gamma < 0$, and this happens when $\gamma > -4\pi^2\epsilon/L^2$. On the other hand, if $S(0) < S(2\pi/L)$ then $S(k)$ has a peak at some nonzero $k$ and the system is a microemulsion, which happens at $\gamma < -4\pi^2\epsilon/L^2$. So we find the more accurate homogeneous-microemulsion boundary at finite size $L$ at

$$\gamma = -\frac{4\pi^2\epsilon}{L^2} \tag{2.49}$$

which shifts from the infinitely large patch limit $\gamma = 0$[70], and proves that this kind of finite size effect also exists in planar geometry. Additionally, with certain Landau-Ginzburg parameters ($\gamma < 0$), we may find the system in a microemulsion if $L > 2\pi\sqrt{-\epsilon/\gamma}$ (the other condition for Equation (2.48) to be peaked), while it may become homogeneous when $L < 2\pi\sqrt{-\epsilon/\gamma}$ because the system is too small to accommodate the correlation length scale of phase fluctuations determined by Landau-Ginzburg parameters.

Similarly, in the spherical case we can rewrite Equation (2.47) in a different form

$$R = \sqrt{-\frac{2\epsilon}{\gamma}} \tag{2.50}$$

which represents the other aspect of finite size effect of a sphere. When the radius is larger than this threshold, we would expect the system to be a microemulsion if $\gamma < 0$, and if it is smaller than the threshold we expect a homogeneous phase, which means the sphere is too small to accommodate phase fluctuations of a particular size. Interestingly, the same critical radius can also be predicted by our exploration of the structure factor of a Gaussian sphere, where the structure factor monotonically decreases with wave vector magnitude $k$ when $R$ is smaller than this and shows a peak at nonzero wave vector when $R$ is larger[109]; see Chapter 3 for details. In conclusion, the intrinsic finite size effect of a spherical surface is most pronounced when its radius is small, which could affect the determination of lateral phase even when internal structures and compositions are unchanged as represented by Landau-Ginzburg parameters.

The threshold radius for a microemulsion is one of many detectable properties in various experiments, which reveal the physical meanings and values of the phenomenological parameters used in our model. The same scattering experiment can measure the location (wave vector) of the structure factor's first peak, which is approximately $k^* = \sqrt{-\gamma/(2\epsilon)}$. The characteristic half wavelength $\lambda^* = \pi/k^*$ is also measurable by either a direct observation in optical microscopy or a measurement of spatial autocorrelation (for example in Reference [54]). It has been more common to test the system's phase separation temperature $T_c$ (for example in Reference [116]), which is linearly related to $\alpha = a(T - T_c)$ at temperature $T$

where constant $a > 0$. Otherwise, the line tension determined by (2.3) can also be directly measured in spectroscopy[117].

Later, we expand our study beyond the restriction of an ideal spherical surface of a constant radius to a closed surface deformed from sphere, which also has intrinsic finite size and may involve a wider variety of lateral phase behaviors due to deformations. In Chapter 4, we illustrate the coupling of the surface order parameter and lateral phases to the bending rigidity and spontaneous curvature of the surface. The membrane thickness, however, becomes sizable and comparable to the radius of sphere if the spherical size is small enough, and may furthermore reinforce the intrinsic finite size effect of a spherical surface. Hence, we suggest the necessity of taking into account the effects of finite size when considering phase formation and separation on a lipid-bilayer versicle, especially in comparison of theoretical and simulation results (mostly from membrane patch model with planar geometry) and experiments (mostly on closed vesicles with a spherical geometry, many of which are small).

# Chapter 3

# TWO- AND THREE-DIMENSIONAL STRUCTURE FACTORS OF LIPID MEMBRANES AND THEIR MODEL-FREE RELATIONSHIP

In this chapter we make use of the simplified "Gaussian" form of the extended Landau-Ginzburg model mentioned in Section 2.4 to calculate the two-dimensional scattering structure factor of a planar lipid membrane and the three-dimensional structure factor of a spherical lipid vesicle. We consider the 2D and 3D structure factors as proportional to the ensemble averaged squares of Fourier transforms of the compositional order parameters on a planar surface embedded in a two-dimensional space, or on a spherical surface embedded in a three-dimensional space, respectively. These are idealized properties for rigid planes or spheres which are simplified from soft, deformable lipid membranes, and we continue to consider a more idealized model of infinitely large planar or spherical surfaces. We develop a model-independent, approximate mathematical relationship between the 2D structure factor of a large planar surface and the 3D structure factor of an equally large spherical surface made of the same two-dimensional material, not necessarily a lipid bilayer or the Gaussian model. The comparison turns out to be accurate in the ideal situation of infinitely large surfaces, and is less effective at a small size.

## *3.1 Two- and three-dimensional Fourier transforms of the order parameter and calculation of structure factors*

The Gaussian model, as a functional of order parameter $\phi(\boldsymbol{r})$, is defined on a surface $S$

$$E[\phi(\boldsymbol{r})] = \int \mathrm{d}S \left\{ \frac{\alpha}{2} \left|\phi(\boldsymbol{r})\right|^2 + \frac{\gamma}{2} \left|\nabla\phi(\boldsymbol{r})\right|^2 + \frac{\epsilon}{2} \left|\nabla^2\phi(\boldsymbol{r})\right|^2 \right\} \tag{3.1}$$

with Landau-Ginzburg parameters $\alpha$, $\gamma$ and $\epsilon$ as in Equation (2.5). Under quadratic analysis, all terms in the integral are second-order and the quartic term in Equation (2.5) is removed, so $E[\phi(\boldsymbol{r})]$ is a homogeneous quadratic functional. The removal of the quartic term is allowed when the system is in a homogeneous phase or a microemulsion state (see Chapter 2), while in a two-phase coexistence or a modulated phase the system energy would diverge to negative infinity without the quartic term.

The calculation of structure factors requires the Fourier transform of the order parameter, which is defined differently in a two-dimensional space or in a three-dimensional space. For the sake of clarity, we use the notation $\boldsymbol{s}$ for a 2D vector marking a point in a 2D space, and $\boldsymbol{r}$ for a 3D vector marking a point in a 3D space. Similarly, we use $\boldsymbol{q}$ to denote a 2D wave vector in the 2D space and $\boldsymbol{k}$ to denote a 3D wave vector in the 3D space. Then the two-dimensional Fourier transform of $\phi(\boldsymbol{s})$ in a planar surface is

$$\tilde{\phi}(\boldsymbol{q}) = \int \mathrm{d}\boldsymbol{s}\, \phi(\boldsymbol{s}) e^{-i\boldsymbol{q}\cdot\boldsymbol{s}}. \tag{3.2}$$

For a flat square of edge length $L$, the 2D structure factor is

$$S^{(2\mathrm{d})}(\boldsymbol{q}) = \frac{1}{L^2}\left\langle |\tilde{\phi}(\boldsymbol{q})|^2 \right\rangle \tag{3.3}$$

where $\langle\cdot\rangle$ denotes the ensemble thermal equilibrium average. In terms of Fourier modes $\tilde{\phi}(\boldsymbol{q})$, the planar form of Equation (3.1)

$$E[\phi(\boldsymbol{s})] = \int \mathrm{d}S \left\{ \frac{\alpha}{2} |\phi(\boldsymbol{s})|^2 + \frac{\gamma}{2} |\nabla\phi(\boldsymbol{s})|^2 + \frac{\epsilon}{2} \left|\nabla^2\phi(\boldsymbol{s})\right|^2 \right\} \tag{3.4}$$

is transformed into (See Equation (2.7))

$$E = \frac{1}{2L^2} \sum_{\boldsymbol{q}} (\alpha + \gamma q^2 + \epsilon q^4) |\tilde{\phi}(\boldsymbol{q})|^2 \tag{3.5}$$

in which $\boldsymbol{q} = (2\pi i/L, 2\pi j/L)$ (Equation (2.8)) and each degree of freedom contributes $(\alpha + \gamma q^2 + \epsilon q^4)|\tilde{\phi}(\boldsymbol{q})|^2/(2L^2)$ to the total energy. It is observed that $\boldsymbol{q}$ and $-\boldsymbol{q}$ are coupled through complex conjugates because $\phi$ is real-valued

$$\tilde{\phi}(\boldsymbol{q}) = \tilde{\phi}^*(-\boldsymbol{q}). \tag{3.6}$$

According to the equipartition theorem in statistical thermodynamics, with thermal fluctuation at temperature $T$, the contribution of each degree of freedom is equal to half the thermal energy scale $k_{\mathrm{B}}T$ on average,

$$\left\langle \frac{1}{2L^2}(\alpha + \gamma q^2 + \epsilon q^4)|\tilde{\phi}(\boldsymbol{q})|^2 \right\rangle = \frac{k_{\mathrm{B}}T}{2}, \tag{3.7}$$

so the 2D structure factor (Equation (3.3)) becomes

$$S^{(2\mathrm{d})}(\boldsymbol{q}) = \frac{k_{\mathrm{B}}T}{\alpha + \gamma q^2 + \epsilon q^4}. \tag{3.8}$$

The structure factor depends only on the magnitude of the wave vector $q$ and is denoted by $S^{(2\mathrm{d})}(q)$. This is not surprising for an isotropic two-dimensional material in a homogeneous or microemulsion state.

The 3D structure factor depends on the three-dimensional Fourier transform

$$\tilde{\rho}(\boldsymbol{k}) = \int \mathrm{d}\boldsymbol{r}\, \rho(\boldsymbol{r}) e^{-i\boldsymbol{k}\cdot\boldsymbol{r}}. \tag{3.9}$$

where $\rho$ is the embedding of $\phi$ in a 3D space. The 3D structure factor is defined as

$$S^{(\mathrm{sph})}(\boldsymbol{k}) = \frac{1}{4\pi R^2} \left\langle |\tilde{\rho}(\boldsymbol{k})|^2 \right\rangle \tag{3.10}$$

for a sphere of radius $R$ in our discussion. Like $S^{(2\mathrm{d})}(q)$, it is also demonstrated later that the 3D structure factor is also a function of the magnitude of wave vector $k$ and is then written as $S^{(\mathrm{sph})}(k)$. Examples of both $S^{(2\mathrm{d})}(q)$ and $S^{(\mathrm{sph})}(k)$ are given in Figure 3.1 for the comparison of different geometries and dimensionalities.

### *3.1.1 Two-dimensional structure factor of a disk*

In order to calculate $S^{(\mathrm{sph})}(k)$, we consider the calculation of $S^{(2\mathrm{d})}(q)$ in a circular plane or a disk of radius $R$. In a polar coordinate system, the basis set is defined as[107]

$$\Psi_{n,m}(r,\varphi) = \frac{1}{\sqrt{2\pi N_n^{(m)}}} J_m(q_{n,m} r) e^{im\varphi} \tag{3.11}$$

in which $J_m$ is a Bessel function, and $n$ and $m$ are integers. Both $q_{n,m}$ and $N_n^{(m)}$ are parameters dependent on $n$ and $m$. The order parameter is expanded in terms of the basis functions as

$$\phi(\boldsymbol{s}) = \phi(r,\varphi) = \sum_{n=1}^{\infty}\sum_{m=-\infty}^{\infty} P_{n,m}\Psi_{n,m}(r,\varphi) \equiv \sum_{n,m} P_{n,m}\Psi_{n,m}(r,\varphi). \tag{3.12}$$

The basis functions satisfy

$$\int_0^R r\mathrm{d}r \int_0^{2\pi} \mathrm{d}\varphi\, \Psi^*_{n,m}(r,\varphi)\Psi_{n',m'}(r,\varphi) = \delta_{n,n'}\delta_{m,m'} \tag{3.13}$$

$$\nabla^2\Psi_{n,m}(r,\varphi) = -q^2_{n,m}\Psi_{n,m}(r,\varphi). \tag{3.14}$$

Similar to Equations (2.25)–(2.27), we have

$$\int r\mathrm{d}r\mathrm{d}\varphi\ |\phi|^2 = \int r\mathrm{d}r\mathrm{d}\varphi\, \phi^*\phi = \sum_{n,m}|P_{n,m}|^2 \tag{3.15}$$

$$\int r\mathrm{d}r\mathrm{d}\varphi\, |\nabla\phi|^2 = -\int r\mathrm{d}r\mathrm{d}\varphi\, \phi^*\nabla^2\phi = \sum_{n,m} q^2_{n,m}|P_{n,m}|^2 \tag{3.16}$$

$$\int r\mathrm{d}r\mathrm{d}\varphi\ \left|\nabla^2\phi\right|^2 = \int r\mathrm{d}r\mathrm{d}\varphi\, (\nabla^2\phi)^*\nabla^2\phi = \sum_{n,m} q^4_{n,m}|P_{n,m}|^2. \tag{3.17}$$

The free energy functional (Equation (3.4)) is rewritten as

$$E = \frac{1}{2}\sum_{n,m}(\alpha + \gamma q^2_{n,m} + \epsilon q^4_{n,m})|P_{n,m}|^2. \tag{3.18}$$

According to the equipartition theorem we have

$$\left\langle \frac{1}{2}(\alpha + \gamma q^2_{n,m} + \epsilon q^4_{n,m})|P_{n,m}|^2 \right\rangle = \frac{k_\mathrm{B}T}{2} \tag{3.19}$$

in each degree of freedom, and the ensemble averaged square of coefficient $P_{n,m}$ is

$$\left\langle |P_{n,m}|^2 \right\rangle = \frac{k_\mathrm{B}T}{\alpha + \gamma q^2_{n,m} + \epsilon q^4_{n,m}}. \tag{3.20}$$

More generally we have

$$\left\langle P^*_{n,m}P_{n',m'} \right\rangle = \frac{k_\mathrm{B}T}{\alpha + \gamma q^2_{n,m} + \epsilon q^4_{n,m}}\delta_{n,n'}\delta_{m,m'}. \tag{3.21}$$

We further use the plane wave basis set expansion in Bessel functions (assuming zero boundary condition for the determination of $q_{n,m}$; see Reference [107])

$$e^{i\boldsymbol{q}\cdot\boldsymbol{s}} = \sum_{n',m'} 2\sqrt{\pi}(-1)^{n'} i^{m'} q_{n',m'} \frac{J_{m'}(qR)}{q^2 - q_{n',m'}^2} e^{-im'\varphi_q} \Psi_{n',m'}(r,\varphi) \tag{3.22}$$

in which $\boldsymbol{q} = (q, \varphi_q)$. We derive the Fourier transform

$$\begin{aligned}
\tilde{\phi}(\boldsymbol{q}) &= \int_0^R r\mathrm{d}r \int_0^{2\pi} \mathrm{d}\varphi\, \phi(r,\varphi) e^{-i\boldsymbol{q}\cdot\boldsymbol{s}} \\
&= \sum_{n,m} \sum_{n',m'} 2\sqrt{\pi} P_{n,m} (-1)^{n'} (-i)^{m'} q_{n',m'} \frac{J_{m'}(qR)}{q^2 - q_{n',m'}^2} e^{im'\varphi_q} \delta_{n,n'} \delta_{m,m'} \\
&= \sum_{n,m} 2\sqrt{\pi} P_{n,m} (-1)^{m+n} i^m q_{n,m} \frac{J_m(qR)}{q^2 - q_{n,m}^2} e^{im\varphi_q}
\end{aligned} \tag{3.23}$$

Then the 2D structure factor of the disk is

$$\begin{aligned}
S^{(2\mathrm{d})}(q) &= \frac{1}{\pi R^2} \left\langle \tilde{\phi}^*(\boldsymbol{q}) \tilde{\phi}(\boldsymbol{q}) \right\rangle \\
&= \frac{4}{R^2} \sum_{n,m} \sum_{n',m'} \left\langle P_{n,m}^* P_{n',m'} \right\rangle (-1)^{m'+n'+n} i^{m+m'} q_{n,m} q_{n',m'} \frac{J_m(qR) J_{m'}(qR)}{(q^2 - q_{n,m}^2)(q^2 - q_{n',m'}^2)} e^{i(m'-m)\varphi_q} \\
&= \frac{4}{R^2} \sum_{n,m} \frac{k_\mathrm{B}T}{\alpha + \gamma q_{n,m}^2 + \epsilon q_{n,m}^4} q_{n,m}^2 \frac{J_m(qR)^2}{(q^2 - q_{n,m}^2)^2}.
\end{aligned} \tag{3.24}$$

The limit of this result as $R \to \infty$ might be equal to the result for a planar square (Equation (3.8)). This could be an alternative method to derive the 2D structure factor.

### *3.1.2 Three-dimensional structure factor of a sphere*

We use an approach similar to the disk structure factor calculation to find the 3D structure factor. In a three-dimensional space, the Gaussian model is the one discussed in Section 2.4, which is Equation (2.18) without the quartic term:

$$E[\phi(\theta,\varphi)] = R^2 \int \mathrm{d}\Omega \left\{ \frac{\alpha}{2} |\phi(\theta,\varphi)|^2 + \frac{\gamma}{2} |\nabla\phi(\theta,\varphi)|^2 + \frac{\epsilon}{2} \left|\nabla^2\phi(\theta,\varphi)\right|^2 \right\}. \tag{3.25}$$

Here, $\phi(\theta,\varphi)$ is the surface order parameter of a sphere of radius $R$, whose embedding in 3D space is

$$\rho(\boldsymbol{r}) = \rho(r,\theta,\varphi) = \phi(\theta,\varphi)\delta(r-R) = \sum_{l,m} w_{l,m} Y_{l,m}(\theta,\varphi)\delta(r-R) \tag{3.26}$$

where the spherical harmonic coefficients $w_{l,m}$ are the same as in Chapter 2. We have obtained (see Equation (2.32))

$$E = \frac{R^2}{2}\sum_{l,m}\left\{\alpha + \frac{\gamma}{R^2}l(l+1) + \frac{\epsilon}{R^4}[l(l+1)]^2\right\}|w_{l,m}|^2. \tag{3.27}$$

By applying the equipartition theorem, in each degree of freedom

$$\left\langle \frac{R^2}{2}\left\{\alpha + \frac{\gamma}{R^2}l(l+1) + \frac{\epsilon}{R^4}[l(l+1)]^2\right\}|w_{l,m}|^2 \right\rangle = \frac{k_{\mathrm{B}}T}{2} \tag{3.28}$$

and we have

$$\left\langle |w_{l,m}|^2 \right\rangle = \frac{k_{\mathrm{B}}T}{\alpha R^2 + \gamma l(l+1) + \epsilon[l(l+1)]^2/R^2} \tag{3.29}$$

or more generally

$$\left\langle w^*_{l,m} w_{l',m'} \right\rangle = \frac{k_{\mathrm{B}}T}{\alpha R^2 + \gamma l(l+1) + \epsilon[l(l+1)]^2/R^2}\delta_{l,l'}\delta_{m,m'}. \tag{3.30}$$

The plane wave basis set expansion in spherical harmonics is[107]

$$e^{-i\boldsymbol{k}\cdot\boldsymbol{r}} = 4\pi\sum_{l',m'}(-i)^{l'} j_{l'}(kr) Y^*_{l',m'}(\theta,\varphi) Y_{l',m'}(\theta_k,\varphi_k) \tag{3.31}$$

where the three-dimensional wave vector $\boldsymbol{k} = (k,\theta_k,\varphi_k)$ and $j_{l'}(kr)$ is the spherical Bessel function. The 3D Fourier transform can thus be written as

$$\begin{aligned}
\tilde{\rho}(\boldsymbol{k}) &= \int \mathrm{d}r\mathrm{d}\theta\mathrm{d}\varphi\, r^2 \sin\theta \rho(r,\theta,\varphi) e^{-i\boldsymbol{k}\cdot\boldsymbol{r}} \\
&= 4\pi R^2 \int_0^{2\pi} d\varphi \int_0^{\pi} \sin\theta d\theta \sum_{l,m} w_{l,m} Y_{l,m}(\theta,\varphi) \sum_{l',m'} (-i)^{l'} j_{l'}(kR) Y^*_{l',m'}(\theta,\varphi) Y_{l',m'}(\theta_k,\varphi_k) \\
&= 4\pi R^2 \sum_{l,m}\sum_{l',m'} w_{l,m}(-i)^{l'} j_{l'}(kR) Y_{l',m'}(\theta_k,\varphi_k)\delta_{l,l'}\delta_{m,m'} \\
&= 4\pi R^2 \sum_{l,m} w_{l,m}(-i)^{l} j_{l}(kR) Y_{l,m}(\theta_k,\varphi_k).
\end{aligned} \tag{3.32}$$

Finally we calculate the 3D structure factor (Equation (3.10))

$$\begin{aligned} S^{(\mathrm{sph})}(k) &= \frac{1}{4\pi R^2}\left\langle \tilde{\rho}^*(\boldsymbol{k})\tilde{\rho}(\boldsymbol{k})\right\rangle = \frac{1}{4\pi R^2}\left\langle \tilde{\rho}(\boldsymbol{k})\tilde{\rho}(-\boldsymbol{k})\right\rangle \\ &= 4\pi R^2 \sum_{l,m}\sum_{l',m'} (-i)^{l+l'} Y_{l,m}(\theta_k,\varphi_k) Y_{l',m'}(\pi-\theta_k,\varphi_k+\pi) j_l(kR) j_{l'}(kR) \left\langle w^*_{l,m} w_{l',m'}\right\rangle \\ &= 4\pi R^2 k_{\mathrm{B}}T \sum_{l=0}^{\infty} \frac{j_l(kR)^2}{\alpha R^2 + \gamma l(l+1) + \epsilon[l(l+1)]^2/R^2} \sum_{m=-l}^{l} Y_{l,m}(\theta_k,\varphi_k) Y_{l,m}(\pi-\theta_k,\varphi_k+\pi) \end{aligned} \tag{3.33}$$

which means

$$S^{(\mathrm{sph})}(k) = k_{\mathrm{B}}T \sum_{l=0}^{\infty} \frac{(2l+1) j_l(kR)^2}{\alpha + \gamma l(l+1)/R^2 + \epsilon[l(l+1)]^2/R^4}, \tag{3.34}$$

where we use Unsöld's theorem

$$\sum_{m=-l}^{l} Y_{l,m}(\theta_k,\varphi_k) Y_{l,m}(\pi-\theta_k,\varphi_k+\pi) = \frac{2l+1}{4\pi}. \tag{3.35}$$

### *3.1.3 Qualitative comparisons of two- and three-dimensional structure factors*

Plots of 2D and 3D structure factors are included in Figure 3.1, where for simplicity the phenomenological parameters $k_{\mathrm{B}}T = \alpha = \epsilon = 1$ and $\gamma = \pm 1$. The summation in Equation (3.34) is processed over $l = 0$ to $l_{\max} = 100$. In both dimensionalities the structure factor decreases monotonically with the wave vector or shows a single maximum at a certain wave vector, with a positive or a negative $\gamma$ respectively. This observation is not always correct, since there are some exceptions. The scattering structure factor is always positive, which means the denominators in Equations (3.8) and (3.34) are required to be positive, and $\gamma$ is not allowed to be too negative, or the Gaussian model would be no longer applicable in this calculation. A sufficient condition is

$$\gamma > -2\sqrt{\alpha\epsilon}. \tag{3.36}$$

With this condition, the 2D structure factor $S^{(\mathrm{2d})}(q)$ decreases monotonically with $q$ when $\gamma > 0$, indicating a homogeneous phase, or shows a single-peak pattern whose maximum

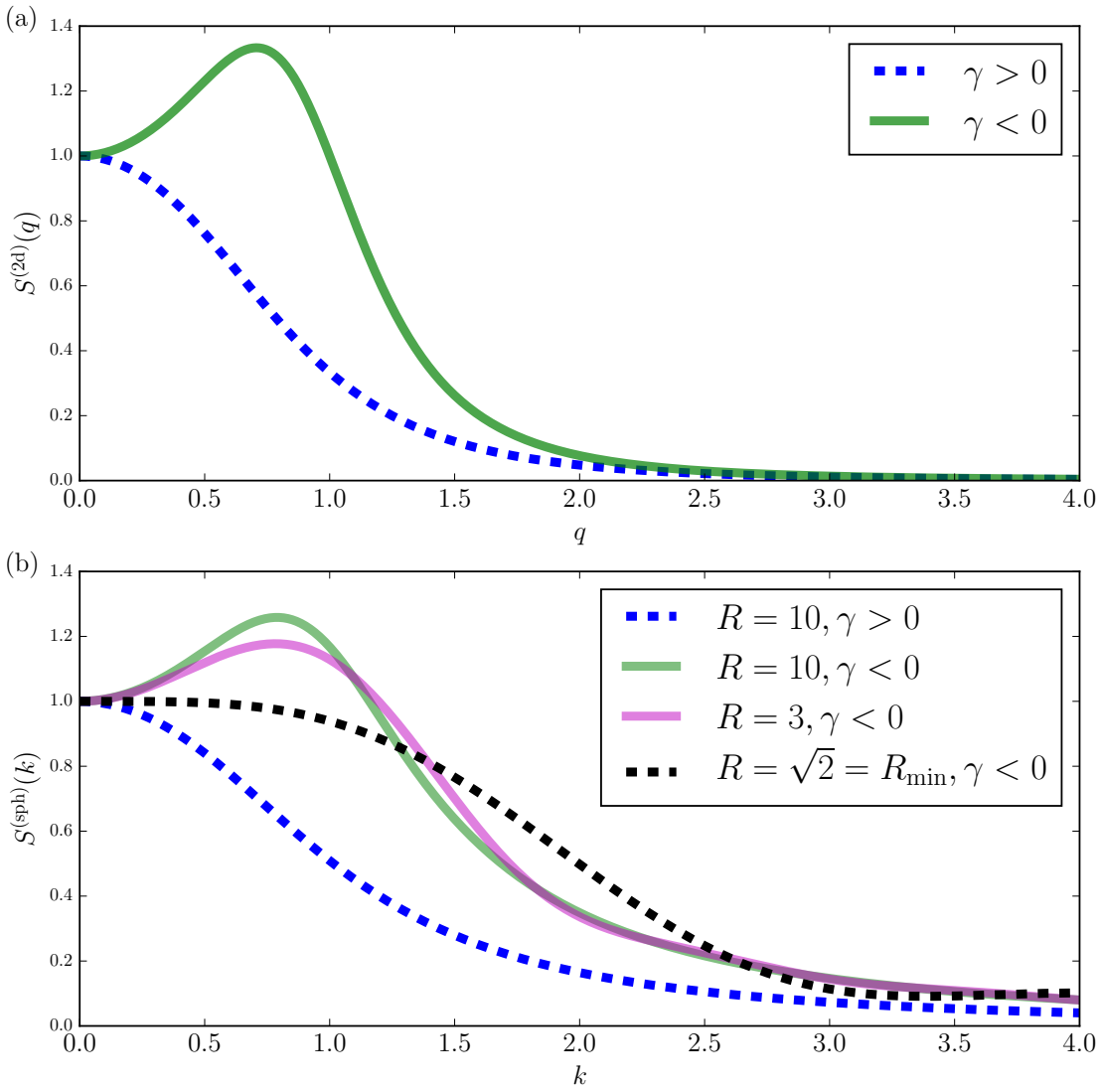


Figure 3.1: Two- and three-dimensional structure factors (Equations (3.8) and (3.34)). Here $q$ is the magnitude of a 2D wave vector, and $k$ is that of a 3D wave vector. We use parameters $l_{\max} = 100$, $k_{\mathrm{B}}T = \alpha = \epsilon = 1$ and $\gamma = 1$ or $-1$. (a) The structure factor $S^{(2d)}(q)$ of a large plane where $q$ is nearly continuous. (b) The structure factor $S^{(sph)}(k)$ of spherical surface varying with the spherical size. When $\gamma > 0$, both 2D and 3D structure factors indicate a homogeneous phase, and when $\gamma < 0$, they mostly indicate a microemulsion, except for $R = \sqrt{2} = R_{\min}$.

is located at $q = \sqrt{-\gamma/(2\epsilon)}$ when $\gamma < 0$, indicating a microemulsion with dominant wave vector $k^* = \sqrt{-\gamma/(2\epsilon)}$ (see calculation and discussion in Chapter 2), if the planar surface is large enough and $q$ is nearly continuous. However, at a finite size the planar surface may not be able to accommodate the transient phase fluctuation of a microemulsion, and would show a monotonically decreasing $S^{(2d)}(q)$ with discrete $q$ even when $\gamma < 0$. For a square plane, its edge size $L$ has to be $L > 2\pi\sqrt{-\epsilon/\gamma}$ to be able to show a microemulsion state. See Section 2.4 for details of this two-dimensional finite size effect.

As for 3D structure factors, a finite size effect also exists. We can calculate the zeroth, first and second derivatives of $S^{(\mathrm{sph})}(k)$ at the limit of $k \to 0$ as follows

$$S^{(\mathrm{sph})}(k \to 0) = \frac{k_\mathrm{B}T}{\alpha} \tag{3.37}$$

$$\left.\frac{\mathrm{d}S^{(\mathrm{sph})}}{\mathrm{d}k}\right|_{k\to 0} = 0 \tag{3.38}$$

$$\left.\frac{\mathrm{d}^2S^{(\mathrm{sph})}}{\mathrm{d}k^2}\right|_{k\to 0} = -\frac{2k_\mathrm{B}TR^2(2\gamma/R^2 + 4\epsilon/R^4)}{3\alpha(\alpha + 2\gamma/R^2 + 4\epsilon/R^4)}. \tag{3.39}$$

The first two equations match the observation of Figure 3.1. The last equation indicates that when $\gamma > 0$, the second derivative is negative near $k = 0$, and this is a necessary condition for $S^{(\mathrm{sph})}(k)$ to monotonically decrease with increasing $k$ and for the system to behave as a homogeneous fluid. When $\gamma < 0$, the second derivative is equal to 0 when

$$R = \sqrt{-\frac{2\epsilon}{\gamma}}. \tag{3.40}$$

When $R < \sqrt{-2\epsilon/\gamma}$, we always have $\mathrm{d}^2S^{(\mathrm{sph})}/\mathrm{d}k^2 < 0$ even if $\gamma < 0$, and $S^{(\mathrm{sph})}(k)$ always monotonically decreases, which means that the spherical size is too small to accommodate phase fluctuations in a microemulsion. Therefore we define $R_{\min} = \sqrt{-2\epsilon/\gamma}$ as the minimum radius of such a spherical surface to possibly behave as a microemulsion. When $\gamma < 0$ and $R > R_{\min}$, we have $\mathrm{d}^2S^{(\mathrm{sph})}/\mathrm{d}k^2 > 0$, suggesting that $S^{(\mathrm{sph})}(k)$ has a single-peak pattern and that the system is a microemulsion. The radius threshold $R_{\min}$ is identical to the one (Equation (2.50)) derived from spherical harmonic modes $w_{l,m}$ in Section 2.4. An illustration of the existence of such a minimum size is shown in Figure 3.1, where the scattering signal

of $S^{(\mathrm{sph})}(k)$ for $R = \sqrt{2}$ is monotonically decreasing, suggesting a homogeneous state even when $\gamma < 0$, because $R = R_{\min}$ here.

Analytical calculation has given the location of the maximum for $S^{(\mathrm{2d})}(q)$ when $\gamma < 0$, which is $q = \sqrt{-\gamma/(2\epsilon)}$. It appears that the location of the maximum for $S^{(\mathrm{sph})}(k)$ when $\gamma < 0$ varies with radius, and numerical analysis shows that the location of the peak at a large radius $R \to \infty$ (e.g. $R = 100$) is

$$k \approx 0.78516\sqrt{-\frac{\gamma}{\epsilon}}. \tag{3.41}$$

The 2D and 3D structure factors cannot be directly compared in a quantitative way, since $\boldsymbol{q}$ and $\boldsymbol{k}$ are in different dimensionalities. We can do the quantitative comparison indirectly, through a model-free forward and inverse transformation between $S^{(\mathrm{2d})}(q)$ and $S^{(\mathrm{sph})}(k)$ of the same two-dimensional material in planar and spherical geometries. We develop the transformation by considering embedding a large plane in a three-dimensional space, where the in-plane wave vector $\boldsymbol{q}$ is a component of the 3D wave vector $\boldsymbol{k}$. We compare the orientational average of the 2D structure factor with the 3D structure factor of a large sphere whose surface is nearly flat. We also develop the inverse transform from a 3D structure factor into a 2D space. The transformation turns out to be exact for infinitely large planar and spherical surfaces, and is approximate for surfaces whose finite size is not too small.

## *3.2 Mathematical relationship and transformation between two- and three-dimensional structure factors*

For a planar surface made of any two-dimensional material whose 2D structure factor is defined as $S^{(\mathrm{2d})}(q)$ in Equation (3.3), the embedding of its order parameter $\phi(\boldsymbol{s}) = \phi(x, y)$ in a three-dimensional Euclidean space and Cartesian coordinate system is described by

$$\rho(\boldsymbol{r}) = \rho(x, y, z) = \phi(x, y)\delta(z) \tag{3.42}$$

so that the surface is in the x-y plane. The three-dimensional Fourier transform is

$$\tilde{\rho}(\boldsymbol{k}) = \int \mathrm{d}\boldsymbol{r}\, \rho(\boldsymbol{r}) e^{-i\boldsymbol{k}\cdot\boldsymbol{r}} = \int \mathrm{d}x\mathrm{d}y\, \phi(x, y) e^{-i\boldsymbol{k}_{\parallel}\cdot\boldsymbol{s}} = \tilde{\phi}(\boldsymbol{k}_{\parallel}) \tag{3.43}$$

where $\boldsymbol{k}_{\parallel}$ is the component of $k$ in the x-y plane. The structure factor of the embedding is

$$S^{(\mathrm{emb})}(\boldsymbol{k}) = \frac{1}{L^2}\left\langle|\tilde{\rho}(\boldsymbol{k})|\right\rangle = \frac{1}{L^2}\left\langle|\tilde{\phi}(\boldsymbol{k}_{\parallel})|^2\right\rangle = S^{(\mathrm{2d})}(\boldsymbol{k}_{\parallel}) \tag{3.44}$$

which means the structure factor of the embedding of a plane in a three-dimensional wave vector field $\boldsymbol{k}$ is equal to the 2D structure factor of the plane which is sensitive to the in-plane component of $\boldsymbol{k}$. Assuming the material is isotropic in the plane and that $S^{(\mathrm{emb})}(\boldsymbol{k})$ has a cylindrical symmetry according to its perpendicular direction, we calculate the spherical average of $S^{(\mathrm{emb})}(\boldsymbol{k})$ over polar angle $\theta$ and azimuthal angle $\varphi$. Using the relations

$$q = |\boldsymbol{k}_{\parallel}| = k\sin\theta \tag{3.45}$$

$$\theta = \arcsin\frac{q}{k} \tag{3.46}$$

we have

$$\begin{aligned} S^{(\mathrm{3d})}_{\mathrm{avg}}(k) &= \frac{1}{4\pi}\int_0^{\pi}\sin\theta\mathrm{d}\theta\int_0^{2\pi}\mathrm{d}\varphi\, S^{(\mathrm{emb})}(\boldsymbol{k}) = \frac{1}{2}\int_0^{\pi}\sin\theta\mathrm{d}\theta\, S^{(\mathrm{2d})}(q) \\ &= \frac{1}{2}\int_0^{\pi}\mathrm{d}\left(\arcsin\frac{q}{k}\right)\frac{q}{k}S^{(\mathrm{2d})}(q) = \int_0^{k}\mathrm{d}q\,\frac{1/k}{\sqrt{1-q^2/k^2}}\frac{q}{k}S^{(\mathrm{2d})}(q) \end{aligned} \tag{3.47}$$

which results in

$$S^{(\mathrm{3d})}_{\mathrm{avg}}(k) = \frac{1}{k}\int_0^{k}\mathrm{d}q\,\frac{q}{\sqrt{k^2-q^2}}S^{(\mathrm{2d})}(q). \tag{3.48}$$

Considering the plane placed in a three-dimensional field where the incoming wave vector $\boldsymbol{k}$ can make any angle $0 \leqslant \theta \leqslant \pi$ with the plane, we can interpret the orientational average $S^{(\mathrm{3d})}_{\mathrm{avg}}(k)$ as the average effect of rotating the plane over all orientations relative to $\boldsymbol{k}$. We can also consider an infinitely large sphere embedded in the same 3D space. Any small area on the surface of such a sphere is effectively flat, and can be in any orientation. Then the spherical surface as a whole is regarded as a collection of planes of all possible orientations. For this reason we have $S^{(\mathrm{3d})}_{\mathrm{avg}}(k) = S^{(\mathrm{sph})}(k)$ which is exact when the spherical size is infinitely large, and is approximate when the spherical radius $R \gg 1/k$ which is a characteristic length scaled by $k$. Combining these conclusions we have

$$S^{(\mathrm{sph})}(k) \to S^{(\mathrm{3d})}_{\mathrm{avg}}(k) \tag{3.49}$$

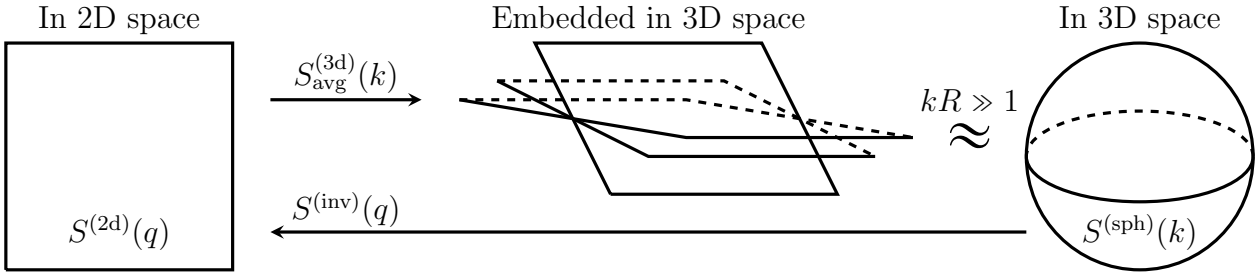


Figure 3.2: Mathematical relations and transformation between two- and three-dimensional structure factors (Equations (3.8) and (3.34)). At a large spherical size $R \gg 1/k$, we have $S^{(\mathrm{sph})}(k) \approx S^{(3\mathrm{d})}_{\mathrm{avg}}(k)$ and $S^{(\mathrm{inv})}(q) \approx S^{(2\mathrm{d})}(q)$.

when

$$kR \to \infty. \tag{3.50}$$

Following the same reasoning, we calculate the inverse transformation of Equation (3.48) to convert $S^{(3\mathrm{d})}_{\mathrm{avg}}(k)$ back to $S^{(2\mathrm{d})}(q)$. Because at a large radius $S^{(3\mathrm{d})}_{\mathrm{avg}}(k) \approx S^{(\mathrm{sph})}(k)$, we can apply the same inverse transformation on $S^{(\mathrm{sph})}(k)$ to convert it to a new structure factor $S^{(\mathrm{inv})}(q)$ which should satisfy

$$S^{(\mathrm{inv})}(q) \approx S^{(2\mathrm{d})}(q) \tag{3.51}$$

when $R \gg 1/k$. All these relationships between $S^{(2\mathrm{d})}(q)$, $S^{(\mathrm{sph})}(k)$, $S^{(3\mathrm{d})}_{\mathrm{avg}}(k)$ and $S^{(\mathrm{inv})}(q)$ are summarized in Figure 3.2 (adapted from Reference [109]). The development of this transformation is demanded by the need of a direct, quantitative comparison between the two-dimensional simulation result of a flat membrane (2D structure factor) and the three-dimensional scattering result of a vesicle (3D structure factor).

We obtain the expression of $S^{(\mathrm{inv})}(q)$ by deriving $S^{(2\mathrm{d})}(q)$ from $S^{(3\mathrm{d})}_{\mathrm{avg}}(k)$. From Equation (3.48) we use integration by parts on the right hand side to find

$$\begin{aligned} kS^{(3\mathrm{d})}_{\mathrm{avg}}(k) &= \left(-\sqrt{k^2-q^2}S^{(2\mathrm{d})}(q)\right)\Big|_{q=0}^{q=k} - \int_0^k \mathrm{d}q \left(-\sqrt{k^2-q^2}\frac{\mathrm{d}S^{(2\mathrm{d})}(q)}{\mathrm{d}q}\right) \\ &= kS^{(2\mathrm{d})}(0) + \int_0^k \mathrm{d}q\,\sqrt{k^2-q^2}\frac{\mathrm{d}S^{(2\mathrm{d})}(q)}{\mathrm{d}q} \end{aligned} \tag{3.52}$$

and then

$$\begin{aligned}\frac{\mathrm{d}}{\mathrm{d}k}\left(kS^{(3\mathrm{d})}_{\mathrm{avg}}(k)\right) &= S^{(2\mathrm{d})}(0) + \int_0^k \mathrm{d}q\, \frac{\partial}{\partial k}\left(\sqrt{k^2-q^2}\right)\frac{\mathrm{d}S^{(2\mathrm{d})}(q)}{\mathrm{d}q} \\ &= S^{(2\mathrm{d})}(0) + \int_0^k \mathrm{d}q\, \frac{k}{\sqrt{k^2-q^2}}\frac{\mathrm{d}S^{(2\mathrm{d})}(q)}{\mathrm{d}q}.\end{aligned} \tag{3.53}$$

Multiplying both sides by $1/\sqrt{p^2-k^2}$ where $p > k$ and integrating over $0 < k < p$ we have

$$\begin{aligned}&\int_0^p \mathrm{d}k\, \frac{\mathrm{d}}{\mathrm{d}k}\left(kS^{(3\mathrm{d})}_{\mathrm{avg}}(k)\right)\frac{1}{\sqrt{p^2-k^2}} \\ &= S^{(2\mathrm{d})}(0)\int_0^p \mathrm{d}k\, \frac{1}{\sqrt{p^2-k^2}} + \int_0^p \mathrm{d}k\, \frac{1}{\sqrt{p^2-k^2}}\int_0^k \mathrm{d}q\, \frac{k}{\sqrt{k^2-q^2}}\frac{\mathrm{d}S^{(2\mathrm{d})}(q)}{\mathrm{d}q} \\ &= \frac{\pi}{2}S^{(2\mathrm{d})}(0) + \int_0^p \mathrm{d}q\, \frac{\mathrm{d}S^{(2\mathrm{d})}(q)}{\mathrm{d}q}\int_q^p \mathrm{d}k\, \frac{k}{\sqrt{(p^2-k^2)(k^2-q^2)}} \\ &= \frac{\pi}{2}S^{(2\mathrm{d})}(0) + \frac{\pi}{2}\int_0^p \mathrm{d}q\, \frac{\mathrm{d}S^{(2\mathrm{d})}(q)}{\mathrm{d}q} = \frac{\pi}{2}S^{(2\mathrm{d})}(p).\end{aligned} \tag{3.54}$$

Replacing $p$ with $q$, we have

$$S^{(2\mathrm{d})}(q) = \frac{2}{\pi}\int_0^q \mathrm{d}k\, \frac{\mathrm{d}}{\mathrm{d}k}\left(kS^{(3\mathrm{d})}_{\mathrm{avg}}(k)\right)\frac{1}{\sqrt{q^2-k^2}}. \tag{3.55}$$

Here a three-dimensional wave vector $k$ corresponds to larger two-dimensional wave vectors $q > k$, not to its projection in a plane.

An alternative method to derive Equation (3.55) is to use the convolution theorem of Fourier transforms[108]. We start from Equation (3.48), in which we define variables

$$K = k^2 \tag{3.56}$$

$$Q = q^2 \tag{3.57}$$

and functions

$$T(K) = kS^{(3\mathrm{d})}_{\mathrm{avg}}(k) \tag{3.58}$$

$$D(Q) = S^{(2\mathrm{d})}(q) \tag{3.59}$$

$$W(\xi) = \begin{cases} 1/(2\sqrt{\xi}), & \xi > 0 \\ 0, & \xi \leqslant 0 \end{cases} \tag{3.60}$$

and rewrite Equation (3.48) into a convolution of $W(\xi)$ and $D(Q)$

$$T(K) = \frac{1}{2}\int_0^K \mathrm{d}Q\, \frac{D(Q)}{\sqrt{K-Q}} = W * D. \tag{3.61}$$

Using the convolution theorem and the Fourier transforms $\overline{T}(\tau)$, $\overline{D}(\tau)$ and $\overline{W}(\tau) = 1/(2\sqrt{2i\tau})$ of $T(K)$, $D(Q)$ and $W(\xi)$ respectively, we have

$$\overline{T}(\tau) = \overline{W}(\tau) \times \overline{D}(\tau) = \frac{\overline{D}(\tau)}{2\sqrt{2i\tau}} \tag{3.62}$$

which is

$$\overline{D}(\tau) = 2\sqrt{2i\tau} \times \overline{T}(\tau) = \frac{2}{\pi\sqrt{2i\tau}} \times 2\pi i\tau\overline{T}(\tau) = \frac{4}{\pi}\overline{W}(\tau) \times \overline{T'}(\tau) \tag{3.63}$$

where $\overline{T'}(\tau) = 2\pi i\tau\overline{T}(\tau)$ is the Fourier transform of $T' = \mathrm{d}T/\mathrm{d}K$. The inverse Fourier transform of Equation (3.63) gives

$$D = \frac{4}{\pi}W * T' = \frac{4}{\pi}\int_0^Q \mathrm{d}K\, W(Q-K)\frac{\mathrm{d}T}{\mathrm{d}K} \tag{3.64}$$

which is equivalent to

$$S^{(2\mathrm{d})}(q) = \frac{2}{\pi}\int_0^q \mathrm{d}k\, \frac{1}{\sqrt{q^2-k^2}}\frac{\mathrm{d}}{\mathrm{d}k}\left(kS^{(3\mathrm{d})}_{\mathrm{avg}}(k)\right) \tag{3.65}$$

which is identical to Equation (3.55).

The inverse transformation is thus

$$S^{(\mathrm{inv})}(q) = \frac{2}{\pi}\int_0^q \mathrm{d}k\, \frac{\mathrm{d}}{\mathrm{d}k}\left(kS^{(\mathrm{sph})}(k)\right)\frac{1}{\sqrt{q^2-k^2}}. \tag{3.66}$$

The integrand would diverge as $k \to q$. To avoid this difficulty in numerical calculation of the inverse transform, we can use partial integration to obtain the following expression

$$\begin{aligned} S^{(\mathrm{inv})}(q) &= \frac{2}{\pi}\left(\frac{\mathrm{d}}{\mathrm{d}k}(kS^{(\mathrm{sph})}(k))\arctan(\frac{k}{\sqrt{q^2-k^2}})\right)\Bigg|_{k=0}^{k=q} \\ &\quad - \frac{2}{\pi}\int_0^q \mathrm{d}k\, \arctan\left(\frac{k}{\sqrt{q^2-k^2}}\right)\frac{\mathrm{d}^2}{\mathrm{d}k^2}\left(kS^{(\mathrm{sph})}(k)\right) \\ &= \frac{\mathrm{d}}{\mathrm{d}k}\left(kS^{(\mathrm{sph})}(k)\right)\Big|_{k=q} - \frac{2}{\pi}\int_0^q \mathrm{d}k\, \arctan\left(\frac{k}{\sqrt{q^2-k^2}}\right)\frac{\mathrm{d}^2}{\mathrm{d}k^2}\left(kS^{(\mathrm{sph})}(k)\right). \end{aligned} \tag{3.67}$$

The orientational average (Equation (3.48)) and inverse transform (Equation (3.66)) are both independent of specific surface model, as long as both planar and spherical surfaces are made of the same two-dimensional material which has an in-plane isotropy. We can use the Gaussian model and its two- and three dimensional structure factors (Equations (3.8) and (3.34) respectively) to examine its applicability and limit.

### *3.3 Test and discussion of two/three-dimensional structure factor comparison and transformation*

Figure 3.3 shows the comparison of structure factors of the Gaussian model: two-dimensional structure factor $S^{(2d)}(q)$ (Equation (3.8)) of a large planar surface made of Gaussian material, three-dimensional structure factor $S^{(sph)}(k)$ (Equation (3.34)) of spherical surface made of the same material in various sizes (radius $R = 10$, 3, or $R_{min} = \sqrt{2}$ as calculated from Equation (3.40)), the forward transform or spherical average $S^{(3d)}_{avg}(k)$ (Equation (3.48)) of the 2D structure factor, and the inverse transform $S^{(inv)}(q)$ (Equation (3.66)) from the 3D structure factor. All calculations are done in Mathematica and Equation (3.67) is used for finding $S^{(inv)}(q)$. The summation in Equation (3.34) is processed over $l = 0$ to $l_{max} = 100$. And we use the same phenomenological parameters $k_B T = \alpha = \epsilon = 1$ and $\gamma = \pm 1$ as in Figure 3.1, which means the plots of $S^{(2d)}(q)$ and $S^{(sph)}(k)$ are the same ones as in Figure 3.1. For the same parameters $\gamma$ and $R$, $S^{(2d)}(q)$ and $S^{(sph)}(k)$ are placed in the same plot for direct comparison and the abscissa is wave vector in general. It is obvious that the structure factors of different dimensionalities are similar in shape, but not identical even at a large spherical size. The 2D structure factor is the same in subplots (b)–(d) of the same $\gamma = -1$, and so is $S^{(3d)}_{avg}(k)$.

When $\gamma > 0$ and both planar and spherical systems are homogeneous fluid, the forward and inverse transformation accurately computes $S^{(3d)}_{avg}(k) \approx S^{(sph)}(k)$ and $S^{(inv)}(q) \approx S^{(2d)}(q)$ which are almost exact, at least for a large radius $R = 10$. We anticipate that as the spherical size decreases, the approximations would not be exact and would finally collapse at a small enough size. We explore the situation of $\gamma < 0$ for this finite size effect, when

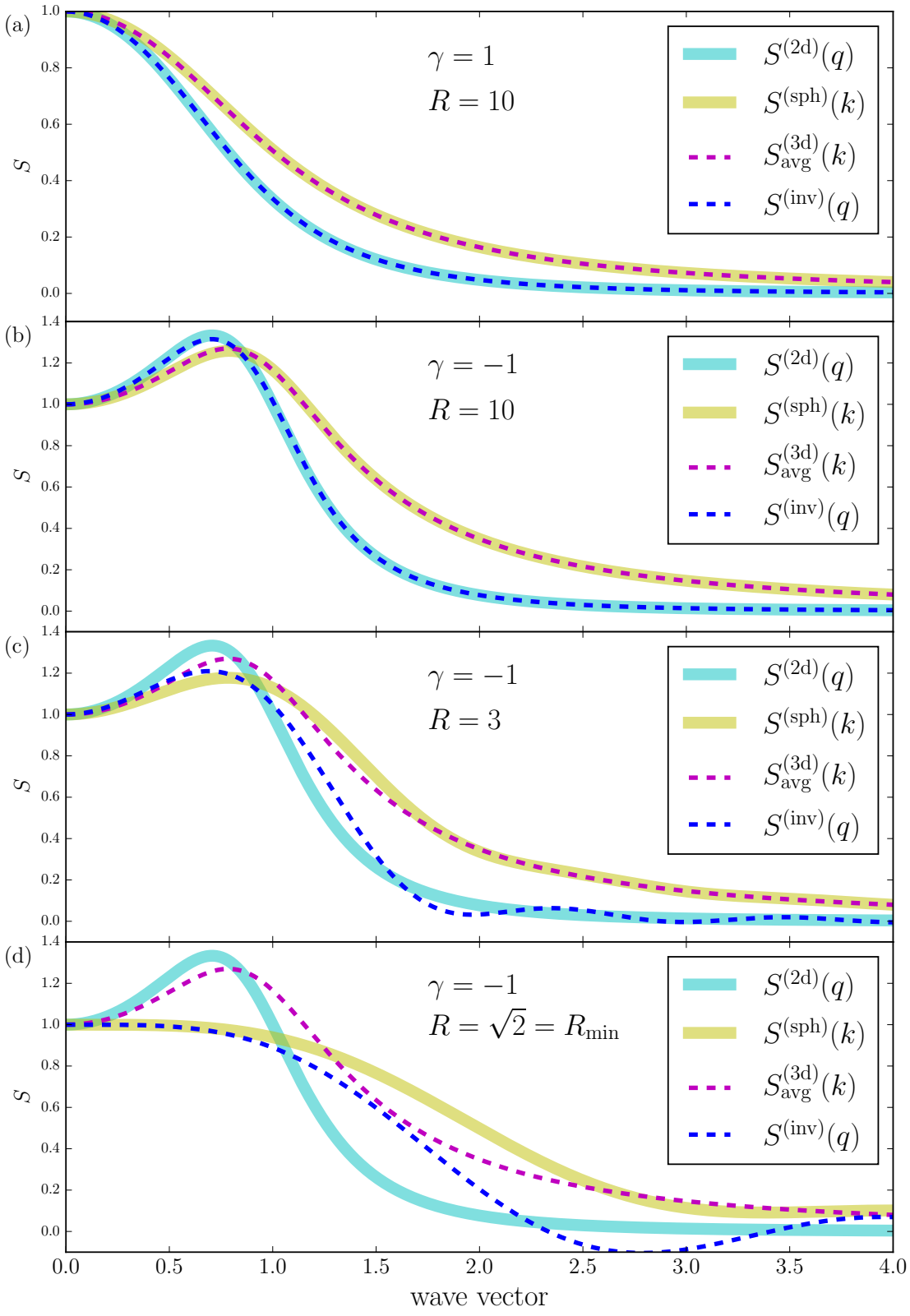


Figure 3.3: Comparison and transformation between two- and three-dimensional structure factors of the Gaussian model, $S^{(2d)}(q)$ and $S^{(sph)}(k)$. At a large spherical radius, the forward and inverse transformation (into $S^{(3d)}_{avg}(k)$ and $S^{(inv)}(q)$) is almost exact. The accuracy of the transformation decreases as the radius becomes smaller, and is totally ineffective when $R$ is as small as $R_{min}$. The abscissa is either $q$ or $k$ depending on the dimensionality.

$S^{(2d)}(q)$ indicates a microemulsion in the planar surface. When $R > R_{min} = \sqrt{2}$, $S^{(sph)}(k)$ also indicates a microemulsion in the spherical surface, and the transformation is accurate in computing $S^{(3d)}_{avg}(k) \approx S^{(sph)}(k)$ and $S^{(inv)}(q) \approx S^{(2d)}(q)$ almost exactly for a large $R = 10$. However, for $R = 3$, the transformation is not as effective in recovering $S^{(sph)}(k)$ from $S^{(2d)}(q)$ because the former obviously deviates from $S^{(3d)}_{avg}(k)$. And $S^{(inv)}(q)$ computed shows a non-monotonic (bumpy) pattern which cannot recover $S^{(2d)}(q)$ from $S^{(sph)}(k)$. When $R = R_{min}$, the spherical surface is actually homogeneous, and the $S^{(sph)}(k)$, which is qualitatively distinct from the single-peak $S^{(3d)}_{avg}(k)$, results in a bumpy $S^{(2d)}(q)$ whose value is negative at some $q$ and is thus not physical. This is an indication of the collapse of the transformation.

### *3.3.1 Discussion of the Gaussian model*

Both benefits and limitations of the mathematical relationship and transformation of the structure factors between spherical and planar systems are showcased. The transformation is nearly exact when the spherical radius is large compared to the intrinsic length scale of the material. At intermediate radius, the transformation still qualitatively captures some tendency of structure factor change in converting $S^{(2d)}(q)$ into $S^{(3d)}_{avg}(k)$, and $S^{(sph)}(k)$ into $S^{(inv)}(q)$, for example in a microemulsion the location of the signal peak is more to the left (smaller wave vector) in both $S^{(2d)}(q)$ and $S^{(inv)}(q)$ than that in $S^{(sph)}(k)$. When the spherical size is too small to accommodate a microemulsion, the transformation ceases to yield meaningful results in estimating planar from spherical structure factors or vice versa. We notice that the threshold radius $R_{min} = 1/k^*$ in which $k^*$ is defined on a plane, which leads to an intuitive interpretation: the length of the sphere's great circle, $2\pi R$, must exceed the correlation length $2\pi/k^*$ of the two-dimensional material to show microemulsion.

There are also several other limitations worth considering in any attempt of using the mathematical relationship and transformation. They arise from the simplicity of the Gaussian model used in this work. For a realistic material of non-zero thickness, the simplification into a two-dimensional material has to ignore the transverse scattering signal perpendicular to the surface. This effect is important for very small spheres when the thickness is siz-

able compared to the radius. The assumption of rigid planar and spherical surfaces of ideal geometries is another limitation. Shape deformations will have to be considered for a soft surface, and such a system of curvature-composition coupling is introduced in Chapter 4.

### *3.3.2 Test of the transformation using a single-domain model*

We can also test the transformation (Equations (3.48) and (3.66)) in a system whose structure factors are not described by the Gaussian model (Equations (3.8) and (3.34)). We consider a planar surface which is a square, at the center of which is a circular domain with an order parameter $\phi = 1$ which is different from the order parameter $\phi = 0$ of the area outside the domain. In a two-dimensional space and a polar coordinate system, we define

$$\phi(\boldsymbol{s}) = \phi(s,\theta) = \begin{cases} 1, & 0 \leqslant s \leqslant t \\ 0, & s > t \end{cases} \tag{3.68}$$

where $t$ is the radius of the round domain and $t < L/2$ where $L$ is the edge length of the square. Then the area fraction of the domain is

$$\chi = \frac{\pi t^2}{L^2}. \tag{3.69}$$

We calculate the two-dimensional Fourier transform of $\phi$ and structure factor of such a plane as follows ($J_1$ is the first-order Bessel function)

$$\tilde{\phi}(\boldsymbol{q}) = \int \mathrm{d}\boldsymbol{s}\, \phi e^{-i\boldsymbol{q}\cdot\boldsymbol{s}} = \int_0^t s\mathrm{d}s \int_0^{2\pi} \mathrm{d}\theta\, e^{-iqs\cos\theta} = 2\pi t \frac{J_1(qt)}{q} \tag{3.70}$$

$$S^{(2\mathrm{d})}(q) = \frac{1}{L^2}\left\langle \tilde{\phi}(\boldsymbol{q})\tilde{\phi}(\boldsymbol{q})^* \right\rangle = \frac{4\pi^2 t^2 J_1(qt)^2}{L^2 q^2}. \tag{3.71}$$

Now considering changing the topology of this plane by rolling it up into a spherical surface of the same surface area, with radius $R$ satisfying

$$4\pi R^2 = L^2 = A \tag{3.72}$$

where $A$ is the surface area in general. Then the circular domain becomes a dome on the spherical surface, which is defined by

$$\phi(\theta,\varphi) = \begin{cases} 1, & 0 \leqslant \theta \leqslant \alpha \\ 0, & \alpha < \theta \leqslant \pi \end{cases}. \tag{3.73}$$

The area fraction of the domain stays the same as in Equation (3.69) which is

$$\chi = \frac{1}{4\pi}\int_0^{2\pi} \mathrm{d}\varphi \int_0^{\alpha} \sin\theta \mathrm{d}\theta = \frac{1-\cos\alpha}{2} \tag{3.74}$$

and so

$$\cos\alpha = 1 - 2\chi. \tag{3.75}$$

We calculate the three-dimensional Fourier transform of the order parameter

$$\rho(\boldsymbol{r}) = \rho(r,\theta,\varphi) = \phi(\theta,\varphi)\delta(r-R) \tag{3.76}$$

and structure factor of such a sphere of a single domain as follows ($\boldsymbol{k} = (k, \theta_k, \varphi_k)$)

$$\tilde{\rho}(\boldsymbol{k}) = 4\pi R^2 \int_0^{2\pi} \mathrm{d}\varphi \int_0^{\alpha} \sin\theta \mathrm{d}\theta \sum_{l,m} (-i)^l j_l(kR) Y_{l,m}(\theta_k,\varphi_k) Y^*_{l,m}(\theta,\varphi) \tag{3.77}$$

$$\begin{aligned} S^{(\mathrm{sph})}(k) &= \frac{1}{4\pi R^2}\left(\frac{1}{4\pi}\int_0^{2\pi}\mathrm{d}\varphi_k \int_0^{\pi} \sin\theta_k \mathrm{d}\theta_k \, \tilde{\rho}(\boldsymbol{k})\tilde{\rho}^*(\boldsymbol{k})\right) \\ &= R^2 \sum_{l,m} j_l(kR)^2 \left| \int_0^{2\pi}\mathrm{d}\varphi \int_0^{\alpha} \sin\theta \mathrm{d}\theta \, Y_{l,m}(\theta,\varphi)\right|^2 \\ &= \pi R^2 \left\{ \frac{\sin^2(kR)}{(kR)^2}(1-\cos\alpha)^2 + \sum_{l>0}(2l+1) j_l(kR)^2 \frac{[(\cos\alpha)P_l(\cos\alpha) - P_{l+1}(\cos\alpha)]^2}{l^2}\right\} \end{aligned} \tag{3.78}$$

where $P_l$ is the Legendre polynomial.

Using Equations (3.69) and (3.72) and defining a new independent variable $x = qR = qL/\sqrt{4\pi}$, we rewrite Equation (3.71) into

$$\frac{S^{(\mathrm{2d})}(x)}{L^2} = \frac{\chi J_1(2x\sqrt{\chi})^2}{x^2}. \tag{3.79}$$

Equation (3.78) is similarly rewritten into (considering Equation (3.75) and $x = kR$ in the three-dimensional case)

$$\frac{S^{(\mathrm{sph})}(x)}{4\pi R^2} = \chi^2 \frac{\sin^2 x}{x^2} + \frac{1}{4}\sum_{l>0}(2l+1) j_l(x)^2 \frac{((1-2\chi)P_l(1-2\chi) - P_{l+1}(1-2\chi))^2}{l^2}. \tag{3.80}$$

We use Equation (3.48) to transform $S^{(\mathrm{2d})}(x)/L^2$ into $S^{(\mathrm{3d})}_{\mathrm{avg}}(x)/A$ which can be compared with $S^{(\mathrm{sph})}(x)/(4\pi R^2)$, and use Equation (3.66) to convert $S^{(\mathrm{sph})}(x)/(4\pi R^2)$ into $S^{(\mathrm{inv})}(x)/A$

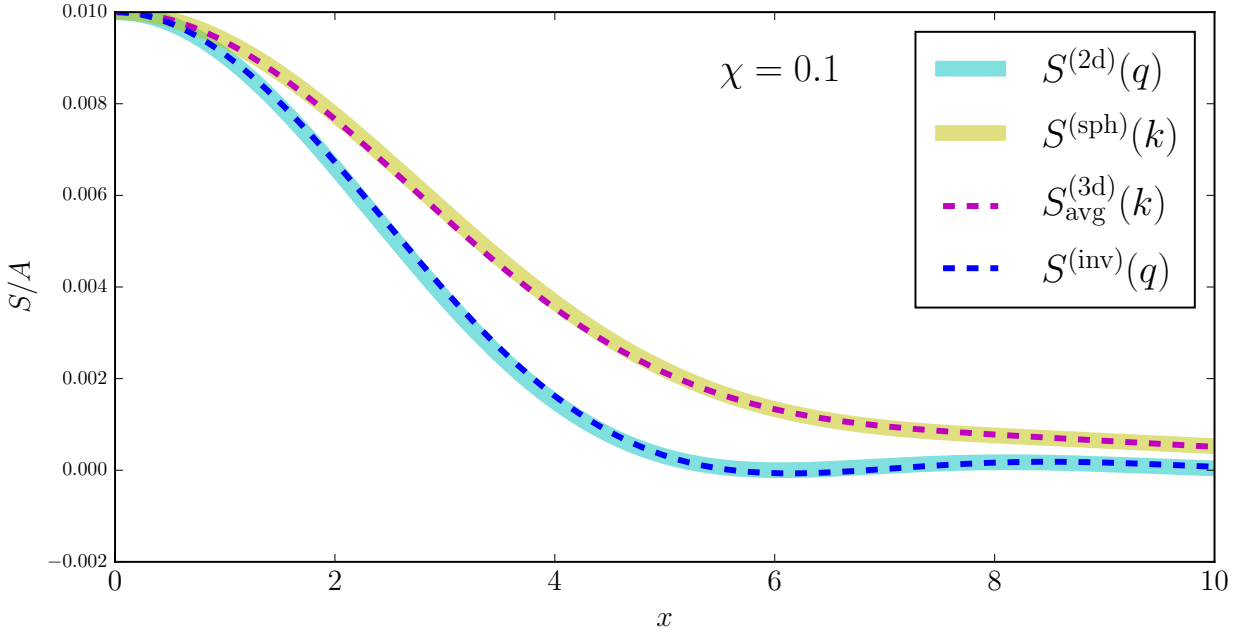


Figure 3.4: Comparison and transformation between two- and three-dimensional structure factors of the single-domain model, $S^{(2d)}(x)/L^2$ and $S^{(sph)}(x)/(4\pi R^2)$. Here the abscissa $x = qR$ for 2D structure factors and $x = kR$ for the 3D ones. Area fraction of the single domain $\chi = 0.1$. The forward and inverse transformation (into $S^{(3d)}_{avg}(x)/A$ and $S^{(inv)}(x)/A$) is almost exact. This comparison is insensitive to the system size.

which should be comparable to $S^{(2d)}(x)/L^2$. The results for domain area fraction $\chi = 0.1$ is shown in Figure 3.4. The structure factors could be very close to 0 but never become negative. Because the size effect of the system is reduced in this analysis, the comparisons are exact to a great extent, with $S^{(inv)}$ able to capture the bumpy feature of $S^{(2d)}$. We have tested that the approximate transformation is still valid even when $\chi = 0.5$ when the system shows a phase separation into two domains of the same area. Both the Gaussian model and the single-domain model validate the effectiveness of the approximate transformation in the range of this theoretical study.

# Chapter 4

# LIPID VESICLES WITH COMPOSITION-CURVATURE COUPLING AND THEIR PHASE DIAGRAMS

In this chapter we introduce a lipid membrane model that is able to describe shape deformations induced by the coupling between surface composition and local geometry of the membrane, which is regarded as two-dimensional fluid. The coupling is believed to play a crucial role in separating lipid species into domains of different bending rigidities and/or spontaneous curvatures. In order to incorporate this effect into the Landau-Ginzburg model, which would increase its usefulness in describing realistic systems handled in experiments, we combine a Helfrich model of membrane bending energetics with the standard Landau-Ginzburg free energy expression. Both bending rigidity and spontaneous curvature are linear functions of the surface compositional field. An optional Gaussian bending term may also be added into the model. Under certain approximations, simplifications and conditions, we show ground state phase diagrams generated from this model which are calculated using different methods, and they all appear similar. These phase diagrams demonstrate that without an extended Landau-Ginzburg model and an effectively negative interface line tension, modulated phases can still be produced with a composition-curvature coupling, in agreement with some existing works in the literature. We show some surface patterns as examples extracted from points on the phase diagrams. We also calculate experimentally measurable physical properties from our model, and compare them with similar measurables determined in experiments or simulations.

## 4.1 Establishment and treatment of the coupling model on a vesicular surface

### *4.1.1 Helfrich bending energy and the model of composition-curvature coupling*

The mechanical bending model of Helfrich (or Canham–Helfrich, first introduced in References [83] and [118]), defined on a two-dimensional surface $S$, is

$$E = \int \mathrm{d}S \, \frac{\kappa}{2}(H - H_\mathrm{s})^2 \tag{4.1}$$

in which $\kappa$ is the bending modulus, $H$ is twice the mean curvature and $H_\mathrm{s}$ is twice spontaneous curvature of the membrane. If $\kappa_a$ and $\kappa_b$ are the principal curvatures at a local point on the surface, then

$$H = \kappa_a + \kappa_b \tag{4.2}$$

$$K = \kappa_a \kappa_b. \tag{4.3}$$

in which the second property $K$ is the Gaussian curvature. And the spontaneous curvature is the reciprocal of the spontaneous radius $R_\mathrm{s}$, which means

$$H_\mathrm{s} = \frac{2}{R_\mathrm{s}}. \tag{4.4}$$

For the sake of simplicity, we refer to $H$ and $H_\mathrm{s}$ as "mean curvature" and "spontaneous curvature" respectively.

On a surface whose local deformation is characterized by a height $h(\boldsymbol{r})$, a deviation relative to an undeformed reference surface, the mean curvature $H$ is a functional of $h(\boldsymbol{r})$ and also changes locally. In a non-homogeneous system such as a multicomponent lipid membrane, the bending modulus $\kappa$ and spontaneous curvature $H_\mathrm{s}$ would also change continuously on the surface. In our composition-curvature coupling model, we assume that both bending modulus $\kappa$ and spontaneous curvature $H_\mathrm{s}$ are linearly dependent on the surface compositional organization characterized by the order parameter $\phi(\boldsymbol{r})$, which means they are linear functionals of $\phi(\boldsymbol{r})$. This is reasoned by considering a lipid membrane which is able to phase separate into liquid-ordered and liquid-disordered domains. When phase separation happens, the liquid-ordered phase would obtain a different bending modulus and spontaneous

curvature than the liquid-disordered phase, where lipid molecules are more loosely packed. We assume

$$\kappa = \begin{cases} \kappa_{\rm lo}, & \text{liquid-ordered} \\ \kappa_{\rm ld}, & \text{liquid-disordered} \end{cases} \tag{4.5}$$

$$H_{\rm s} = \begin{cases} H_{\rm lo}, & \text{liquid-ordered} \\ H_{\rm ld}, & \text{liquid-disordered} \end{cases} . \tag{4.6}$$

We assume the local concentrations (mole fractions, or relative amounts) of the more ordered species and the more disordered species (e.g. DPPC and DOPC lipids) at point $\boldsymbol{r}$ to be $\phi_{\rm lo}(\boldsymbol{r})$ and $\phi_{\rm ld}(\boldsymbol{r})$ respectively, and we have

$$\phi_{\rm lo}(\boldsymbol{r}) + \phi_{\rm ld}(\boldsymbol{r}) = 1. \tag{4.7}$$

Then at any point on the surface, being in any lateral phase or surface pattern, the bending modulus $\kappa$ would be a linear combination of $\kappa_{\rm lo}$ and $\kappa_{\rm ld}$, and the spontaneous curvature is linearly combined by $H_{\rm lo}$ and $H_{\rm ld}$ through

$$\kappa = \kappa_{\rm lo}\phi_{\rm lo}(\boldsymbol{r}) + \kappa_{\rm ld}\phi_{\rm ld}(\boldsymbol{r}) \tag{4.8}$$

$$H_{\rm s} = H_{\rm lo}\phi_{\rm lo}(\boldsymbol{r}) + H_{\rm ld}\phi_{\rm ld}(\boldsymbol{r}). \tag{4.9}$$

One way to define the order parameter $\phi(\boldsymbol{r})$ is to calculate the difference between $\phi_{\rm lo}(\boldsymbol{r})$ and $\phi_{\rm ld}(\boldsymbol{r})$ [92]

$$\phi(\boldsymbol{r}) = \phi_{\rm lo}(\boldsymbol{r}) - \phi_{\rm ld}(\boldsymbol{r}). \tag{4.10}$$

Then from Equations (4.7) and (4.10) the bending modulus and spontaneous curvature are

$$\kappa[\phi(\boldsymbol{r})] = \frac{\kappa_{\rm lo} - \kappa_{\rm ld}}{2}\phi(\boldsymbol{r}) + \frac{\kappa_{\rm lo} + \kappa_{\rm ld}}{2} = \kappa_0 + \kappa_1\phi(\boldsymbol{r}) \tag{4.11}$$

$$H_{\rm s}[\phi(\boldsymbol{r})] = \frac{H_{\rm lo} - H_{\rm ld}}{2}\phi(\boldsymbol{r}) + \frac{H_{\rm lo} + H_{\rm ld}}{2} = H_0 + H_1\phi(\boldsymbol{r}) \tag{4.12}$$

in which $\kappa_0 = (\kappa_{\rm lo} - \kappa_{\rm ld})/2$, $\kappa_1 = (\kappa_{\rm lo} + \kappa_{\rm ld})/2$, $H_0 = (H_{\rm lo} - H_{\rm ld})/2$ and $H_1 = (H_{\rm lo} + H_{\rm ld})/2$ are constants.

The shape-composition coupling model, by combining Landau-Ginzburg and Helfrich free energies, is defined as

$$E = \int \mathrm{d}S \left\{ \frac{\alpha}{2} |\phi(\boldsymbol{r})|^2 + \frac{b}{4} |\phi(\boldsymbol{r})|^4 + \frac{\gamma}{2} |\nabla\phi(\boldsymbol{r})|^2 \right\} + \int \mathrm{d}S \, \frac{\kappa[\phi(\boldsymbol{r})]}{2} \Big\{ H - H_{\mathrm{s}}[\phi(\boldsymbol{r})] \Big\}^2 + \int \mathrm{d}S \, \bar{\kappa} K + \sigma \int \mathrm{d}S. \tag{4.13}$$

The first integral is the standard Landau-Ginzburg model, and the second integral is the Helfrich model with implicit couplings. The Laplacian squared term from the extended Landau-Ginzburg model is not needed because we are looking into the effect of a positive $\gamma$. The third integral is the Gaussian bending energy term, in which $\bar{\kappa}$ is the Gaussian bending modulus, and $\sigma$ is the surface tension. An additional term of chemical potential $\mu$ (which is related the the relative amounts of ordered and disordered species)

$$-\mu \int \mathrm{d}S \, \phi(\boldsymbol{r}) \tag{4.14}$$

can be added into the system to control the surface composition of lipid species. We assume there are equal amounts of ordered and disordered species, and we have $\phi = 0$ on average and so the term is equal to 0. We introduce this constraint explicitly later.

Many previous applications of the Helfrich model are on a deformable planar surface, where the undeformed plane is placed in the x-y plane of a Cartesian coordinate system, and its deformation is described by the local height $z = h(x, y)$ in the z-direction. Here we focus on the implementation of the coupling model on a soft, deformable spherical surface, which is closed and has the topology of a sphere. The local height on the spherical surface, which is a radial deviation from the undeformed radius $R_0$, is a function of polar angle $\theta$ and azimuthal angle $\varphi$ in a spherical coordinate system:

$$h(\theta, \varphi) = R(\theta, \varphi) - R_0. \tag{4.15}$$

The mean curvature $H$, then, is a functional of $h(\theta, \varphi)$ (see specific derivation of $H$ in terms of $h$ in Reference [62]), and the bending modulus $\kappa$ and spontaneous curvature $H_{\mathrm{s}}$ are dependent

on the local order parameter $\phi(\theta,\varphi)$. In this system the coupling model (Equation (4.13)) is

$$\begin{aligned} E = &\int \mathrm{d}S \left\{ \frac{\alpha}{2} \left|\phi(\theta,\varphi)\right|^2 + \frac{b}{4} \left|\phi(\theta,\varphi)\right|^4 + \frac{\gamma}{2} \left|\nabla\phi(\theta,\varphi)\right|^2 \right\} \\ &+ \int \mathrm{d}S \, \frac{\kappa[\phi(\theta,\varphi)]}{2} \Big\{ H - H_{\mathrm{s}}[\phi(\theta,\varphi)] \Big\}^2 + \int \mathrm{d}S \, \bar{\kappa} K + \sigma \int \mathrm{d}S + pV. \end{aligned} \tag{4.16}$$

Here the surface tension $\sigma$ and osmotic pressure $p$ are Lagrange multipliers of surface area $\int \mathrm{d}S$ and the volume $V$ enclosed by the vesicular surface, and they can be used to change the shape of the vesicle. In the third integral, the Gaussian bending term, if $\bar{\kappa}$ is a constant all over the surface, which is an assumption made by some theoretical works, then according to the Gauss-Bonnet theorem

$$\int \mathrm{d}S \, K = 4\pi \tag{4.17}$$

over the closed surface, and the Gaussian bending term would be a constant

$$\int \mathrm{d}S \, \bar{\kappa} K = 4\pi\bar{\kappa} \tag{4.18}$$

and can be dropped from Equation (4.16) because it plays no role in the optimization of the energy. In this case the model without Gaussian bending is

$$\begin{aligned} E = &\int \mathrm{d}S \left\{ \frac{\alpha}{2} \left|\phi(\theta,\varphi)\right|^2 + \frac{b}{4} \left|\phi(\theta,\varphi)\right|^4 + \frac{\gamma}{2} \left|\nabla\phi(\theta,\varphi)\right|^2 \right\} \\ &+ \int \mathrm{d}S \, \frac{\kappa[\phi(\theta,\varphi)]}{2} \Big\{ H - H_{\mathrm{s}}[\phi(\theta,\varphi)] \Big\}^2 + \sigma \int \mathrm{d}S + pV. \end{aligned} \tag{4.19}$$

But some theories[47, 119] indicate that the Gaussian bending modulus is not a constant and is approximately equal to negative bending modulus $\bar{\kappa} \approx -\kappa$, so in the model we can optionally choose

$$\bar{\kappa}[\phi(\boldsymbol{r})] = -\kappa[\phi(\boldsymbol{r})] = -\kappa_0 - \kappa_1\phi(\boldsymbol{r}) \tag{4.20}$$

and from Equation (4.16) we have the model with Gaussian bending as

$$\begin{aligned} E = &\int \mathrm{d}S \left\{ \frac{\alpha}{2} \left|\phi(\theta,\varphi)\right|^2 + \frac{b}{4} \left|\phi(\theta,\varphi)\right|^4 + \frac{\gamma}{2} \left|\nabla\phi(\theta,\varphi)\right|^2 \right\} \\ &+ \int \mathrm{d}S \, \frac{\kappa[\phi(\theta,\varphi)]}{2} \Big\{ H - H_{\mathrm{s}}[\phi(\theta,\varphi)] \Big\}^2 - \int \mathrm{d}S \, \kappa[\phi(\theta,\varphi)] K + \sigma \int \mathrm{d}S + pV. \end{aligned} \tag{4.21}$$

We analyze both treatments of Gaussian bending and draw phase diagrams of a vesicle with or without Gaussian bending. To this end, we apply spherical harmonic analysis as has been done for the extended Landau-Ginzburg model (Chapter 2). Beside decomposing $\phi(\theta, \varphi)$ into its spherical harmonic modes $w_{l,m}$ (Equation (2.20))

$$\phi(\theta, \varphi) = \sum_{l=0}^{\infty} \sum_{m=-l}^{l} w_{l,m} Y_{l,m}(\theta, \varphi) \tag{4.22}$$

we also need to decompose $h(\theta, \varphi)$ into spherical harmonic modes $u_{l,m}$ in a similar way,

$$h(\theta, \varphi) = \sum_{l=0}^{\infty} \sum_{m=-l}^{l} u_{l,m} Y_{l,m}(\theta, \varphi) \equiv \sum_{l,m} u_{l,m} Y_{l,m}(\theta, \varphi), \tag{4.23}$$

which also has

$$u^*_{l,m} = (-1)^m u_{l,-m} \tag{4.24}$$

because $h$ is real. Here, $l$ and $m$ are integers.

### *4.1.2 Spherical harmonic analysis and quadratic approximation*

Before applying spherical harmonic analysis to rewrite Equation (4.19) or Equation (4.21) in the spherical harmonic space, we briefly review some knowledge from differential geometry of a closed surface embedded in three-dimensional space[62]. In a spherical coordinate system, the three orthogonal unit vectors are defined as

$$\hat{\boldsymbol{r}} = \sin\theta\cos\varphi\hat{\boldsymbol{x}} + \sin\theta\sin\varphi\hat{\boldsymbol{y}} + \cos\theta\hat{\boldsymbol{z}} \tag{4.25}$$

$$\hat{\boldsymbol{\theta}} = \cos\theta\cos\varphi\hat{\boldsymbol{x}} + \cos\theta\sin\varphi\hat{\boldsymbol{y}} - \sin\theta\hat{\boldsymbol{z}} \tag{4.26}$$

$$\hat{\boldsymbol{\varphi}} = -\sin\varphi\hat{\boldsymbol{x}} + \cos\varphi\hat{\boldsymbol{y}} \tag{4.27}$$

and first derivatives of $\hat{\boldsymbol{r}}$ with respect to $\theta$ and $\varphi$ are

$$\frac{\partial\hat{\boldsymbol{r}}}{\partial\theta} = \hat{\boldsymbol{\theta}} \tag{4.28}$$

$$\frac{\partial\hat{\boldsymbol{r}}}{\partial\varphi} = \sin\theta\hat{\boldsymbol{\varphi}}. \tag{4.29}$$

For a closed surface described by $\boldsymbol{r} = r(\theta, \varphi)\hat{\boldsymbol{r}}$, we have

$$\boldsymbol{r}_\theta = \frac{\partial \boldsymbol{r}}{\partial \theta} = \frac{\partial r}{\partial \theta}\hat{\boldsymbol{r}} + r\hat{\boldsymbol{\theta}} = r_\theta \hat{\boldsymbol{r}} + r\hat{\boldsymbol{\theta}} \tag{4.30}$$

$$\boldsymbol{r}_\varphi = \frac{\partial \boldsymbol{r}}{\partial \varphi} = \frac{\partial r}{\partial \varphi}\hat{\boldsymbol{r}} + r\sin\theta\hat{\boldsymbol{\varphi}} = r_\varphi \hat{\boldsymbol{r}} + r\sin\theta\hat{\boldsymbol{\varphi}} \tag{4.31}$$

and so we have

$$|\boldsymbol{r}_\theta|^2 = r_\theta^2 + r^2 \tag{4.32}$$

$$|\boldsymbol{r}_\varphi|^2 = r_\varphi^2 + r^2\sin^2\theta \tag{4.33}$$

$$\boldsymbol{r}_\theta \cdot \boldsymbol{r}_\varphi = r_\theta r_\varphi \tag{4.34}$$

which may be combined to make the metric tensor $\boldsymbol{G}$

$$\boldsymbol{G} = \begin{pmatrix} r_\theta^2 + r^2 & r_\theta r_\varphi \\ r_\theta r_\varphi & r_\varphi^2 + r^2\sin^2\theta \end{pmatrix} \tag{4.35}$$

whose inverse matrix is

$$\boldsymbol{G}^{-1} = \frac{1}{g}\begin{pmatrix} r_\varphi^2 + r^2\sin^2\theta & -r_\theta r_\varphi \\ -r_\theta r_\varphi & r_\theta^2 + r^2 \end{pmatrix} \tag{4.36}$$

where the square of surface area element (the determinant of $\boldsymbol{G}$)

$$g = |\boldsymbol{G}| = r^2 r_\varphi^2 + r^4\sin^2\theta + r^2 r_\theta^2\sin^2\theta. \tag{4.37}$$

The inverse metric tensor is used to calculate the squared gradient of any function $\phi(\theta, \varphi)$ defined on the curved surface [55]

$$\begin{aligned} |\nabla\phi|^2 &= \boldsymbol{G}^{-1}(1,1)(\frac{\partial\phi}{\partial\theta})^2 + \boldsymbol{G}^{-1}(1,2)\frac{\partial\phi}{\partial\theta}\frac{\partial\phi}{\partial\varphi} + \boldsymbol{G}^{-1}(2,1)\frac{\partial\phi}{\partial\varphi}\frac{\partial\phi}{\partial\theta} + \boldsymbol{G}^{-1}(2,2)(\frac{\partial\phi}{\partial\varphi})^2 \\ &= \frac{r_\varphi^2 + r^2\sin^2\theta}{g}\phi_\theta^2 + \frac{r_\theta^2 + r^2}{g}\phi_\varphi^2 - \frac{2r_\theta r_\varphi}{g}\phi_\theta\phi_\varphi. \end{aligned} \tag{4.38}$$

According to our previous definition in Equation (4.15), $r(\theta, \varphi) = R(\theta, \varphi)$ and its first derivatives $r_\theta = h_\theta$ and $r_\varphi = h_\varphi$. The radial deviation $h(\theta, \varphi)$ and its derivatives are small compared to $R(\theta, \varphi)$ so that $R \approx R_0$. Similarly, the order parameter $\phi(\theta, \varphi)$ is also small and fluctuating around $\phi = 0$, and so are its derivatives. Any function of $h$, $h_\theta$, $h_\varphi$ and

second derivatives $h_{\theta\theta}$, $h_{\theta\varphi}$ and $h_{\varphi\varphi}$, and $\phi$, $\phi_\theta$ and $\phi_\varphi$ (and second derivatives of $\phi$), can be expanded into a Taylor series of these independent variables and their products. Under the quadratic approximation, we only keep terms up to the second order of these variables and multiplications. For example, we have

$$|\phi(\theta,\varphi)|^2 \,\mathrm{d}S = |\phi|^2 \sqrt{g}\mathrm{d}\theta\mathrm{d}\varphi \approx \phi^2 R_0^2 \sin\theta \mathrm{d}\theta\mathrm{d}\varphi \tag{4.39}$$

and (from Equation (4.38))

$$|\nabla\phi(\theta,\varphi)|^2\mathrm{d}S = |\nabla\phi|^2\sqrt{g}\mathrm{d}\theta\mathrm{d}\varphi \approx \left(\frac{\phi_\varphi^2}{\sin\theta} + \phi_\theta^2 \sin\theta\right)\mathrm{d}\theta\mathrm{d}\varphi = \left(\frac{\phi_\varphi^2}{\sin^2\theta} + \phi_\theta^2\right)\sin\theta\mathrm{d}\theta\mathrm{d}\varphi \tag{4.40}$$

which are simply the square and squared gradient terms on an undeformed spherical surface of a Landau-Ginzburg model. In the coupling model, we manipulate the quadratic part

$$\begin{aligned} E_2 = \int \mathrm{d}S \Big\{ &\frac{\alpha}{2}|\phi(\theta,\varphi)|^2 + \frac{\gamma}{2}|\nabla\phi(\theta,\varphi)|^2 + \frac{\kappa[\phi(\theta,\varphi)]}{2}\{H - H_\mathrm{s}[\phi(\theta,\varphi)]\}^2 \\ &+ \sigma + \Big(-\kappa[\phi(\theta,\varphi)]K\Big)\Big\} + pV \end{aligned} \tag{4.41}$$

with quadratic approximation, where the Gaussian bending

$$-\int \mathrm{d}S\, \kappa[\phi(\theta,\varphi)]K \tag{4.42}$$

is optional, while the quartic term

$$E_4 = \int \mathrm{d}S \frac{b}{4}|\phi(\theta,\varphi)|^4 \tag{4.43}$$

is preserved exactly and written as (see Equation (2.32))

$$E_4 = \frac{bR_0^2}{4}\sum_{l,m}\left|\sum_{l_1,m_1}\sum_{l_2,m_2}\sqrt{\frac{(2l_1+1)(2l_2+1)(2l+1)}{4\pi}}\begin{pmatrix} l_1 & l_2 & l \\ 0 & 0 & 0\end{pmatrix}\begin{pmatrix} l_1 & l_2 & l \\ m_1 & m_2 & m\end{pmatrix} w_{l_1,m_1} w_{l_2,m_2}\right|^2. \tag{4.44}$$

Thus the full model $E = E_2 + E_4$ is treated in a hybrid method.

We define the operator $\widetilde{\nabla}$ (which is also used in Reference [58])

$$\widetilde{\nabla} = R\nabla = \frac{\partial}{\partial\theta}\hat{\boldsymbol{\theta}} + \frac{1}{\sin\theta}\frac{\partial}{\partial\varphi}\hat{\boldsymbol{\varphi}} \tag{4.45}$$

which is independent of the radius. From the fact that

$$\widetilde{\nabla}^2 Y_{l,m}(\theta,\varphi) = -l(l+1)Y_{l,m}(\theta,\varphi) \tag{4.46}$$

and using the properties of spherical harmonics, we have

$$\int \mathrm{d}S\ |\phi(\theta,\varphi)|^2 \approx R_0^2 \sum_{l,m} |w_{l,m}|^2 \tag{4.47}$$

$$\int \mathrm{d}S\, |\nabla\phi(\theta,\varphi)|^2 \approx \int \mathrm{d}\Omega\, \left(\frac{\phi_\varphi^2}{\sin^2\theta} + \phi_\theta^2\right) = \int \mathrm{d}\Omega\, |\widetilde{\nabla}\phi|^2 = \sum_{l,m} l(l+1)|w_{l,m}|^2 \tag{4.48}$$

and so the quadratic Landau-Ginzburg terms in $E_2$ are

$$\int \mathrm{d}S\, \left\{\frac{\alpha}{2}\,|\phi|^2 + \frac{\gamma}{2}|\nabla\phi|^2\right\} = \sum_{l,m}\left[\frac{R_0^2\alpha}{2} + \frac{\gamma}{2}l(l+1)\right]|w_{l,m}|^2. \tag{4.49}$$

We find the following integrals of $h(\theta,\varphi)$ and its derivatives:

$$\int \mathrm{d}\Omega\, h = 2\sqrt{\pi}u_{0,0} \tag{4.50}$$

$$\int \mathrm{d}\Omega\, \widetilde{\nabla}^2 h = 0 \tag{4.51}$$

$$\int \mathrm{d}\Omega\ |h|^2 = \sum_{l,m} |u_{l,m}|^2 \tag{4.52}$$

$$\int \mathrm{d}\Omega\, |\widetilde{\nabla}h|^2 = \sum_{l,m} l(l+1)|u_{l,m}|^2 \tag{4.53}$$

$$\int \mathrm{d}\Omega\, |\widetilde{\nabla}^2 h|^2 = \sum_{l,m} [l(l+1)]^2 |u_{l,m}|^2. \tag{4.54}$$

We then have the following integrals that are useful in the spherical harmonic transform of $E_2$ (Equation (4.41)):

$$\int \mathrm{d}S\, \phi \approx \int \mathrm{d}\Omega\, (R_0^2 + 2R_0 h)\phi = 2\sqrt{\pi}R_0^2 w_{0,0} + 2R_0 \sum_{l,m} w_{l,m}^* u_{l,m} \tag{4.55}$$

$$\int \mathrm{d}S \approx \int \mathrm{d}\Omega\ \left(R_0^2 + 2R_0 h + h^2 + \frac{1}{2}|\widetilde{\nabla}h|^2\right) = 4\pi R_0^2 + 4\sqrt{\pi}u_{0,0}R_0 + \sum_{l,m}|u_{l,m}|^2\left[1 + \frac{l(l+1)}{2}\right] \tag{4.56}$$

$$\int \mathrm{d}S\, H \approx \int \mathrm{d}\Omega\, \left(\frac{1}{R_0}|\widetilde{\nabla} h|^2 + 2R_0 + 2h - \widetilde{\nabla}^2 h\right) = 8\pi R_0 + 4\sqrt{\pi} u_{0,0} + \sum_{l,m} \frac{|u_{l,m}|^2}{R_0} l(l+1) \quad (4.57)$$

$$\begin{aligned} \int \mathrm{d}S\, H^2 &\approx \int \mathrm{d}\Omega\, \left[\frac{4h}{R_0^2}\widetilde{\nabla}^2 h - \frac{4}{R_0}\widetilde{\nabla}^2 h + \frac{2}{R_0^2}|\widetilde{\nabla} h|^2 + \frac{1}{R_0^2}|\widetilde{\nabla}^2 h|^2 + 4\right] \\ &= 16\pi + \sum_{l,m} \frac{|u_{l,m}|^2}{R_0^2}(l-1)l(l+1)(l+2) \end{aligned} \quad (4.58)$$

$$V \approx \frac{R_0^3}{3}\int \mathrm{d}\Omega + R_0^2 \int h \mathrm{d}\Omega + R_0 \int h^2 \mathrm{d}\Omega = \frac{4\pi}{3} R_0^3 + 2\sqrt{\pi} u_{0,0} R_0^2 + R_0 \sum_{l,m} |u_{l,m}|^2 \quad (4.59)$$

$$\int \mathrm{d}S\, H\phi \approx \int \mathrm{d}\Omega\, (2h + 2R_0 - \widetilde{\nabla}^2 h)\phi = \sum_{l,m} [l(l+1) + 2] w_{l,m}^* u_{l,m} + 4\sqrt{\pi} R_0 w_{0,0} \quad (4.60)$$

The coupling in Equation (4.60), $\int \mathrm{d}S\, H\phi$, is a common explicit coupling used by previous theoretical studies (see Chapter 1). In our coupling model, we also need the coupling terms

$$\int \mathrm{d}S\, H^2\phi \approx 4\int \mathrm{d}\Omega\, \left(1 - \frac{1}{R_0}\widetilde{\nabla}^2 h\right)\phi = 8\sqrt{\pi} w_{0,0} + \frac{4}{R_0}\sum_{l,m} l(l+1) w_{l,m}^* u_{l,m} \quad (4.61)$$

$$\int \mathrm{d}S\, H\phi^2 \approx -2R_0 \int \mathrm{d}\Omega\, \phi^2 = -2R_0 \sum_{l,m} |w_{l,m}|^2. \quad (4.62)$$

The Helfrich bending term in $E_2$ is decomposed into

$$\begin{aligned} \int \mathrm{d}S\, \frac{\kappa[\phi]}{2}\Big\{H - H_{\mathrm{s}}[\phi]\Big\}^2 &= \int \mathrm{d}S\, \frac{\kappa_0 + \kappa_1\phi}{2}(H - H_0 - H_1\phi)^2 \\ &= \underbrace{\frac{\kappa_1}{2}\int \mathrm{d}S\, (H - H_0)^2\phi}_{\text{(I)}} + \underbrace{\frac{\kappa_0}{2}\int \mathrm{d}S\, (H - H_0)^2}_{\text{(II)}} + \underbrace{\frac{\kappa_1}{2}\int \mathrm{d}S\, H_1^2\phi^3}_{\text{(III)}} \\ &\quad + \underbrace{\frac{\kappa_0}{2}\int \mathrm{d}S\, H_1^2\phi^2}_{\text{(IV)}} \underbrace{-\kappa_1 \int \mathrm{d}S\, (H - H_0)H_1\phi^2}_{\text{(V)}} \underbrace{-\kappa_0 \int \mathrm{d}S\, (H - H_0)H_1\phi}_{\text{(VI)}}. \end{aligned} \quad (4.63)$$

Under the quadratic approximation, based on the above integrals, we have Terms (I)–(VI) transformed into

$$\text{(I)} = \sqrt{\pi}\kappa_1(2 - R_0H_0)^2 w_{0,0} + \frac{\kappa_1}{R_0}(2 - H_0R_0)\sum_{l,m}[l(l+1) - R_0H_0] w_{l,m}^* u_{l,m} \quad (4.64)$$

$$\begin{aligned}(\mathrm{II}) =&\kappa_0\Big\{2\pi(R_0H_0-2)^2+2\sqrt{\pi}H_0(R_0H_0-2)u_{0,0}\\&+\sum_{l,m}\frac{|u_{l,m}|^2}{2R_0^2}[(l-1)l(l+1)(l+2)-2R_0H_0l(l+1)+\frac{R_0^2H_0^2}{2}[2+l(l+1)]]\Big\}\end{aligned} \tag{4.65}$$

$$(\mathrm{III}) = 0 \tag{4.66}$$

$$(\mathrm{IV}) = \frac{\kappa_0 H_1^2 R_0^2}{2}\sum_{l,m}|w_{l,m}|^2. \tag{4.67}$$

$$(\mathrm{V}) = \kappa_1 H_0 H_1 R_0^2\sum_{l,m}|w_{l,m}|^2 + 2R_0\kappa_1 H_1\sum_{l,m}|w_{l,m}|^2 \tag{4.68}$$

$$(\mathrm{VI}) = 2R_0\kappa_0 H_0 H_1\left(\sqrt{\pi}R_0 w_{0,0}+\sum_{l,m}w_{l,m}^* u_{l,m}\right)-\kappa_0 H_1\left\{\sum_{l,m}[l(l+1)+2]w_{l,m}^* u_{l,m}+4\sqrt{\pi}R_0 w_{0,0}\right\} \tag{4.69}$$

and the optional Gaussian bending term (Equation (4.42)) is

$$\begin{aligned}-\int \mathrm{d}S\,\kappa[\phi]K &= -\kappa_1\int \mathrm{d}S\,K\phi-\kappa_0\int \mathrm{d}S\,K = -\kappa_1\int \mathrm{d}\Omega\,\left(\phi-\frac{\phi\widetilde{\nabla}^2 h}{R_0}\right)-4\pi\kappa_0\\&= -4\pi\kappa_0-2\sqrt{\pi}\kappa_1 w_{0,0}-\frac{\kappa_1}{R_0}\sum_{l,m}l(l+1)w_{l,m}^* u_{l,m}.\end{aligned} \tag{4.70}$$

Finally, we combine the obtained quadratic terms in $E_2$, including Landau-Ginzburg, Helfrich (I)–(VI), and optional Gaussian bending terms, to rewrite $E_2$ in the spherical harmonic space. Without Gaussian bending, we have $E_2$ equal to

$$\begin{aligned}&4\pi\sigma R_0^2+2\pi\kappa_0(R_0H_0-2)^2+\frac{4\pi}{3}pR_0^3+2\sqrt{\pi}[\kappa_0H_0(R_0H_0-2)+pR_0^2+2\sigma R_0]u_{0,0}\\&+\sqrt{\pi}[\kappa_1(2-R_0H_0)^2+2\kappa_0H_1R_0(H_0R_0-2)]w_{0,0}\\&+\sum_{l,m}\Big\{\sigma[1+\frac{l(l+1)}{2}]+pR_0+\frac{\kappa_0}{2R_0^2}[(l-1)l(l+1)(l+2)-2R_0H_0l(l+1)+\frac{R_0^2H_0^2}{2}(2+l(l+1))]\Big\}|u_{l,m}|^2\\&+\sum_{l,m}\Big\{\frac{\alpha R_0^2}{2}+\frac{\gamma}{2}l(l+1)+\left(\frac{\kappa_0H_1R_0}{2}+\kappa_1H_0R_0+2\kappa_1\right)H_1R_0\Big\}|w_{l,m}|^2\\&+\sum_{l,m}\Big\{\frac{\kappa_1}{R_0}(2-H_0R_0)[l(l+1)-R_0H_0]+\kappa_0H_1[2R_0H_0-(l(l+1)+2)]\Big\}w_{l,m}^*u_{l,m}\end{aligned} \tag{4.71}$$

and with Gaussian bending we have $E_2$ equal to

$$
\begin{aligned}
&4\pi\sigma R_0^2 + 2\pi\kappa_0(R_0^2H_0^2 - 4R_0H_0 + 2) + \frac{4\pi}{3}pR_0^3 + 2\sqrt{\pi}[\kappa_0H_0(R_0H_0 - 2) + pR_0^2 + 2\sigma R_0]u_{0,0} \\
&+ \sqrt{\pi}[\kappa_1(R_0^2H_0^2 - 4R_0H_0 + 2) + 2\kappa_0H_1R_0(H_0R_0 - 2)]w_{0,0} \\
&+ \sum_{l,m}\Big\{\sigma[1 + \frac{l(l+1)}{2}] + pR_0 + \frac{\kappa_0}{2R_0^2}[(l-1)l(l+1)(l+2) - 2R_0H_0l(l+1) + \frac{R_0^2H_0^2}{2}(2 + l(l+1))]\Big\}|u_{l,m}|^2 \\
&+ \sum_{l,m}\Big\{\frac{\alpha R_0^2}{2} + \frac{\gamma}{2}l(l+1) + \left(\frac{\kappa_0H_1R_0}{2} + \kappa_1H_0R_0 + 2\kappa_1\right)H_1R_0\Big\}|w_{l,m}|^2 \\
&+ \sum_{l,m}\Big\{\frac{\kappa_1}{R_0}[(1 - H_0R_0)l(l+1) - 2R_0H_0 + H_0^2R_0^2] + \kappa_0H_1[2R_0H_0 - (l(l+1) + 2)]\Big\}w_{l,m}^*u_{l,m}.
\end{aligned}
\tag{4.72}
$$

In the above derivations, we keep track of each term in the expansions using Mathematica. We focus on the non-constant part of $E_2$ (which depends on $w_{l,m}$ and $u_{l,m}$) in both situations for further analysis.

### *4.1.3 Constraints on surface area and composition, and reduction of shape deformation field*

To simplify the quadratic $E_2$ model in terms of spherical harmonic modes (Expression (4.71) or (4.72)), we attempt to reduce the surface deformation field $h(\theta, \varphi)$ and its spherical harmonic modes $u_{l,m}$ by optimizing $\Delta E$ with respect to them. Then the resulting $E_2$ will appear only dependent on the compositional field $\phi(\theta, \varphi)$ and therefore $w_{l,m}$. At the first step, we implement a constraint on the vesicular surface area, and another on the total amounts of ordered and disordered species which are equal:

$$
\int \mathrm{d}S = 4\pi R_0^2 + 4\sqrt{\pi}u_{0,0}R_0 + \sum_{l,m}|u_{l,m}|^2\left[1 + \frac{l(l+1)}{2}\right] = 4\pi R_0^2 \tag{4.73}
$$

$$
\int \mathrm{d}S\,\phi = 2\sqrt{\pi}R_0^2w_{0,0} + 2R_0\sum_{l,m}w_{l,m}^*u_{l,m} = 0 \tag{4.74}
$$

which lead to

$$
u_{0,0} = -\sum_{l,m}\frac{|u_{l,m}|^2}{4\sqrt{\pi}R_0}\left[1 + \frac{l(l+1)}{2}\right] = -\frac{u_{0,0}^2}{4\sqrt{\pi}R_0} - \sum_{l=1}^{\infty}\sum_{m=-l}^{l}\frac{|u_{l,m}|^2}{4\sqrt{\pi}R_0}\left[1 + \frac{l(l+1)}{2}\right] \tag{4.75}
$$

$$w_{0,0} = -\sum_{l,m} \frac{w_{l,m}^* u_{l,m}}{\sqrt{\pi} R_0} = -\frac{w_{0,0} u_{0,0}}{\sqrt{\pi} R_0} - \sum_{l=1}^{\infty} \sum_{m=-l}^{l} \frac{w_{l,m}^* u_{l,m}}{\sqrt{\pi} R_0}. \tag{4.76}$$

In Reference [94], $u_{0,0}^2$, $w_{0,0}^2$ and $w_{0,0}u_{0,0}$ are regarded as small amounts and are negligible from constraints (4.75) and (4.76) under quadratic approximation. Following this simplification we have

$$u_{0,0} \approx -\sum_{l=1}^{\infty} \sum_{m=-l}^{l} \frac{|u_{l,m}|^2}{4\sqrt{\pi} R_0} \left[1 + \frac{l(l+1)}{2}\right] \equiv \sum_{l>0,m} \frac{|u_{l,m}|^2}{4\sqrt{\pi} R_0} \left[1 + \frac{l(l+1)}{2}\right] \tag{4.77}$$

$$w_{0,0} \approx -\sum_{l=1}^{\infty} \sum_{m=-l}^{l} \frac{w_{l,m}^* u_{l,m}}{\sqrt{\pi} R_0} \equiv -\sum_{l>0,m} \frac{w_{l,m}^* u_{l,m}}{\sqrt{\pi} R_0}. \tag{4.78}$$

We consider the model with or without Gaussian bending separately by substituting Equations (4.77) and (4.78) into $\Delta E$, the nontrivial part of $E_2$ (Expression (4.71) or (4.72)), and disregarding $u_{0,0}^2$, $w_{0,0}^2$ and $w_{0,0}u_{0,0}$.

*Coupling model without Gaussian bending*

From Expression (4.71) we have

$$\begin{aligned}
\Delta E = & \sum_{l>0,m} \frac{l(l+1)-2}{4} \left\{ \frac{2\kappa_0}{R_0^2} [l(l+1) - H_0 R_0] - p R_0 \right\} |u_{l,m}|^2 \\
& + \sum_{l>0,m} \left\{ \frac{\alpha R_0^2}{2} + \frac{\gamma}{2} l(l+1) + \left( \frac{\kappa_0 H_1 R_0}{2} + \kappa_1 H_0 R_0 + 2\kappa_1 \right) H_1 R_0 \right\} |w_{l,m}|^2 \\
& - \sum_{l>0,m} [l(l+1) - 2] \left[ H_1 \kappa_0 + H_0 \kappa_1 - \frac{2\kappa_1}{R_0} \right] w_{l,m}^* u_{l,m}.
\end{aligned} \tag{4.79}$$

Spherical harmonic modes $w_{l,m}$ and $u_{l,m}$ are complex numbers, and we separate their real and imaginary parts $c_{l,m}$ and $s_{l,m}$[111]

$$w_{l,m} = \begin{cases} c_{l,m}^{(w)} & \text{if } m = 0 \\ (c_{l,m}^{(w)} - i s_{l,m}^{(w)})/\sqrt{2} & \text{if } m > 0 \\ (-1)^m (c_{l,-m}^{(w)} + i s_{l,-m}^{(w)})/\sqrt{2} & \text{if } m < 0 \end{cases} \tag{4.80}$$

$$u_{l,m} = \begin{cases} c^{(u)}_{l,m} & \text{if } m = 0 \\ (c^{(u)}_{l,m} - is^{(u)}_{l,m})/\sqrt{2} & \text{if } m > 0 \\ (-1)^m(c^{(u)}_{l,-m} + is^{(u)}_{l,-m})/\sqrt{2} & \text{if } m < 0 \end{cases} \tag{4.81}$$

so that we have

$$w^*_{l,m}u_{l,m} = \begin{cases} c^{(w)}_{l,m}c^{(u)}_{l,m} & \text{if } m = 0 \\ [(c^{(w)}_{l,m}c^{(u)}_{l,m} + s^{(w)}_{l,m}s^{(u)}_{l,m}) + i(s^{(w)}_{l,m}c^{(u)}_{l,m} - c^{(w)}_{l,m}s^{(u)}_{l,m})]/2 & \text{if } m > 0 \\ [(c^{(w)}_{l,-m}c^{(u)}_{l,-m} + s^{(w)}_{l,-m}s^{(u)}_{l,-m}) + i(c^{(w)}_{l,-m}s^{(u)}_{l,-m} - s^{(w)}_{l,-m}c^{(u)}_{l,-m})]/2 & \text{if } m < 0 \end{cases} \tag{4.82}$$

and for any function $f(l)$

$$\sum_{l=1}^{\infty}\sum_{m=-l}^{l} f(l)|w_{l,m}|^2 = \sum_{l=1}^{\infty}\sum_{m=0}^{l} f(l)[(c^{(w)}_{l,m})^2 + (s^{(w)}_{l,m})^2] \tag{4.83}$$

$$\sum_{l=1}^{\infty}\sum_{m=-l}^{l} f(l)|u_{l,m}|^2 = \sum_{l=1}^{\infty}\sum_{m=0}^{l} f(l)[(c^{(u)}_{l,m})^2 + (s^{(u)}_{l,m})^2] \tag{4.84}$$

$$\sum_{l=1}^{\infty}\sum_{m=-l}^{l} f(l)w^*_{l,m}u_{l,m} = \sum_{l=1}^{\infty}\sum_{m=0}^{l} f(l)(c^{(w)}_{l,m}c^{(u)}_{l,m} + s^{(w)}_{l,m}s^{(u)}_{l,m}). \tag{4.85}$$

All real and imaginary parts are independent variables for $l > 0$ and $0 \leqslant m \leqslant l$.

Then Equation (4.79) becomes

$$\begin{aligned} \Delta E = & \sum_{l>0,m\geqslant 0} \frac{l(l+1)-2}{4}\left\{\frac{2\kappa_0}{R_0^2}[l(l+1) - H_0R_0] - pR_0\right\}[(c^{(u)}_{l,m})^2 + (s^{(u)}_{l,m})^2] \\ & + \sum_{l>0,m\geqslant 0}\left\{\frac{\alpha R_0^2}{2} + \frac{\gamma}{2}l(l+1) + \left(\frac{\kappa_0 H_1 R_0}{2} + \kappa_1 H_0 R_0 + 2\kappa_1\right)H_1R_0\right\}[(c^{(w)}_{l,m})^2 + (s^{(w)}_{l,m})^2] \\ & - \sum_{l>0,m\geqslant 0}[l(l+1)-2]\left[H_1\kappa_0 + H_0\kappa_1 - \frac{2\kappa_1}{R_0}\right](c^{(w)}_{l,m}c^{(u)}_{l,m} + s^{(w)}_{l,m}s^{(u)}_{l,m}) \end{aligned} \tag{4.86}$$

in which

$$\sum_{l=1}^{\infty}\sum_{m=0}^{l} \equiv \sum_{l>0,m\geqslant 0}. \tag{4.87}$$

For each spherical harmonic degree set ($l > 0$, $m \geqslant 0$), we minimize $\Delta E$ with respect to $u_{l,m}$ by solving

$$\frac{\partial(\Delta E)}{\partial c_{l,m}^{(u)}} = 0 \tag{4.88}$$

$$\frac{\partial(\Delta E)}{\partial s_{l,m}^{(u)}} = 0. \tag{4.89}$$

The solutions are

$$c_{l,m}^{(u)} = \frac{2R_0[R_0H_1\kappa_0 + R_0H_0\kappa_1 - 2\kappa_1]}{2\kappa_0[l(l+1) - H_0R_0] - pR_0^3} c_{l,m}^{(w)} \tag{4.90}$$

$$s_{l,m}^{(u)} = \frac{2R_0[R_0H_1\kappa_0 + R_0H_0\kappa_1 - 2\kappa_1]}{2\kappa_0[l(l+1) - H_0R_0] - pR_0^3} s_{l,m}^{(w)}, \tag{4.91}$$

which change Equation (4.79) into

$$\begin{aligned}\Delta E = \sum_{l>0,m} \Big\{ &\frac{\alpha R_0^2}{2} + \frac{\gamma}{2} l(l+1) + \left( \frac{\kappa_0 H_1 R_0}{2} + \kappa_1 H_0 R_0 + 2\kappa_1 \right) H_1 R_0 \\ &- \frac{[l(l+1)-2][H_1R_0\kappa_0 + (H_0R_0 - 2)\kappa_1]^2}{2[l(l+1) - H_0R_0]\kappa_0 - pR_0^3} \Big\} |w_{l,m}|^2 \end{aligned} \tag{4.92}$$

which is a composition-only expression, i.e., it does not depend on the shape variables $u_{l,m}$.

*Coupling model with Gaussian bending*

From Expression (4.72) we have

$$\begin{aligned}
\Delta E = &\sum_{l>0,m} \frac{l(l+1)-2}{4}\Big\{\frac{2\kappa_0}{R_0^2}[l(l+1)-H_0R_0]-pR_0\Big\}|u_{l,m}|^2 \\
&+\sum_{l>0,m}\Big\{\frac{\alpha R_0^2}{2}+\frac{\gamma}{2}l(l+1)+\left(\frac{\kappa_0 H_1 R_0}{2}+\kappa_1 H_0 R_0+2\kappa_1\right)H_1R_0\Big\}|w_{l,m}|^2 \\
&-\sum_{l>0,m}[l(l+1)-2]\left[H_1\kappa_0+H_0\kappa_1-\frac{\kappa_1}{R_0}\right]w_{l,m}^* u_{l,m} \\
= &\sum_{l>0,m\geqslant 0} \frac{l(l+1)-2}{4}\Big\{\frac{2\kappa_0}{R_0^2}[l(l+1)-H_0R_0]-pR_0\Big\}[(c_{l,m}^{(u)})^2+(s_{l,m}^{(u)})^2] \\
&+\sum_{l>0,m\geqslant 0}\Big\{\frac{\alpha R_0^2}{2}+\frac{\gamma}{2}l(l+1)+\left(\frac{\kappa_0 H_1 R_0}{2}+\kappa_1 H_0 R_0+2\kappa_1\right)H_1R_0\Big\}[(c_{l,m}^{(w)})^2+(s_{l,m}^{(w)})^2] \\
&-\sum_{l>0,m\geqslant 0}[l(l+1)-2]\left[H_1\kappa_0+H_0\kappa_1-\frac{\kappa_1}{R_0}\right](c_{l,m}^{(w)}c_{l,m}^{(u)}+s_{l,m}^{(w)}s_{l,m}^{(u)}).
\end{aligned} \tag{4.93}$$

The reduction of $u_{l,m}$ (by solving $\partial(\Delta E)/\partial c_{l,m}^{(u)}=0$ and $\partial(\Delta E)/\partial s_{l,m}^{(u)}=0$) requires

$$c_{l,m}^{(u)} = \frac{2R_0[R_0H_1\kappa_0+R_0H_0\kappa_1-\kappa_1]}{2\kappa_0[l(l+1)-H_0R_0]-pR_0^3}c_{l,m}^{(w)} \tag{4.94}$$

$$s_{l,m}^{(u)} = \frac{2R_0[R_0H_1\kappa_0+R_0H_0\kappa_1-\kappa_1]}{2\kappa_0[l(l+1)-H_0R_0]-pR_0^3}s_{l,m}^{(w)} \tag{4.95}$$

which change $\Delta E$ into

$$\begin{aligned}
\Delta E = \sum_{l>0,m}\Big\{&\frac{\alpha R_0^2}{2}+\frac{\gamma}{2}l(l+1)+\left(\frac{\kappa_0 H_1 R_0}{2}+\kappa_1 H_0 R_0+2\kappa_1\right)H_1R_0 \\
&-\frac{[l(l+1)-2][H_1R_0\kappa_0+(H_0R_0-1)\kappa_1]^2}{2[l(l+1)-H_0R_0]\kappa_0-pR_0^3}\Big\}|w_{l,m}|^2,
\end{aligned} \tag{4.96}$$

which is also a composition-only expression.

We have reduced the quadratic part of the model, $E_2$, into a homogeneous quadratic series of $w_{l,m}$, just like the Gaussian model in Chapter 3. The quartic term $E_4$ is also a functional of $w_{l,m}$ only, and so is the full model $E = E_2 + E_4$. We can find a spherical

harmonic set $\{w_{l,m}\}$ from $l = 1$ to $l_{\max}$ that minimizes $\Delta E + E_4$ and also minimizes $E_2 + E_4$ because $E_2 = \Delta E + \text{const}$. The $\{w_{l,m}\}$ set can be converted back to the real space and generate a surface pattern $\phi(\theta, \varphi)$ which is the ground state lateral pattern. We use the same computational techniques as in Chapter 2, including single-mode, axisymmetric full-mode and non-axisymmetric full-mode methods, to calculate different types of ground state phase diagrams. We show that even without using an extended Landau-Ginzburg model and a negative interface line tension, the composition-curvature coupling can also produce modulated phases and stripe domains.

## *4.2 Methods of ground state phase diagram calculation*

In the ground state calculation of the optimal spherical harmonic set $\{w_{l,m}\}$ that minimizes $E' = \Delta E + E_4$, the single-mode approximation is operated analytically (in Mathematica), and the full-mode methods are handled in the numerical way (in the Python programming language). There are two full-mode approaches, based on whether we assume the resulting surface pattern to be axisymmetric in ground state. This assumption, which is applied in Chapter 2 on a spherical surface, indicates that in the absence of thermal fluctuations, a modulated phase would consist of parallelly aligned stripes circling around the polar direction, and the order parameter becomes independent of the azimuthal angle $\varphi$, meaning only $w_{l,0}$ terms could be nonzero. Under this assumption, we can determine the dominant spherical harmonic degree $l^*$ by observing the resulting surface pattern and counting the number of interfaces between domains. The axisymmetric full-mode approximation is simplified from the real, non-axisymmetric full-mode approach, which still generates axisymmetric surface patterns for most points in the phase diagrams, though not necessarily around the z axis, validating the effectiveness of the axisymmetric assumption to a great extent.

All three methods, single-mode, axisymmetric full-mode and non-axisymmetric full-mode, will be illustrated and their resulting phase diagrams for $E'$ without Gaussian bending (based on $\Delta E$ in Equation (4.92)) and $E'$ with Gaussian bending (based on $\Delta E$ in Equation (4.96)) will be shown. Some examples of surface patterns generated by the non-axisymmetric full-

mode approach will also be shown. We use the following reduced parameters similar to those used in Reference [94],

$$\tilde{\alpha} = \frac{\alpha\kappa_0 R_0^2}{\kappa_1^2} \tag{4.97}$$

$$\tilde{b} = \frac{b\kappa_0 R_0^2}{\kappa_1^2} \tag{4.98}$$

$$\tilde{\gamma} = \frac{\gamma\kappa_0}{\kappa_1^2} \tag{4.99}$$

$$\tilde{p} = \frac{pR_0^3}{\kappa_0}, \tag{4.100}$$

and for a better comparison with literature[94, 47] we study the situation of zero spontaneous curvature $H_s = 0$ which means

$$H_0 = H_1 = 0. \tag{4.101}$$

Without Gaussian bending, these parameters simplify Equation (4.92) into

$$\begin{aligned}\Delta E &= \sum_{l>0,m} \left[\frac{\alpha}{2}R_0^2 + \frac{\gamma}{2}l(l+1) + \frac{4(l-1)(l+2)\kappa_1^2}{pR_0^3 - 2l(l+1)\kappa_0}\right]|w_{l,m}|^2 \\ &= \frac{\kappa_1^2}{\kappa_0}\sum_{l>0,m}\left[\frac{\tilde{\alpha}}{2} + \frac{\tilde{\gamma}}{2}l(l+1) + \frac{4(l-1)(l+2)}{\tilde{p} - 2l(l+1)}\right]|w_{l,m}|^2\end{aligned} \tag{4.102}$$

and constraints (Equations (4.77) and (4.78)) into

$$\begin{aligned}u_{0,0} &= -\sum_{l>0,m}\frac{|w_{l,m}|^2}{4\sqrt{\pi}R_0}\left[1 + \frac{l(l+1)}{2}\right]\left[\frac{4R_0\kappa_1}{pR_0^3 - 2l(l+1)\kappa_0}\right]^2 \\ &= -\sum_{l>0,m}\frac{|w_{l,m}|^2}{4\sqrt{\pi}R_0}\left[1 + \frac{l(l+1)}{2}\right]\left[\frac{4R_0\kappa_1/\kappa_0}{\tilde{p} - 2l(l+1)}\right]^2\end{aligned} \tag{4.103}$$

$$w_{0,0} = -\sum_{l>0,m}\frac{|w_{l,m}|^2}{\sqrt{\pi}R_0}\left[\frac{4R_0\kappa_1}{pR_0^3 - 2l(l+1)\kappa_0}\right] = -\sum_{l>0,m}\frac{|w_{l,m}|^2}{\sqrt{\pi}}\left[\frac{4\kappa_1/\kappa_0}{\tilde{p} - 2l(l+1)}\right]. \tag{4.104}$$

With the Gaussian bending term, Equation (4.96) is simplified into

$$\begin{aligned}\Delta E &= \sum_{l>0,m}\left[\frac{\alpha}{2}R_0^2 + \frac{\gamma}{2}l(l+1) + \frac{(l-1)(l+2)\kappa_1^2}{pR_0^3 - 2l(l+1)\kappa_0}\right]|w_{l,m}|^2 \\ &= \frac{\kappa_1^2}{\kappa_0}\sum_{l>0,m}\left[\frac{\tilde{\alpha}}{2} + \frac{\tilde{\gamma}}{2}l(l+1) + \frac{(l-1)(l+2)}{\tilde{p} - 2l(l+1)}\right]|w_{l,m}|^2\end{aligned} \tag{4.105}$$

with constraints (Equations (4.77) and (4.78))

$$\begin{aligned} u_{0,0} &= -\sum_{l>0,m} \frac{|w_{l,m}|^2}{4\sqrt{\pi}R_0}\left[1+\frac{l(l+1)}{2}\right]\left[\frac{2R_0\kappa_1}{pR_0^3-2l(l+1)\kappa_0}\right]^2 \\ &= -\sum_{l>0,m} \frac{|w_{l,m}|^2}{4\sqrt{\pi}R_0}\left[1+\frac{l(l+1)}{2}\right]\left[\frac{2R_0\kappa_1/\kappa_0}{\tilde{p}-2l(l+1)}\right]^2 \end{aligned} \tag{4.106}$$

$$w_{0,0} = -\sum_{l>0,m} \frac{|w_{l,m}|^2}{\sqrt{\pi}R_0}\left[\frac{2R_0\kappa_1}{pR_0^3-2l(l+1)\kappa_0}\right] = -\sum_{l>0,m} \frac{|w_{l,m}|^2}{\sqrt{\pi}}\left[\frac{2\kappa_1/\kappa_0}{\tilde{p}-2l(l+1)}\right]. \tag{4.107}$$

We study two types of phase diagrams: $\tilde{p}$ vs. $\tilde{\gamma}^{-1/2}$ when $\tilde{\alpha}=0$, and $\tilde{\alpha}$ vs. $\tilde{\gamma}^{-1/2}$ when $\tilde{p}=0$. Including and excluding Gaussian bending, each method generates four phase diagrams in total, all plotted with $0<\tilde{\gamma}^{-1/2}<10$ and intervals between neighboring sampling points $\Delta(\tilde{\gamma}^{-1/2})=0.2$. We consider $-15<\tilde{p}<15$ with $\Delta\tilde{p}=0.5$, and $-5<\tilde{\alpha}<5$ with $\Delta\tilde{\alpha}=0.2$. At each sampling point ($\tilde{p}$, $\tilde{\gamma}^{-1/2}$) or ($\tilde{\alpha}$, $\tilde{\gamma}^{-1/2}$), we find the ground state and determine its lateral phase by observing the visual illustration of surface pattern, without referring to spherical harmonic means $\langle w_{l,m}\rangle$ and variances $\langle|\delta w_{l,m}|^2\rangle$.

### *4.2.1 Single-mode analytical method*

The single-mode expression of the order parameter is

$$\phi(\theta) = w_{l,0}Y_{l,0}(\theta) \tag{4.108}$$

and the expression of $E'=\Delta E+E_4$ is (without Gaussian bending)

$$E' = \frac{\kappa_1^2}{\kappa_0}\left\{\left[\frac{\tilde{\alpha}}{2}+\frac{\tilde{\gamma}}{2}l(l+1)+\frac{4(l-1)(l+2)}{\tilde{p}-2l(l+1)}\right]w_{l,0}^2+\frac{\tilde{b}}{4}\sum_{l'=0}^{2l}\frac{(2l+1)^2(2l'+1)}{4\pi}\left|\begin{pmatrix} l & l & l' \\ 0 & 0 & 0\end{pmatrix}\right|^4 w_{l,0}^4\right\} \tag{4.109}$$

or (with Gaussian bending)

$$E' = \frac{\kappa_1^2}{\kappa_0}\left\{\left[\frac{\tilde{\alpha}}{2}+\frac{\tilde{\gamma}}{2}l(l+1)+\frac{(l-1)(l+2)}{\tilde{p}-2l(l+1)}\right]w_{l,0}^2+\frac{\tilde{b}}{4}\sum_{l'=0}^{2l}\frac{(2l+1)^2(2l'+1)}{4\pi}\left|\begin{pmatrix} l & l & l' \\ 0 & 0 & 0\end{pmatrix}\right|^4 w_{l,0}^4\right\}. \tag{4.110}$$

The minimization is done analytically for each $w_{l,0}$ from $l = 1$ to $l_{\max} = 21$. In a homogeneous phase, we have all $w_{l,0} = 0$ and $E' = 0$. And in a modulated phase, the one $w_{l,0}$ that gives the lowest negative energy reveals the value of $l^*$.

### *4.2.2 Axisymmetric full-mode approximation*

The axisymmetric full-mode expression of $\phi(\theta)$ is

$$\phi(\theta) = \sum_{l=0}^{l_{\max}} w_{l,0} Y_{l,0}(\theta) \tag{4.111}$$

where $l_{\max} = 21$, $w_{0,0}$ is determined by other $w_{l,0}$ of $l > 0$ through Equations (4.77) and (4.78), and $E' = \Delta E + E_4$ is (without Gaussian bending)

$$\begin{aligned} E' =& \frac{\kappa_1^2}{\kappa_0} \left\{ \sum_{l=1}^{l_{\max}} \left[ \frac{\tilde{\alpha}}{2} + \frac{\tilde{\gamma}}{2} l(l+1) + \frac{4(l-1)(l+2)}{\tilde{p} - 2l(l+1)} \right] w_{l,0}^2 \right. \\ & \left. + \frac{\tilde{b}}{4} \sum_{l=0}^{2l_{\max}} \left[ \sum_{l_1=1}^{l_{\max}} \sum_{l_2=1}^{l_{\max}} \sqrt{\frac{(2l_1+1)(2l_2+1)(2l+1)}{4\pi}} \begin{pmatrix} l_1 & l_2 & l \\ 0 & 0 & 0 \end{pmatrix}^2 w_{l_1,0} w_{l_2,0} \right]^2 \right\} \end{aligned} \tag{4.112}$$

or (with Gaussian bending)

$$\begin{aligned} E' =& \frac{\kappa_1^2}{\kappa_0} \left\{ \sum_{l=1}^{l_{\max}} \left[ \frac{\tilde{\alpha}}{2} + \frac{\tilde{\gamma}}{2} l(l+1) + \frac{(l-1)(l+2)}{\tilde{p} - 2l(l+1)} \right] w_{l,0}^2 \right. \\ & \left. + \frac{\tilde{b}}{4} \sum_{l=0}^{2l_{\max}} \left[ \sum_{l_1=1}^{l_{\max}} \sum_{l_2=1}^{l_{\max}} \sqrt{\frac{(2l_1+1)(2l_2+1)(2l+1}{4\pi}} \begin{pmatrix} l_1 & l_2 & l \\ 0 & 0 & 0 \end{pmatrix}^2 w_{l_1,0} w_{l_2,0} \right]^2 \right\}. \end{aligned} \tag{4.113}$$

The minimization is done numerically using the Sequential Least Squares Programming (SLSQP) optimization algorithm to find the ground state $\{w_{l,0}\}$, which reveals the surface pattern in real space.

### *4.2.3 Non-axisymmetric full-mode method*

The non-axisymmetric full-mode order parameter is

$$\phi(\theta, \varphi) = \sum_{l=0}^{l_{\max}} \sum_{m=-l}^{l} w_{l,m} Y_{l,m}(\theta, \varphi) \tag{4.114}$$

where we also have $l_{\max} = 21$ and $w_{0,0}$ determined by other $w_{l,m}$ of $l > 0$, and $E' = \Delta E + E_4$ (without Gaussian bending)

$$E' = \frac{\kappa_1^2}{\kappa_0} \left\{ \sum_{l>0,m} \left[ \frac{\tilde{\alpha}}{2} + \frac{\tilde{\gamma}}{2} l(l+1) + \frac{4(l-1)(l+2)}{\tilde{p} - 2l(l+1)} \right] |w_{l,m}|^2 + \frac{\tilde{b}}{4} \sum_{l,m} \left| \sum_{l_1>0,m_1} \sum_{l_2>0,m_2} \sqrt{\frac{(2l_1+1)(2l_2+1)(2l+1)}{4\pi}} \begin{pmatrix} l_1 & l_2 & l \\ 0 & 0 & 0 \end{pmatrix} \begin{pmatrix} l_1 & l_2 & l \\ m_1 & m_2 & m \end{pmatrix} w_{l_1,m_1} w_{l_2,m_2} \right|^2 \right\} \tag{4.115}$$

or (with Gaussian bending)

$$E' = \frac{\kappa_1^2}{\kappa_0} \left\{ \sum_{l>0,m} \left[ \frac{\tilde{\alpha}}{2} + \frac{\tilde{\gamma}}{2} l(l+1) + \frac{(l-1)(l+2)}{\tilde{p} - 2l(l+1)} \right] |w_{l,m}|^2 + \frac{\tilde{b}}{4} \sum_{l,m} \left| \sum_{l_1>0,m_1} \sum_{l_2>0,m_2} \sqrt{\frac{(2l_1+1)(2l_2+1)(2l+1)}{4\pi}} \begin{pmatrix} l_1 & l_2 & l \\ 0 & 0 & 0 \end{pmatrix} \begin{pmatrix} l_1 & l_2 & l \\ m_1 & m_2 & m \end{pmatrix} w_{l_1,m_1} w_{l_2,m_2} \right|^2 \right\}. \tag{4.116}$$

The minimization is also done using SLSQP to find the ground state $\{w_{l,m}\}$ over all $1 \leqslant l \leqslant l_{\max}$ and $-l \leqslant m \leqslant l$.

### *4.3 Results and discussion*

For all ground state phase diagram calculations we choose $\tilde{b} = 1$ without loss of generality. The single-mode results are shown in Figure 4.1, axisymmetric full-mode results in Figure 4.2 and non-axisymmetric full-mode results in Figure 4.3. In each figure, in the left columns are phase diagrams without Gaussian bending, and in the right columns are results with Gaussian bending. In rows (a) are diagrams of $\tilde{p}$ vs. $\tilde{\gamma}^{-1/2}$ when $\tilde{\alpha} = 0$, and in rows (b) are those of $\tilde{\alpha}$ vs. $\tilde{\gamma}^{-1/2}$ when $\tilde{p} = 0$. All phase diagrams of the same kind are qualitatively similar, which implies that all three ground state computation methods with different levels of approximation lead to similar results. The phase diagrams in the left columns are qualitatively comparable to results in Reference [94], which includes an explicit coupling term $\int \mathrm{d}S\, H\phi$ in the free energy model, while we use implicit couplings which also include $\int \mathrm{d}S\, H^2\phi$ and $\int \mathrm{d}S\, H\phi^2$.

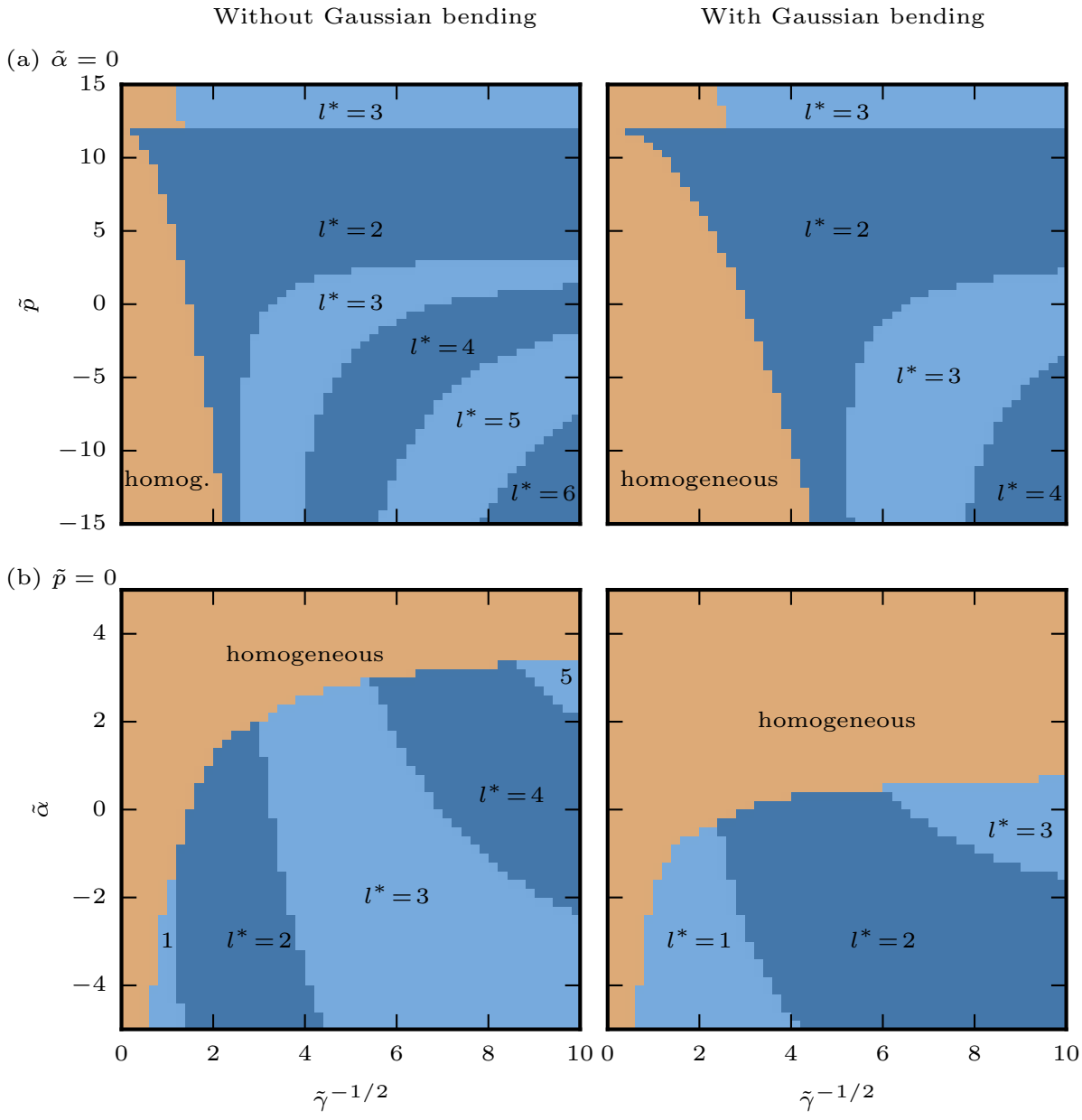


Figure 4.1: Single-mode ground state phase diagrams of deformable vesicles with composition-curvature coupling. (a) $\tilde{p}$ vs. $\tilde{\gamma}^{-1/2}$ when $\tilde{\alpha} = 0$. (b) $\tilde{\alpha}$ vs. $\tilde{\gamma}^{-1/2}$ when $\tilde{p} = 0$. Left column: Gaussian bending not included. Right column: Gaussian bending included.

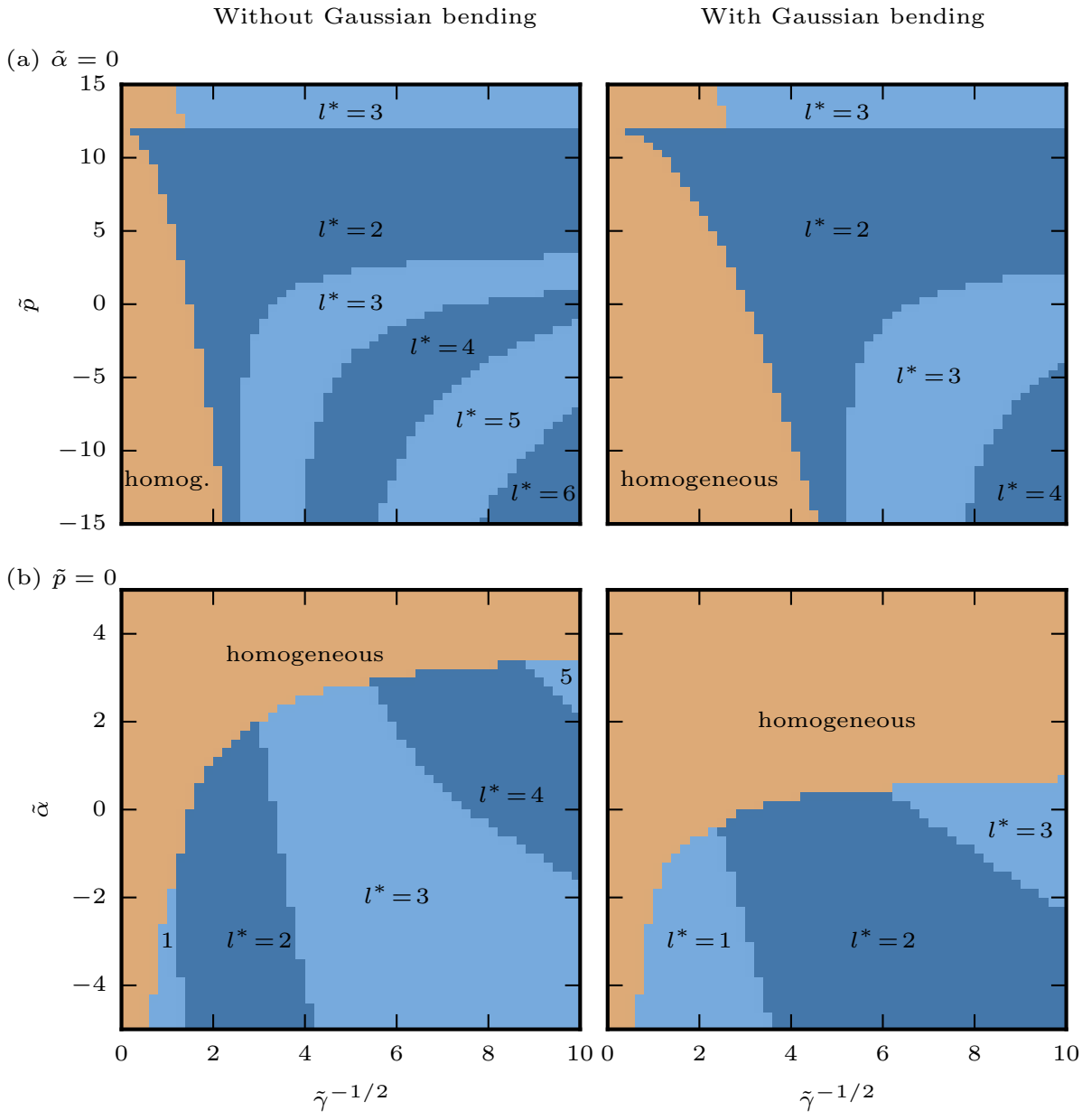


Figure 4.2: Axisymmetric full-mode ground state phase diagrams of deformable vesicles with composition-curvature coupling. (a) $\tilde{p}$ vs. $\tilde{\gamma}^{-1/2}$ when $\tilde{\alpha} = 0$. (b) $\tilde{\alpha}$ vs. $\tilde{\gamma}^{-1/2}$ when $\tilde{p} = 0$. Left column: Gaussian bending not included. Right column: Gaussian bending included.

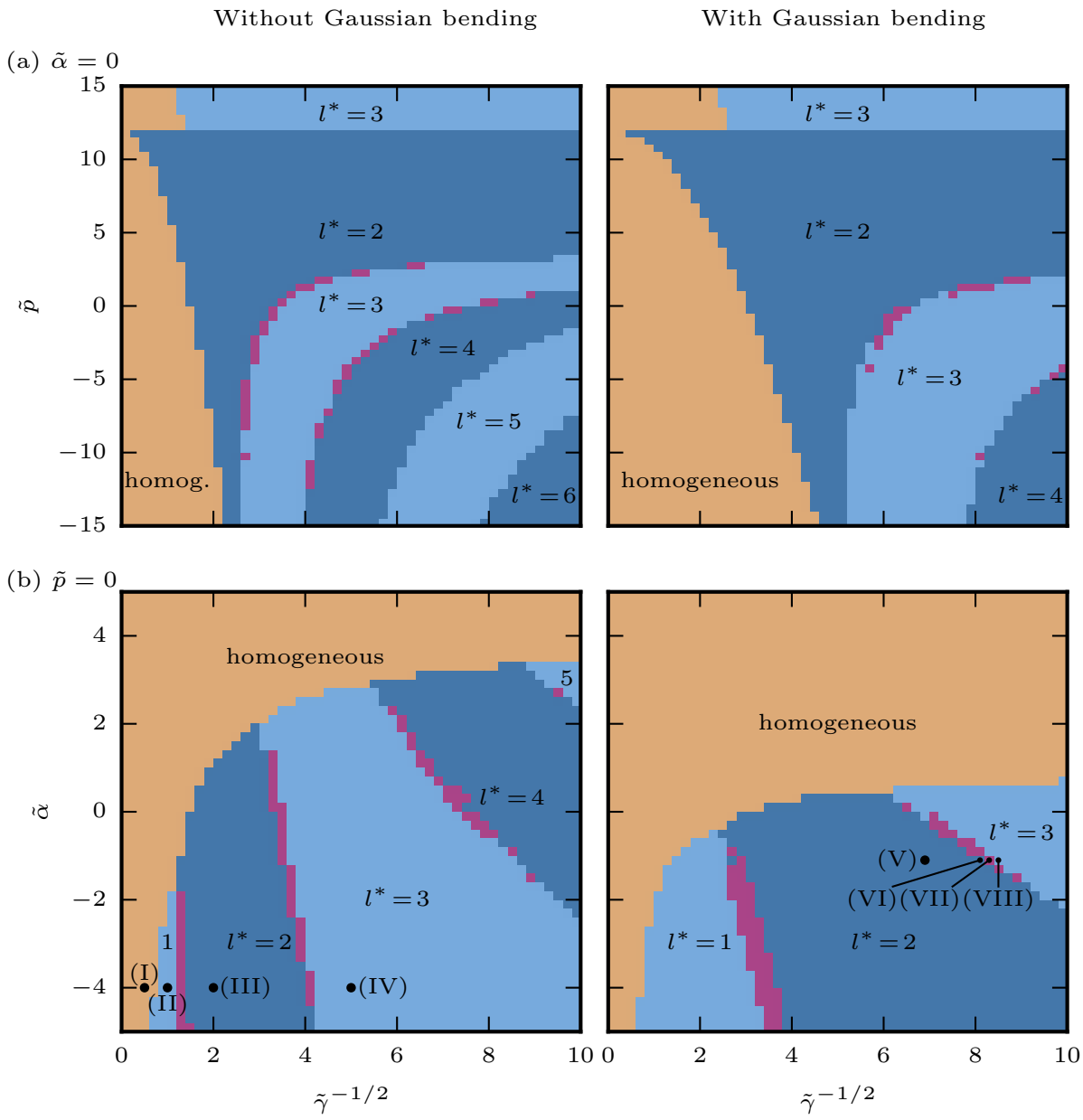


Figure 4.3: Non-axisymmetric full-mode ground state phase diagrams of deformable vesicles with composition-curvature coupling. (a) $\tilde{p}$ vs. $\tilde{\gamma}^{-1/2}$ when $\tilde{\alpha} = 0$. (b) $\tilde{\alpha}$ vs. $\tilde{\gamma}^{-1/2}$ when $\tilde{p} = 0$. Left column: Gaussian bending not included. Right column: Gaussian bending included. Purple regions indicate the locations of intermediate "spiral" phases. Surface patterns of points (I)–(IV) are illustrated in Figure 4.4 and those of points (V)–(VIII) are in Figure 4.5 (I: $\tilde{\alpha} = -4$, $\tilde{\gamma}^{-1/2} = 0.5$; II: $\tilde{\alpha} = -4$, $\tilde{\gamma}^{-1/2} = 1$; III: $\tilde{\alpha} = -4$, $\tilde{\gamma}^{-1/2} = 2$; IV: $\tilde{\alpha} = -4$, $\tilde{\gamma}^{-1/2} = 5$; V: $\tilde{\alpha} = -1.1$, $\tilde{\gamma}^{-1/2} = 6.9$; VI: $\tilde{\alpha} = -1.1$, $\tilde{\gamma}^{-1/2} = 8.1$; VII: $\tilde{\alpha} = -1.1$, $\tilde{\gamma}^{-1/2} = 8.3$; VIII: $\tilde{\alpha} = -1.1$, $\tilde{\gamma}^{-1/2} = 8.5$).

Because of the constraint on surface composition, in the two-phase coexistence state the order parameter does not form a single phase with $\phi = 0$, but instead separates into two coexisting phases. This makes the two-phase coexistence indistinguishable from a modulated phase dominated by $l^* = 1$. In fact, it would be unnecessary to make the distinction in experiments and simulations. One important observation is that at $\tilde{\alpha} = 0$ there is not an $l^* = 1$ phase region in the diagrams in rows (a). This could be well explained by phase diagrams in rows (b) when $\tilde{p} = 0$. The $l^* = 1$ region, which includes two-phase coexistence, only happens when $\tilde{\alpha} < 0$. This is in agreement with the conclusion drawn from both standard and extended Landau-Ginzburg models, which state that the two-phase coexistence happens only when $\alpha < 0$. Because of the coupling between shape and composition, the phase separation from the homogeneous phase into $l^* = 1$ does not take place exactly at $\tilde{\alpha} = 0$.

Phase diagrams in the right columns with Gaussian bending have fewer modulated regions and lower $l^*$ values shown than diagrams in left columns without Gaussian bending in the same range. This is different from the finite size effect at small spherical radius in Chapter 2. Because of the Gaussian bending modulus $\bar{\kappa} = -\kappa$, the inclusion of the Gaussian bending term counteracts the effect of mismatch between bending moduli $\kappa_{\rm lo}$ and $\kappa_{\rm ld}$ that gives rise to modulated phases. The Gaussian bending effectively lowers the curvature mismatch between liquid-ordered and liquid-disordered domains, making it unnecessary to decrease domain size and increase $l^*$ to offset the curvature mismatch and still keep the vesicular shape near-spherical.

The bending modulus mismatch, with or without Gaussian bending, is mainly counteracted by the reduced Landau-Ginzburg parameter $\tilde{\gamma} > 0$ which implies a positive interface line tension between domains. The line tension prefers less interface and would induce a two-phase coexistence at large $\tilde{\gamma}$ (small $\tilde{\gamma}^{-1/2}$) when $\tilde{\alpha} < 0$. As $\tilde{\gamma}$ decreases and $\tilde{\gamma}^{-1/2}$ increases, the two-phase coexistence would give way to a modulated phase of $l^* > 1$, which has more domains and more interface, but also smaller domains (narrower stripes) with less curvature and less total bending energy. The smaller $\tilde{\gamma}$, the smaller the domains and the greater the $l^*$, so that the bending energy can be lowered even when the bending modulus contrast remains

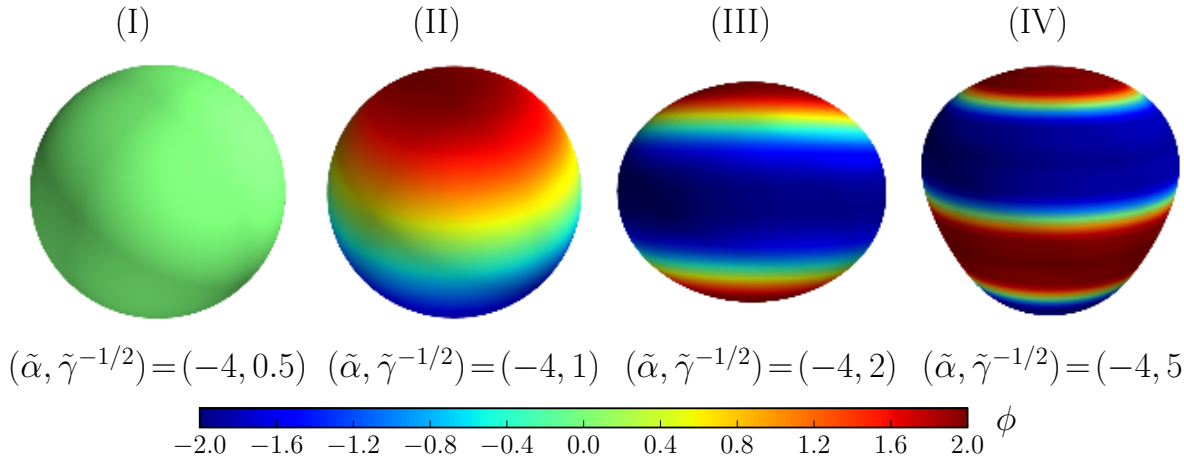


Figure 4.4: Examples of lateral patterns on the surface of a vesicle at points (I)–(IV) in Figure 4.3 (b) without Gaussian bending. (I) is in the homogeneous region, (II) in $l^* = 1$ region, (III) in $l^* = 2$ region and (IV) in $l^* = 3$ region. Shape deformations are shown with the surface order parameter distribution scaled by the color bar.

the same. This effect of decreasing $\tilde{\gamma}$ (increasing $\tilde{\gamma}^{-1/2}$) is observed in all phase diagrams. The reduced parameters used here have included bending modulus parameters $\kappa_0$ and $\kappa_1$ and radius $R_0$, which are not varied in this study.

In rows (a), decreasing the reduced osmotic pressure $\tilde{p}$ (making it more negative) could have the same effect as decreasing $\tilde{\gamma}$, giving rise to modulated phases of greater $l^*$. With a negative $\tilde{p}$, the pressure from the inside of a vesicle exceeds that from the outside. The larger the internal pressure, the more likely the vesicle to be in a near-spherical shape, and that requires decreasing curvature contrast by making domains smaller (stripes narrower) and $l^*$ larger. There is also an $l^* = 3$ region above the $l^* = 2$ region, with the former at a greater positive pressure than the latter, which seems contrary to the trend. But the boundary between the regions, $\tilde{p} = 12$, is a critical osmotic pressure where our model collapses and energy diverges to negative infinity. In this theoretical study, we are unable to predict the phenomenon of crossing the boundary at $\tilde{p} = 12$ from $l^* = 2$ to $l^* = 3$, or whether this transition is physical.

In Figure 4.3, most resulting surface patterns from the real full-mode method without a constraint of $\varphi$-independence would still be axisymmetric. These axisymmetric patterns are easily categorized into either the homogeneous phase or one of the modulated phases with an integer $l^*$. Examples are extracted from the left diagram of Figure 4.3 (b) without Gaussian bending, at points (I) in the homogeneous region, (II) in $l^* = 1$ region, (III) in $l^* = 2$ region and (IV) in $l^* = 3$ region. Based on existing literature, we can estimate some physical properties such as interface width and line tension which is experimentally measurable, and compare them with our observations. The size of giant unilamellar vesicles such as those used and simulated in Reference [47] is usually in the tens of micrometers, and a bending modulus is usually in the order of magnitude of $1\text{–}100\times10^{-19}$J or 0.1–10 aJ. Because of the quadratic approximation, the vesicle is not allowed to undergo a large deformation, so that the bending modulus and curvature contrast between liquid-ordered and liquid-disordered domains is small. We assume $\kappa_{\mathrm{lo}}$ is not much larger than $\kappa_{\mathrm{ld}}$ (e.g. $\kappa_{\mathrm{lo}} = 11\,\mathrm{aJ}$ and $\kappa_{\mathrm{ld}} = 9\,\mathrm{aJ}$) and $\kappa_0 \gg \kappa_1$, and use the following parameters

$$R_0 = 10\,\mu\mathrm{m} \tag{4.117}$$

$$\kappa_0 = 10\,\mathrm{aJ} \tag{4.118}$$

$$\kappa_1 = 1\,\mathrm{aJ}. \tag{4.119}$$

Also using $\tilde{b} = 1$, we calculate interface width $d$ and line tension $\Gamma$ at points (I)–(IV) through

$$d = \sqrt{-\frac{2\gamma}{\alpha}} = R_0\sqrt{-\frac{2\tilde{\gamma}}{\tilde{\alpha}}} \tag{4.120}$$

$$\Gamma = \sqrt{-\frac{8\gamma\alpha^3}{9b^2}} = \frac{\kappa_1^2}{R_0\kappa_0}\sqrt{-\frac{8\tilde{\gamma}\tilde{\alpha}^3}{9\tilde{b}^2}}. \tag{4.121}$$

For each point, the vesicular surface pattern as well as shape change is shown in Figure 4.4 .

At point (I), we calculate the line tension as

$$\Gamma = 0.15\,\mathrm{pN} \tag{4.122}$$

which is smaller than typical experimental values ($\sim 1\,\mathrm{pN}$) but way greater than previously used simulation values ($\sim 0.01\,\mathrm{pN}$)[47], and would induce a two-phase coexistence since $\tilde{\alpha} = -4 < 0$. However, we also calculate the interface width in a phase separation to be

$$d = 14\,\mu\mathrm{m} \tag{4.123}$$

which is greater than the radius $R_0 = 10\,\mu\mathrm{m}$. The spherical size is not able to contain such a wide interface and the system remains in a homogeneous phase. At point (II) we have

$$\Gamma = 0.075\,\mathrm{pN} \tag{4.124}$$

$$d = 7\,\mu\mathrm{m}, \tag{4.125}$$

which is comparable to $R_0$, and the system shows a weak segregation into two coexisting phases, which is clearly illustrated by the wide interface between the $\phi > 0$ domain and the $\phi < 0$ domain in Figure 4.4. At point (III) we have

$$\Gamma = 0.038\,\mathrm{pN} \tag{4.126}$$

$$d = 3.5\,\mu\mathrm{m}. \tag{4.127}$$

With decreasing $\tilde{\gamma}$, both interface width and line tension decrease, and the smaller line tension is less effective in counteracting the bending mismatch. This increases $l^*$ and makes the deformation from a sphere obvious, where $\phi > 0$ domains are flatter and the $\phi < 0$ domain is more curved, because the former has a greater bending modulus $\kappa$ than the latter. At point (IV) we have

$$\Gamma = 0.015\,\mathrm{pN} \tag{4.128}$$

$$d = 1.4\,\mu\mathrm{m}. \tag{4.129}$$

The line tension is still comparable to the simulation value, and the interface width shows a strong segregation between domains. The dominant $l^*$ increases as $\tilde{\gamma}$ decreases, and the modulated phase still has flatter $\phi > 0$ domains and more curved $\phi < 0$ domains.

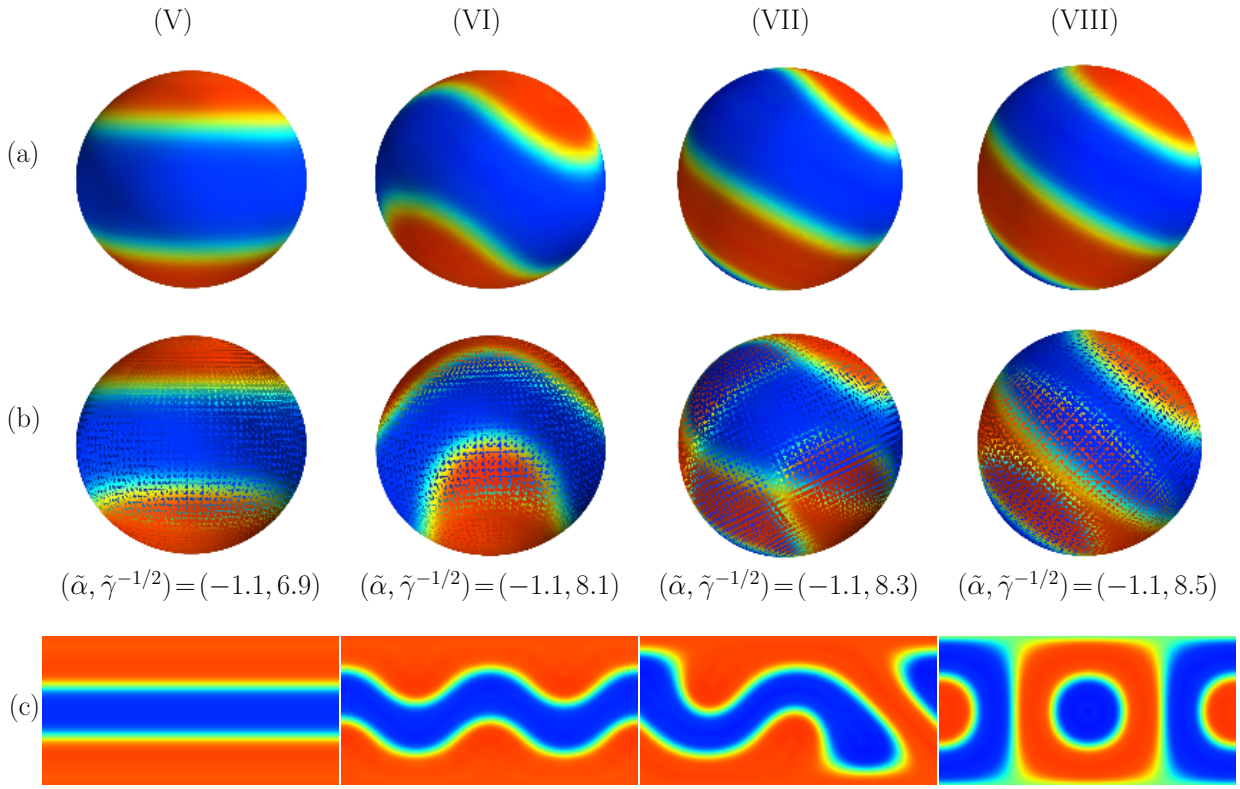


Figure 4.5: Example of lateral pattern change on the surface of a vesicle across the boundary between modulated phase regions $l^* = 2$ and $l^* = 3$, at points (V)–(VIII) in Figure 4.3 (b) with Gaussian bending. (V) is in the $l^* = 2$ region, and at (VI) the axisymmetric pattern is distorted with top and bottom domains elongated in perpendicular directions. At (VII) the domains of the same color ($\phi$) merge into a single spiral domain, which breaks up into multiple domains at (VIII), where $l^* = 3$ and the surface pattern is once again axisymmetric. In (a) are solid illustrations on vesicles, in (b) are the same patterns in transparent illustrations, and in (c) are two-dimensional plots of the same patterns of $\theta$ vs. $\varphi$. Shape deformations are shown with the surface order parameter distribution, which is scaled by the color bar in Figure 4.4.

The phase diagrams obtained from the non-axisymmetric full-mode method in Figure 4.3, however, also contain some special phase regions marked in purple. These are intermediate regions mainly at a boundary between two well-defined modulated phases, where surface patterns are mostly axisymmetric. Their distributions are irregular, but if we increase the resolution (decrease distance between two neighboring sampling points) of the diagrams, we could expect more sampling points near the boundaries to be in the intermediate phase and in such a purple region. Point (VII) from the right diagram of Figure 4.3 (b) with Gaussian bending gives an example of this intermediate phase, which shows a spiral pattern on the vesicular surface in Figure 4.5. At this point on the boundary between $l^* = 2$ and 3, there is only one domain of each color (red or blue, representing $\phi > 0$ and $\phi < 0$ respectively) in a spiral shape. To explore the cause of the "spiral" phase, we examine some other points (V), (VI) (in $l^* = 2$ region) and (VIII) ($l^* = 3$ region) near the boundary. The surface pattern at (V) is axisymmetric, and when $\tilde{\alpha}$ remains $-1.1$ and $\tilde{\gamma}^{-1/2}$ increases from 6.9 to 8.1 ($\tilde{\gamma}$ decreases), the pattern at (VI) is evidently no longer axisymmetric, though it still has two cap domains and one stripe domain and it is pinpointed in the $l^* = 2$ region. The top cap and the bottom cap are both elongated from the shape of a dome, but in perpendicular directions (in the transparent plot in Figure 4.5 (b), it is clear that the top domain is stretched in the plane of the paper and the bottom domain is stretched in the direction vertical to the paper), and the domain width decreases. Further increasing $\tilde{\gamma}^{-1/2}$ to 8.3, we have the distorted domains of the same order parameter merged into a single spiral at (VII), where the spiral width is similar to the distorted domain width at (VI). When $\tilde{\gamma}^{-1/2}$ is increased to 8.5, the surface pattern at (VIII) becomes once again axisymmetric, with a greater $l^* = 3$. There are now two cap domains and two stripe domains, which are smaller in size compared to those at (V). This is because they have a similar width as the spiral at (VII). In summary, if the system goes from $\tilde{\gamma}^{-1/2} = 6.9$ to 8.5, the originally axisymmetric domains are gradually distorted to have a narrower width, and then domains of the same order merge into a spiral, and finally the spiral is broken down into new axisymmetric domains, which are narrower than the original ones so one more domain can emerge and be accommodated on the vesicular

surface of the same size. In Figure 4.5 (a) are solid illustrations of the surface patterns, in (b) are their transparent illustrations, and in (c) are plots of the same patterns of polar angle $\theta$ vs. azimuthal angle $\varphi$ shown in a plane for a better demonstration of the domain shapes (especially the spiral).

Based on this work of a curvature-composition coupling system, we could expect more theoretical studies to come in the future. We could do some similar explorations like those of a spherical Landau-Ginzburg system in Chapters 2 and 3, including finite size effects, structure factor calculation and two- and three-dimensional phase behavior comparison. With the standard Landau-Ginzburg model and a positive interface line tension, the coupling model is more convincing and persuasive in interpreting and predicting modulated phases and other heterogeneities observed in microscopy or scattering experiments. One follow-up work that can be done right away is the Monte Carlo simulation of the coupling model. This would introduce thermal fluctuations at a finite temperature, and bring up the small heterogeneity of microemulsion state which is closely related to presumed lipid rafts. In a Monte Carlo simulation, potential first-order phase transitions and hysteresis in the system energy could also be probed. Both experimental and simulation observations could confirm the existence of the intermediate "spiral" phases, or rule them out as artifacts. In addition, we could have nonzero spontaneous curvature $H_{\mathrm{s}}$ in our model. The cause of nonzero spontaneous curvature, lipid bilayer asymmetry, is the subject of Chapter 5.

# Chapter 5

# MOLECULAR DYNAMICS MODELING OF ASYMMETRIC LIPID BILAYER IN SEARCH OF INDUCED PHASE SEPARATION

This chapter discusses the supplementary simulation study of compositionally asymmetric lipid bilayers, which make an appropriate system for molecular dynamics simulation. An asymmetric lipid-bilayer membrane is a more biologically relevant model of plasma membranes, which usually have unbalanced lipid types and compositions across the bilayer, giving rise to a spontaneous curvature. We focus on the inter-leaflet coupling. See Chapter 1 for experimental evidence of liquid-ordered (or liquid-disordered) domains from both leaflets being in registration, which might be caused by the coupling. In a bilayer consisting of a naturally non-phase-separating leaflet and a phase-separating leaflet by itself, the latter may induce a phase separation tendency in the former through the inter-leaflet coupling interaction. In a small-sized membrane patch, however, the finite size effect may overcome the inter-leaflet coupling and make domains in anti-registration. In this study, we use coarse-grained models of both symmetric and asymmetric bilayers, in small or large sizes, to investigate the coupling and finite size effect in molecular dynamics simulation.

## *5.1 Research background of ternay asymmetric lipid bilayers*

We study a commonly used ternary lipid system consisting of DPPC (dipalmitoylphosphatidylcholine or di-16:0 PC, the high-melting temperature lipid), DIPC (dilinoleoylphosphatidylcholine or di-18:2 PC, the low-melting temperature lipid), and cholesterol. This selection of lipid molecules could reduce domain anti-registration caused by the hydrophobic thickness mismatch between liquid-ordered and liquid-disordered domains[102], because the

tails of DPPC and DIPC have similar number of carbon atoms and similar length, and are each represented by four beads in the coarse-grained model. Besides interactions between DPPC lipid tails and between DIPC lipid tails from the opposing leaflets, the cholesterol molecules, which flip-flop between both leaflets, are helpful for the inter-leaflet coupling and domain registration to happen.

If there are equal amounts of DPPC, DIPC and cholesterol molecules (each 33.3% of the total number of lipids) in each leaflet, the system phase separates at room temperature, which is lower than its phase separation temperature. If we keep the cholesterol molecule number at 33.3% of total lipid number, and decrease the amount of DPPC and increase the amount of DIPC, the system would be outside the phase separation region and would not phase separate even at a low temperature. This is similar to an experimental ternary lipid system composed of DPPC, cholesterol and the low-melting temperature lipid DiPhyPC (di-4ME-16:0), which has four methyl groups attached to each tail.[104] Such a system (a monolayer or a symmetric bilayer) phase separates at equal amounts of DiPhyPC, DPPC and cholesterol, and stays in a homogeneous phase if the percent amounts of the three species are 61.3%, 5.3% and 33.3% respectively. If the percent amounts of DiPhyPC, DPPC and cholesterol are 53.3%, 13.3% and 33.3% respectively, the system is right on the verge of the phase separation region, showing a slight phase separation at room temperature.

The experimental work[104] suggests that when the phase-separating and the homogeneous monolayers are put together forming an asymmetric bilayer, the phase-separating leaflet would force the homogeneous leaflet to also phase separate, and the resulting liquid-ordered domains from the opposing leaflets would be in registration. Through similar inter-leaflet coupling, the homogeneous monolayer would prohibit the slightly phase-separating monolayer from phase separation when they are put together. The induced phase separation is the focal point of our simulation study, though we use DIPC instead of DiPhyPC. We prepare coarse-grained models of three leaflets, A, B and C, according to the same percent amounts in Reference [104]. In the non-phase-separating leaflet A, 61.3% of all molecules are DIPC, 5.3% are DPPC, and 33.3% are cholesterol. In the phase-separating leaflet B, there

are equal amounts of DIPC, DPPC and cholesterol (each 33.3% of all molecules). In leaflet C, which is near the boundary of the phase coexistence region, 53.3% of all molecules are DIPC, 13.3% are DPPC, and 33.3% are cholesterol. We then build symmetric bilayers using two identical leaflets and asymmetric bilayers using two different leaflets.

## *5.2 Simulation system and modeling*

### *5.2.1 Molecular dynamics simulation*

We build models of lipid bilayers in the Martini Bilayer Maker of the CHARMM-GUI web system, using the coarse-grained force field Martini 2.2[120], with explicit water solvent layers of a thickness of 2.25 nm both above and below the lipid bilayer. We run molecular dynamics simulations in GROMACS 5.1.4[121]. Alternative force fields are also available[119], including all atom, united atom, and implicit solvent coarse-grained force fields such as dry Martini[122] and even more coarse-grained models which are able to simulate a whole lipid vesicle[81, 123, 124, 125], but they are not in use here. The choice of Martini force field would be a right balance between speed and accuracy for this application.

We use two different sizes of leaflets and bilayers which are square patches in the simulation with periodic boundary condition. We design the leaflets including the following numbers of lipid molecules:

| Leaflet | DIPC | DPPC | Cholesterol |
|---|---|---|---|
| Small A (no phase separation) | 184 | 16 | 100 |
| Small B (phase separation) | 100 | 100 | 100 |
| Small C (on the verge) | 160 | 40 | 100 |
| Large A (no phase separation) | 613 | 53 | 333 |
| Large B (phase separation) | 333 | 333 | 333 |
| Large C (on the verge) | 533 | 133 | 333 |

The small leaflet patch has 300 lipids in total and the simulation box edge length is about 12 nm, so a small-sized bilayer has a total of 600 lipids. The large leaflet patch has 999

lipids with a simulation box edge length of about 22 nm, so a large-sized bilayer has 1998 lipid molecules. Putting two leaflets of the same size together, we have six combinations: symmetric bilayers A/A, B/B and C/C, and asymmetric bilayers A/C, A/B and C/B. With small and large sizes, we run simulations of 12 different bilayer systems in total.

We run simulations in the NPT ensemble, and the dynamics integration time step is 20 fs. Right before the production simulation step, there is an equilibration step for 400 ns at temperature 400 K, which is above the phase separation temperature. Therefore the system is homogeneous and the lipid molecules are fully mixed. In the production step, the simulation lasts for 10 µs at temperature 300 K, and the system should be brought to a stable state according to the observations in Reference [102] which uses similar systems and parameters. We record simulation snapshots along the process, making sure the system is in an equilibrium state, and calculate intra- and inter-leaflet pair correlation functions using these snapshots. For both non-phase-separating and phase-separating systems, the pair correlation functions would show some typical features, which correspond to the observations of the snapshots. For a non-phase-separating system showing some trend of phase separation, such as leaflet C on the verge of phase separation, we build idealized bilayer models in the Python programming language to give a possible explanation of its pair correlation function.

### *5.2.2 Idealized bilayer model*

The idealized bilayer model consists of two species, representing DIPC and DPPC. In each leaflet, the range of one or more domains is manually adjusted. Inside the domain range is assigned to the "liquid-ordered" phase and outside is for the "liquid-disordered" phase. In each phase, DIPC and DPPC molecules are uniformly distributed according to their different densities, which are also manually selected. The DIPC density inside the domain range is different from that outside, and the same holds for the DPPC density. The size of an idealized model membrane is set to be approximately the same as a simulation membrane (12 nm for small membrane and 22 nm for large membrane), and the number of DIPC (also number of DPPC) molecules in an idealized model leaflet is equal to that in the corresponding

simulation leaflet. If in a simulation leaflet of edge length $L$, the number of DIPC molecules is $N_{\mathrm{DIPC}}$ and that of DPPC is $N_{\mathrm{DPPC}}$, we have the following constraints on the area $A^{(\mathrm{lo})}$ of the "liquid-ordered" phase, the area $A^{(\mathrm{ld})}$ of the "liquid-disordered" phase, the density $\rho^{(\mathrm{lo})}_{\mathrm{DIPC}}$ of DIPC molecules in the "liquid-ordered" phase, the density $\rho^{(\mathrm{ld})}_{\mathrm{DIPC}}$ of DIPC outside the "liquid-ordered" phase (in the "liquid-disordered" phase), and densities $\rho^{(\mathrm{lo})}_{\mathrm{DPPC}}$ and $\rho^{(\mathrm{ld})}_{\mathrm{DPPC}}$ of DPPC inside and outside the "liquid-ordered" phase:

$$A^{(\mathrm{lo})} + A^{(\mathrm{ld})} = L^2 \tag{5.1}$$

$$\rho^{(\mathrm{lo})}_{\mathrm{DIPC}} A^{(\mathrm{lo})} + \rho^{(\mathrm{ld})}_{\mathrm{DIPC}} A^{(\mathrm{ld})} = N_{\mathrm{DIPC}} \tag{5.2}$$

$$\rho^{(\mathrm{lo})}_{\mathrm{DPPC}} A^{(\mathrm{lo})} + \rho^{(\mathrm{ld})}_{\mathrm{DPPC}} A^{(\mathrm{ld})} = N_{\mathrm{DPPC}} \tag{5.3}$$

where we use the same $L$, $N_{\mathrm{DIPC}}$ and $N_{\mathrm{DPPC}}$ from the simulation, and we can manually adjust $A^{(\mathrm{lo})}$, $\rho^{(\mathrm{lo})}_{\mathrm{DIPC}}$ and $\rho^{(\mathrm{lo})}_{\mathrm{DPPC}}$ independently to create the idealized model leaflet. We put two such leaflets together to form a bilayer. We can make multiple bilayers of the same model with manually designed lipid composition and distribution, and calculate the intra- and inter-leaflet pair correlation functions of the model from these many bilayers generated independently. In fact, for each of the 12 different bilayer systems in simulation, either symmetric or asymmetric, we can design an idealized bilayer to model it. For a small-sized system (600 lipids), we make 500 bilayers, and for a large-sized system (1998 lipids) we make 100 bilayers for the pair correlation function calculation. The correlations calculated from the idealized bilayer model system can be compared with those calculated from simulation snapshots. If the idealized model is able to reproduce the same features observed in simulation correlations, the manually designed lipid distribution of the model is a possible explanation of the corresponding simulation results.

### *5.3 Results and discussion*

The final simulation snapshots of small A, B and C leaflets in their symmetric bilayers are included in Figure 5.1. DPPC molecules are marked by grey color, DIPC molecules are

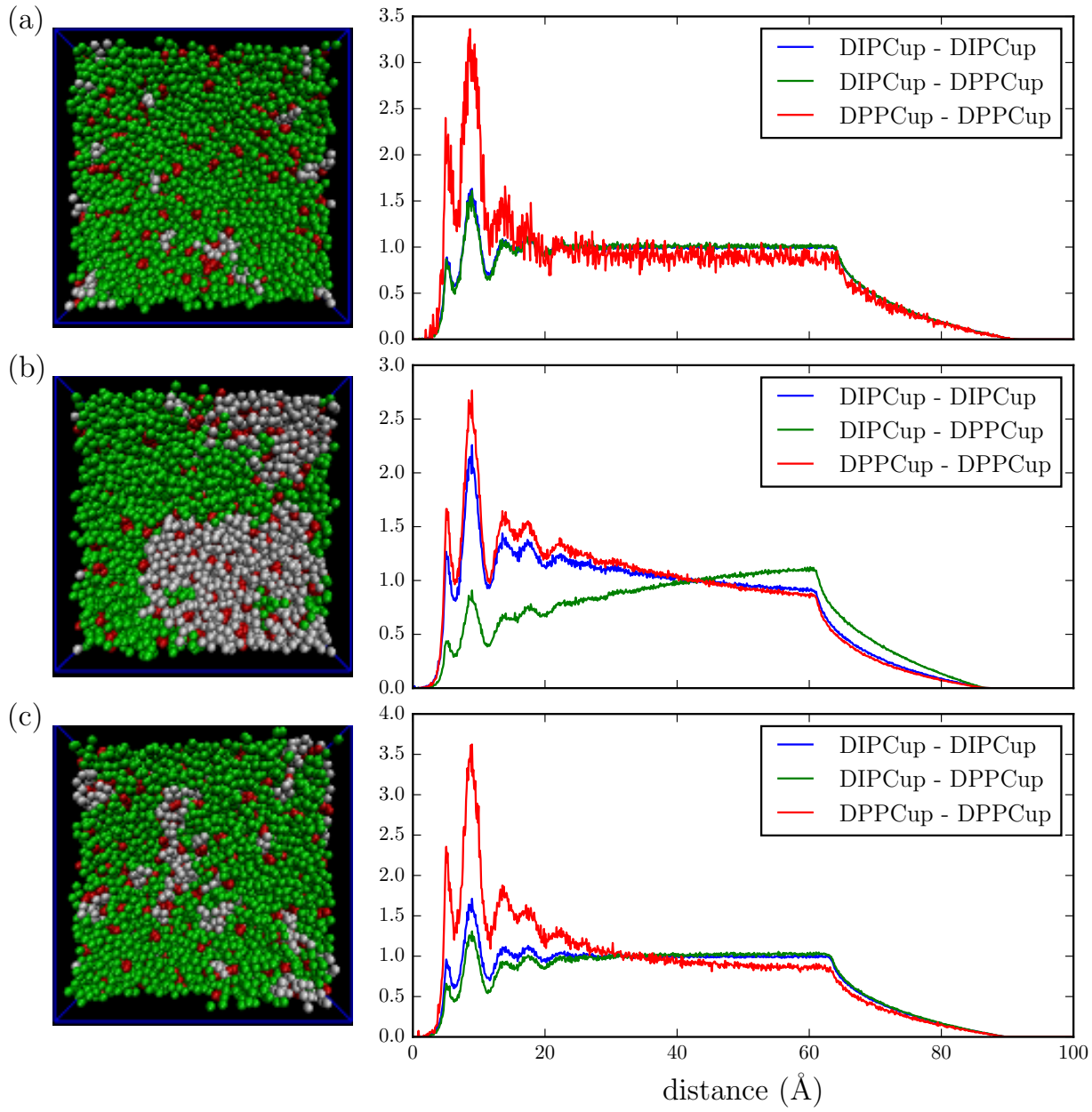


Figure 5.1: Simulation snapshots and intra-leaflet pair correlation functions of small leaflets A, B and C in their respective symmetric bilayers (A/A, B/B and C/C) where the upper and lower leaflets behave similarly. A does not phase separate, B shows a phase separation, and C possibly shows multiple small transient DPPC clusters. DIPC: green; DPPC: grey; cholesterol: red.

green, and cholesterols are red. It is visually observable that leaflet A stays in a homogenous phase, leaflet B phase separates into a liquid-ordered phase (made by DPPC and cholesterol) and a liquid-disordered phase (made by DIPC), and leaflet C does not phase separate, but it is likely that there are multiple small clusters of DPPC molecules surrounded by a sea of DIPC. The simulation trajectory of leaflet C shows that these possible clusters are transient and their locations and sizes fluctuate all the time. The leaflets A, B and C show similar surface configurations either in symmetric bilayers (A/A, B/B and C/C) or in asymmetric bilayers (A/C, A/B and C/B), regardless of system size, and this is why we resort to pair correlation function calculations to distinguish the possible phase-separation-inducing effects of leaflet B on leaflets A and C in asymmetric bilayers.

Beside each snapshot are the intra-leaflet pair correlation functions within the upper leaflet. The surface configuration and intra-leaflet correlations of the lower leaflet are similar to the upper. Because of the rapid flip-flop of cholesterol molecules across the bilayers, correlations involving cholesterol are not studied here. All intra- and inter-leaflet pair correlation functions are plotted against distance (in Å) parallel to the membrane plane. Signals attenuate at half the simulation box edge length (about 6 nm for small systems and 11 nm for large systems), leading to the drop-off artifacts. In Figure 5.1, the intra-leaflet correlation functions quickly converge to 1 in a system of no phase separation (leaflet A), and in a phase-separated system (leaflet B) they enter a monotonically decreasing shape (between same species) or a monotonically increasing shape (between different species). These match the observations in snapshots. The correlations within leaflet C resemble those of leaflet A, because they both show no phase separation. The peaks at short distances in these plots are characteristic of a liquid system, but are not captured by the idealized bilayer model.

### *5.3.1 Inter-leaflet correlations in a symmetric bilayer*

It is the inter-leaflet pair correlation functions that show special features characterizing the inter-leaflet coupling. In Figure 5.2, the inter-leaflet correlations of either small or large symmetric A/A bilayers also quickly converge to 1. In Figure 5.3, while the small symmetric B/B

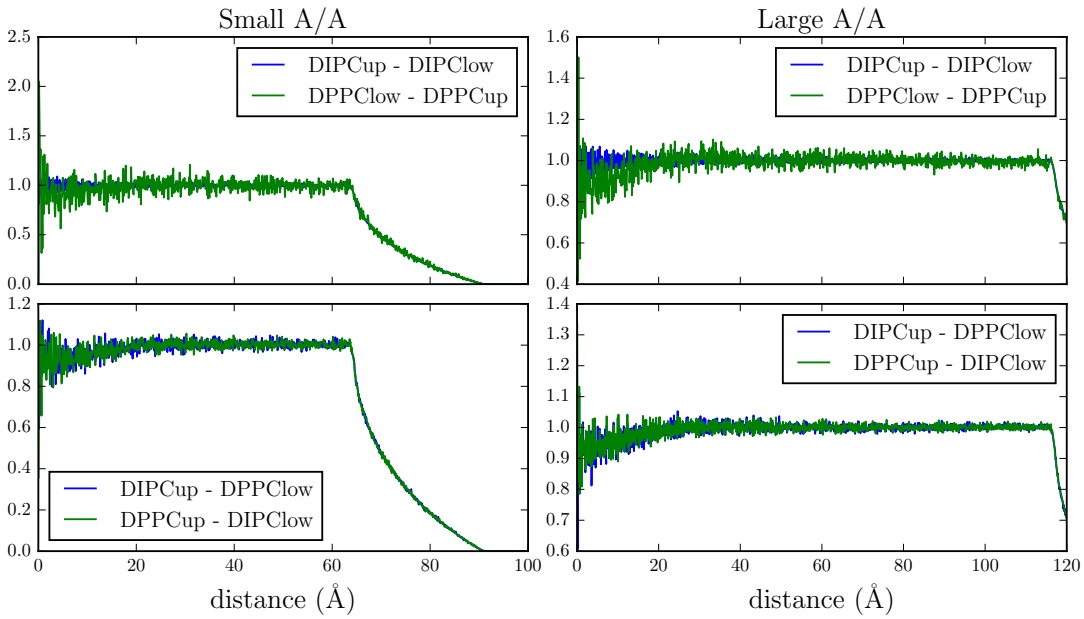


Figure 5.2: Inter-leaflet pair correlation functions of symmetric A/A bilayers

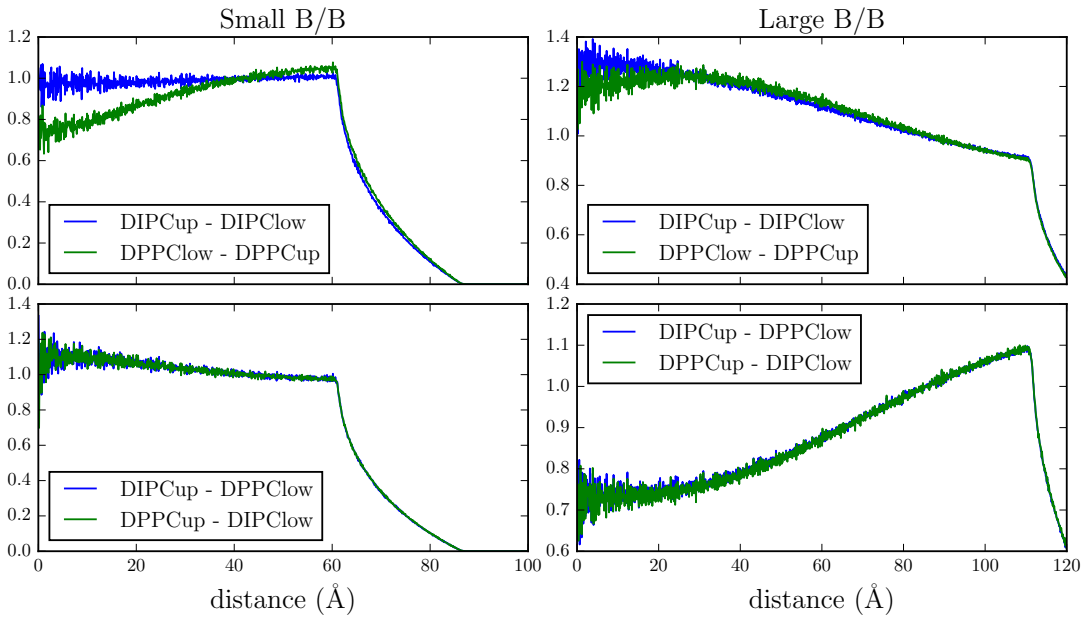


Figure 5.3: Inter-leaflet pair correlation functions of symmetric B/B bilayers

bilayer shows typical inter-leaflet correlations of domains in anti-registration, the large B/B bilayer shows typical correlation signals of domains in registration. A good interpretation of these correlations is given by the idealized bilayer models in Figure 5.4. In both small and large B/B models, there is one circular "liquid-ordered" domain in each leaflet. In the small model, domains are in anti-registration; in the large model, domains are in registration. The idealized models are designed according to the following table:

| Property | Small B/B bilayer | Large B/B bilayer |
|---|---|---|
| $\rho^{(\mathrm{lo})}_{\mathrm{DIPC}}$ ($\mathrm{nm}^{-2}$) | 0.1 | 0.1 |
| $\rho^{(\mathrm{lo})}_{\mathrm{DPPC}}$ ($\mathrm{nm}^{-2}$) | 1.85 | 1.276 |
| $\rho^{(\mathrm{ld})}_{\mathrm{DIPC}}$ ($\mathrm{nm}^{-2}$) | 1.0 | 1.276 |
| $\rho^{(\mathrm{ld})}_{\mathrm{DPPC}}$ ($\mathrm{nm}^{-2}$) | 0.1 | 0.1 |
| Domain number | 1 in each leaflet | 1 in each leaflet |
| Domain radius (nm) | 3.945 | 8.777 |
| Domain location in each leaflet | Upper: at center; lower: half box length from center | Upper and lower: at center |

In Figure 5.4, both the anti-registration configuration of the small model and the in-registration configuration of the big model give rise to the corresponding inter-leaflet correlations in Figure 5.3 of small or large bilayer. These observations suggest that at small membrane size, a phase-separating lipid bilayer may be in an anti-registration configuration, and if the system size is increased, the bilayer may change into an in-registration configuration, in agreement with the conclusion of Reference [103], which attributes the anti-registration caused by finite size to the slight hydrophobic mismatch between DIPC and DPPC tails.

Similarly, the inter-leaflet correlations in small and large symmetric C/C bilayers in Figure 5.5 are modeled by idealized bilayer models in Figure 5.6. In either small or large C/C idealized bilayer model, each leaflet has two "liquid-ordered" round domains. In the upper leaflet, one domain is fixed at the center and the other is randomly located, and in the lower leaflet, one domain is fixed at a distance from the center, and the other is randomly situated. The idealized models are designed according to the table:

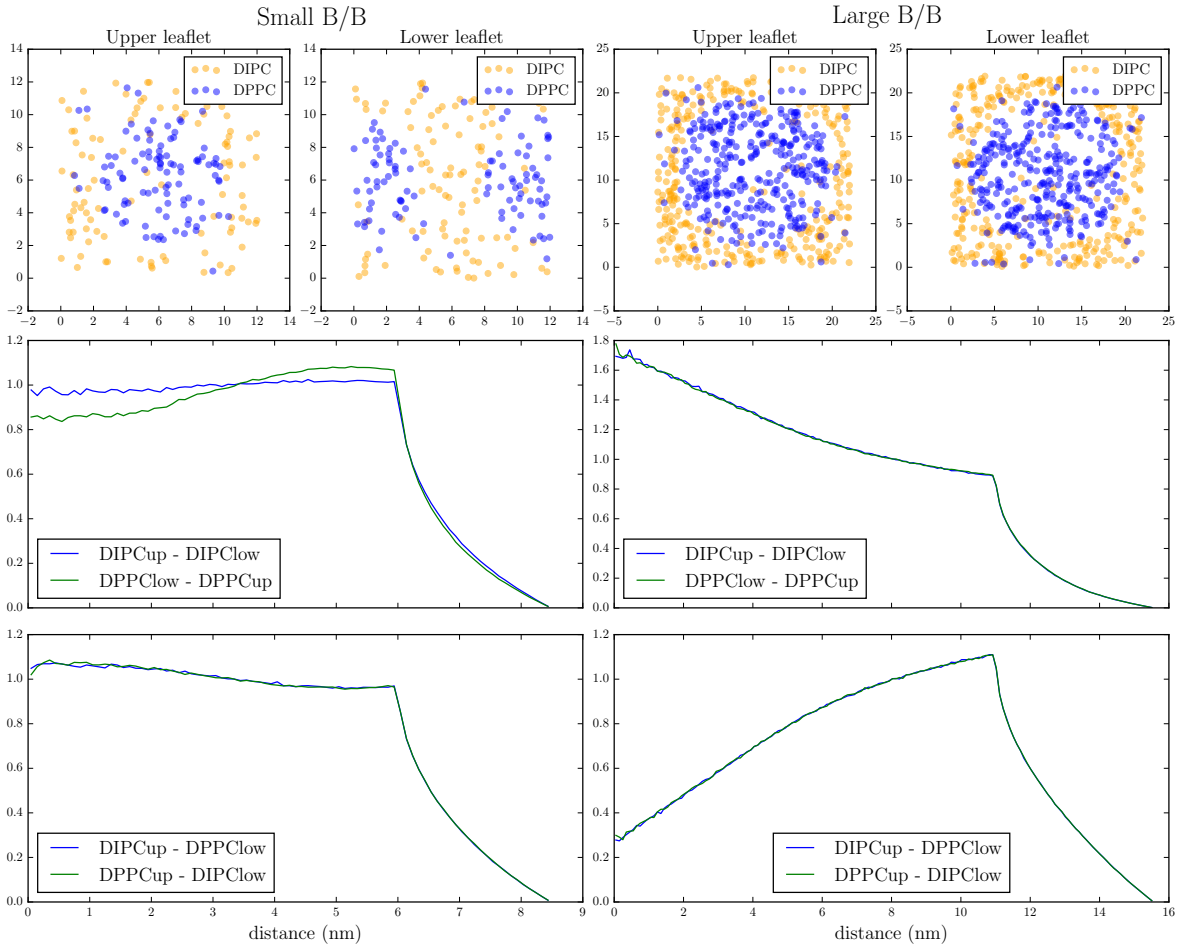


Figure 5.4: Idealized bilayer model configurations and inter-leaflet pair correlation functions of symmetric B/B bilayers; membrane sizes in nm

| Property | Small C/C bilayer | Large C/C bilayer |
|---|---|---|
| $\rho^{(\mathrm{lo})}_{\mathrm{DIPC}}$ ($\mathrm{nm}^{-2}$) | 0.3 | 0.3 |
| $\rho^{(\mathrm{lo})}_{\mathrm{DPPC}}$ ($\mathrm{nm}^{-2}$) | 1.04 | 1.216 |
| $\rho^{(\mathrm{ld})}_{\mathrm{DIPC}}$ ($\mathrm{nm}^{-2}$) | 1.3 | 1.25 |
| $\rho^{(\mathrm{ld})}_{\mathrm{DPPC}}$ ($\mathrm{nm}^{-2}$) | 0.1 | 0.1 |
| Domain number | 2 in each leaflet | 2 in each leaflet |
| Domain radius (nm) | 2.08 | 3.473 |
| Domain location in upper leaflet | One at center, one randomly positioned | One at center, one randomly positioned |
| Domain location in lower leaflet | One 28.5% of box length from center, one randomly positioned | One 25% of box length from center, one randomly positioned |

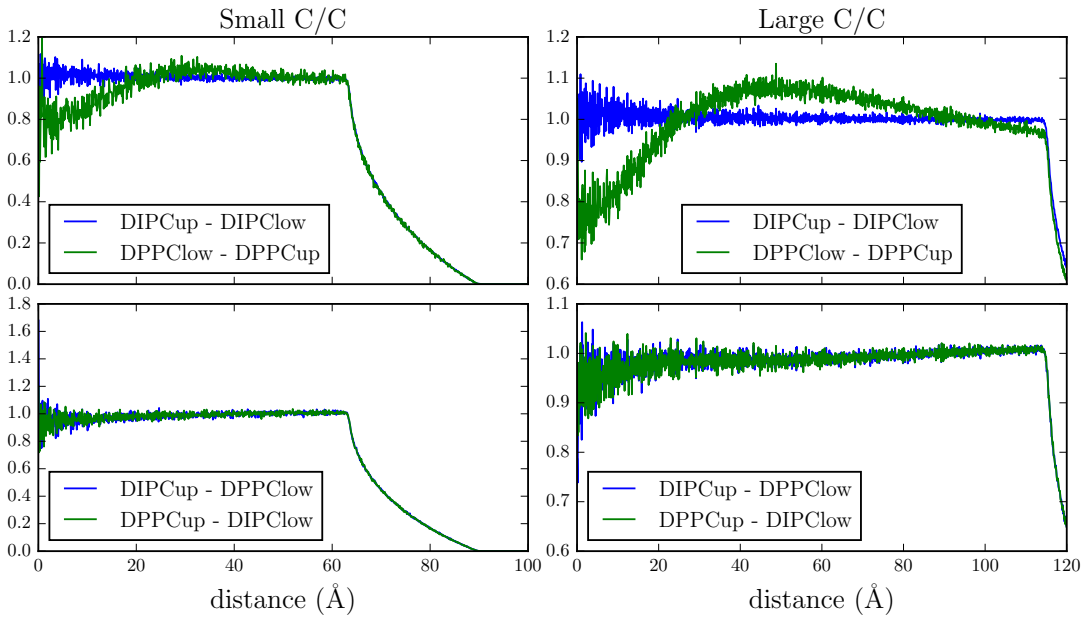


Figure 5.5: Inter-leaflet pair correlation functions of symmetric C/C bilayers

This agrees with the observation of DPPC clusters and no real phase separation. The phase behavior of clustering is similar in both small and large C/C models, and appears insensitive to system size, which may be because of the absence of large-scale phase separation. In fact, no finite size effect is observed by comparing small and large systems, except in B/B bilayers.

### *5.3.2 Inter-leaflet correlations in an asymmetric bilayer*

For asymmetric bilayers, the inter-leaflet correlations in small and large A/C bilayers (Figure 5.7) are qualitatively similar to those in symmetric C/C bilayers (Figure 5.5). Similarly, correlations in small and large A/B bilayers (Figure 5.8) are qualitatively similar to those in asymmetric C/B bilayers (Figure 5.9). This suggests that leaflet A behaves in a similar way to leaflet C, when leaflet A is present in an asymmetric bilayer, where small transient DPPC clusters are possibly formed in leaflet A.

The inter-leaflet correlations in small and large asymmetric C/B bilayers in Figure 5.9 are modeled by idealized bilayer membranes in Figure 5.10. In either small or large C/B

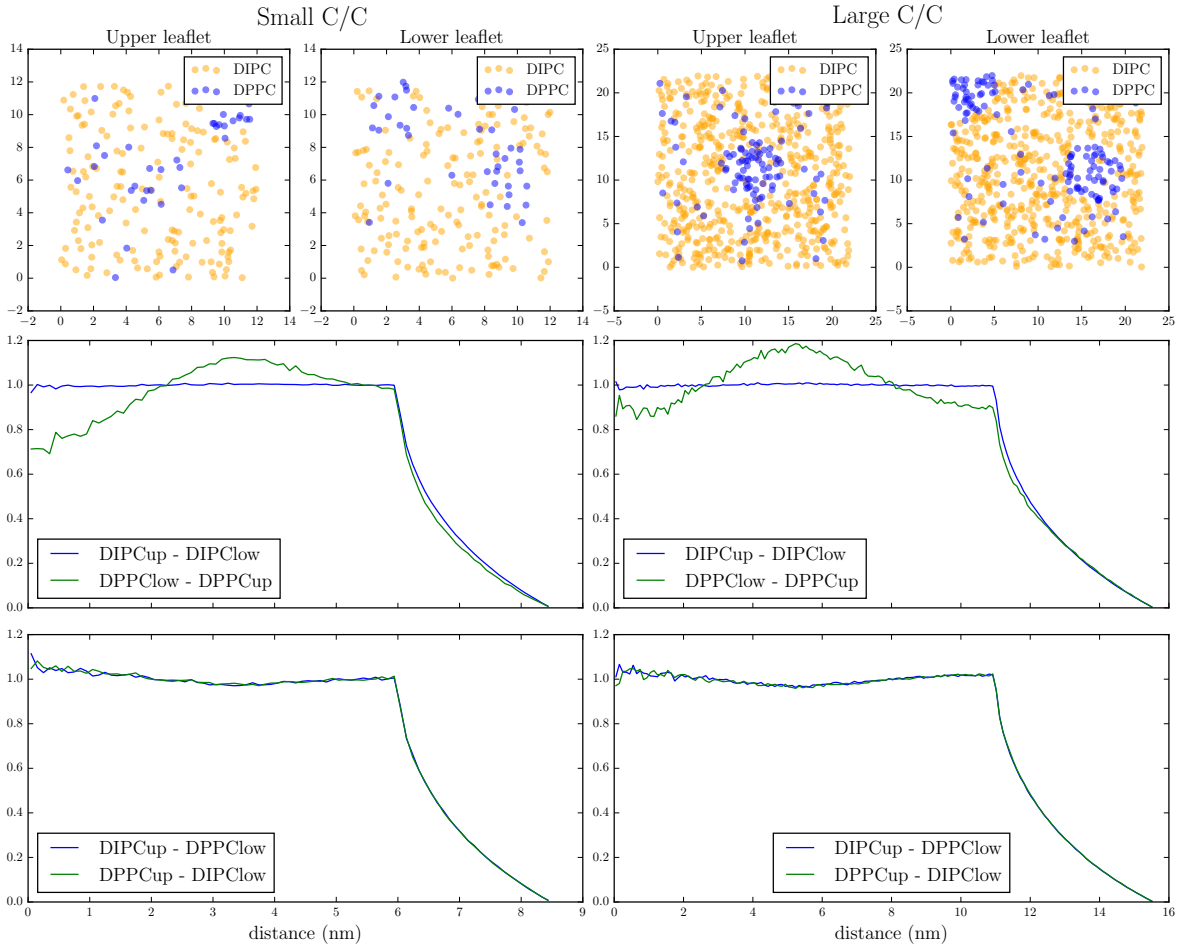


Figure 5.6: Idealized bilayer model configurations and inter-leaflet pair correlation functions of symmetric C/C bilayers; membrane sizes in nm

idealized bilayer model, the lower leaflet B has one domain similar to that in a symmetric B/B bilayer, but the domain is at a distance from the center. The upper leaflet C, on the other hand, has a 50% chance to be in a single-domain configuration, and a 50% chance to be in a two-domain configuration. In the single-domain configuration, the domain is fixed at the center; in the two-domain configuration, one domain is fixed at the center and the other domain is randomly positioned. The idealized leaflets are designed according to:

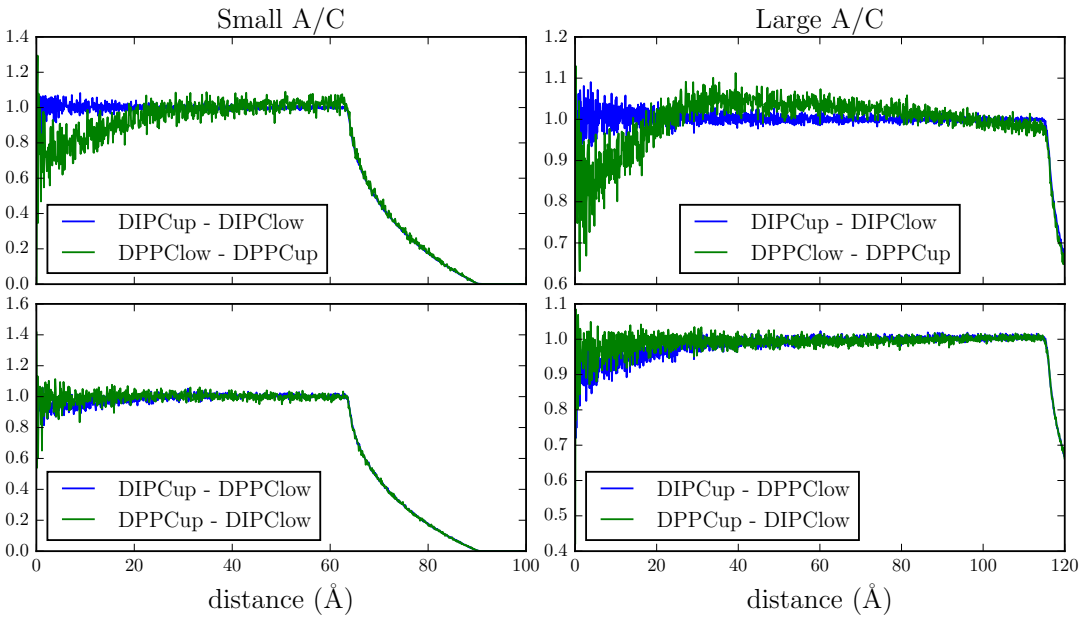


Figure 5.7: Inter-leaflet pair correlation functions of asymmetric A/C bilayers

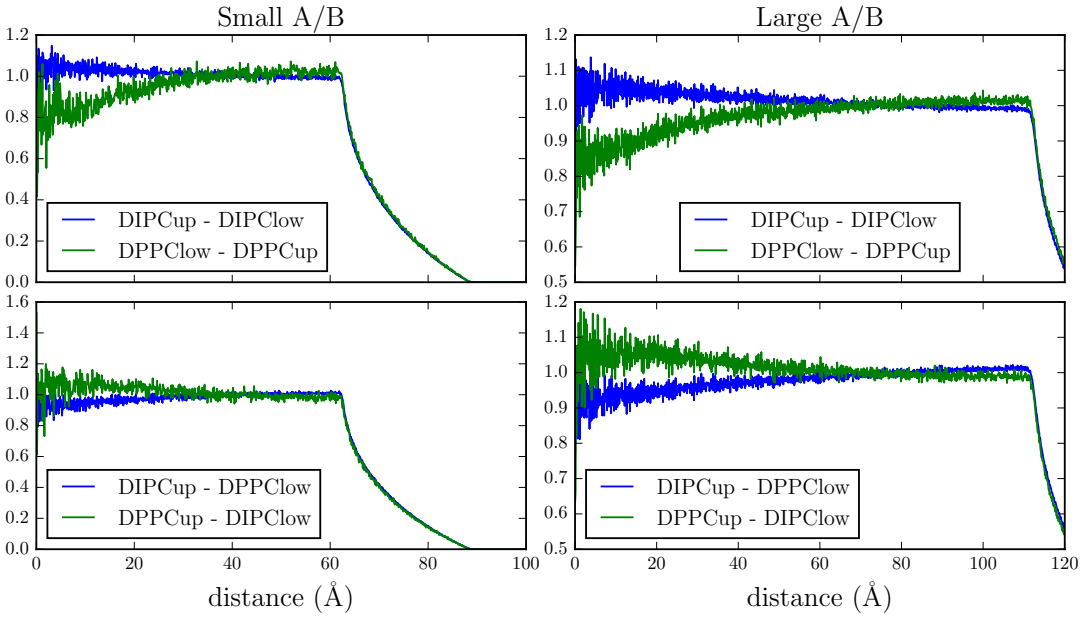


Figure 5.8: Inter-leaflet pair correlation functions of asymmetric A/B bilayers

| Property | Small C leaflet in C/B bilayer | Small B leaflet in C/B bilayer |
|---|---|---|
| $\rho^{(\mathrm{lo})}_{\mathrm{DIPC}}$ ($\mathrm{nm}^{-2}$) | 0.3 | 0.1 |
| $\rho^{(\mathrm{lo})}_{\mathrm{DPPC}}$ ($\mathrm{nm}^{-2}$) | 1.316 | 1.85 |
| $\rho^{(\mathrm{ld})}_{\mathrm{DIPC}}$ ($\mathrm{nm}^{-2}$) | 1.25 | 1.0 |
| $\rho^{(\mathrm{ld})}_{\mathrm{DPPC}}$ ($\mathrm{nm}^{-2}$) | 0.1 | 0.1 |
| Domain number | 1 (50% chance) or 2 (50% chance) | 1 |
| Domain radius (nm) | 2.59 (1-domain) or 1.83 (2-domain) | 3.945 |
| Domain location | At center (1-domain) or one at center, one randomly positioned (2-domain) | 40% of box length from center |

| Property | Large C leaflet in C/B bilayer | Large B leaflet in C/B bilayer |
|---|---|---|
| $\rho^{(\mathrm{lo})}_{\mathrm{DIPC}}$ ($\mathrm{nm}^{-2}$) | 0.3 | 0.1 |
| $\rho^{(\mathrm{lo})}_{\mathrm{DPPC}}$ ($\mathrm{nm}^{-2}$) | 1.22 | 1.8 |
| $\rho^{(\mathrm{ld})}_{\mathrm{DIPC}}$ ($\mathrm{nm}^{-2}$) | 1.25 | 1.0 |
| $\rho^{(\mathrm{ld})}_{\mathrm{DPPC}}$ ($\mathrm{nm}^{-2}$) | 0.1 | 0.1 |
| Domain number | 1 (50% chance) or 2 (50% chance) | 1 |
| Domain radius (nm) | 4.9 (1-domain) or 3.46 (2-domain) | 7.3 |
| Domain location | At center (1-domain) or one at center, one randomly positioned (2-domain) | 40% of box length from center |

When compared with the symmetric C/C systems, it is likely that the leaflet C in both small and large asymmetric C/B systems has a tendency to combine all small DPPC domains and bring about a real phase separation, which is induced by leaflet B through the inter-leaflet coupling.

In summary, the asymmetric lipid bilayers simulated in coarse-grained molecular dynamics have not reproduced the induced phase separations that are visually obvious in leaflet A or C by leaflet B, as observed in experiments. This may be related to the limited number of lipid molecules used, as no phase separation would happen if there are not enough molecules in a coarse-grained simulation.[31] The finite size effect is observed in the phase-separating

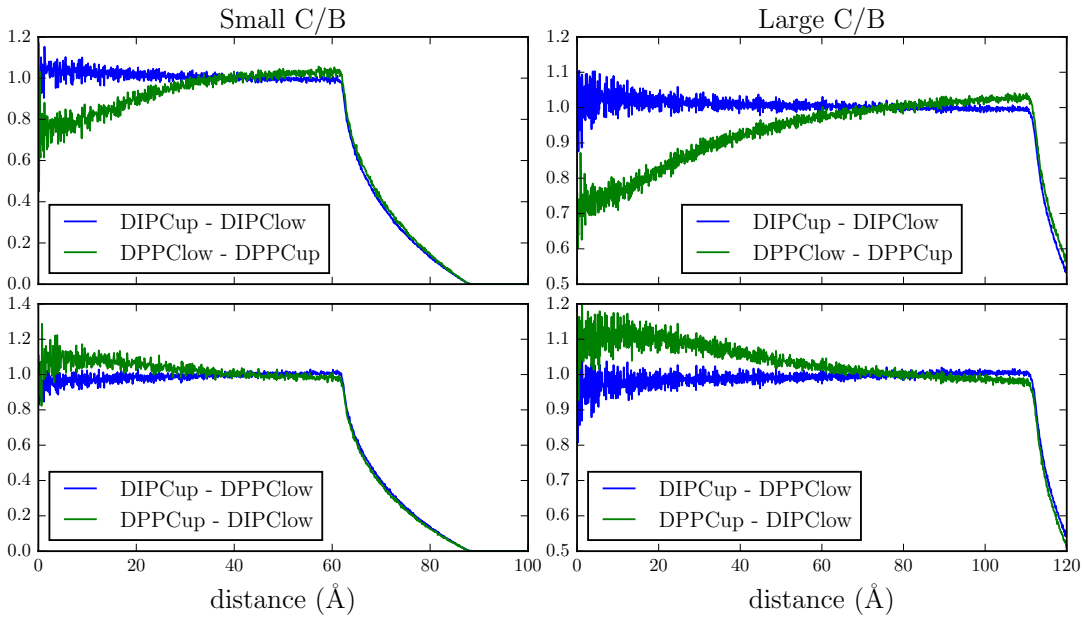


Figure 5.9: Inter-leaflet pair correlation functions of asymmetric C/B bilayers

B/B bilayer, which has domains in registration at a large size and in anti-registration at a small size. However, an inclination to phase separate in leaflet A or C is reflected by the inter-leaflet pair correlation functions of A/B and C/B bilayers. The leaflet A would behave similarly to C, forming multiple small DPPC clusters, and the leaflet C would tend to phase separate by combining the small DPPC clusters into a single domain. The changes in leaflets A and C possibly indicate an inter-leaflet coupling and a phase-separation-inducing effect of leaflet B. The idealized bilayer models illustrate possible lipid distributions and configurations of the bilayers. The details in the modeling results, including density variations of different lipid species and the relative locations of domains in different leaflets, demand further explanations of the physical mechanism. To further confirm the findings of this work, we not only need more molecular dynamics simulations to assure the equilibration of the system, but also need to seek answers to the detailed physical mechanism.

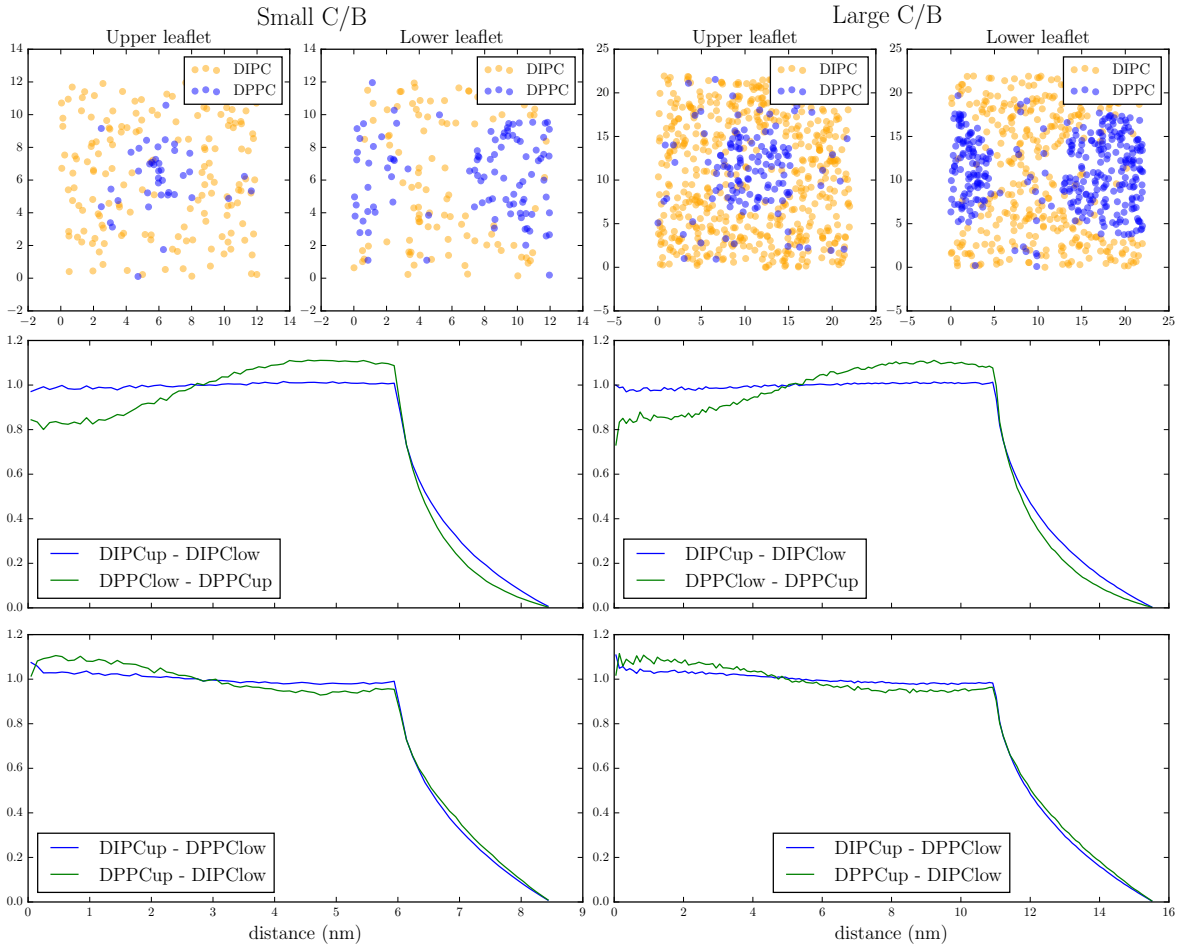


Figure 5.10: Idealized bilayer model configurations and inter-leaflet pair correlation functions of asymmetric C/B bilayers; membrane sizes in nm

## *5.4 Appendix*

The appendix contains intra-leaflet pair correlation functions from both simulations and idealized bilayer modeling.

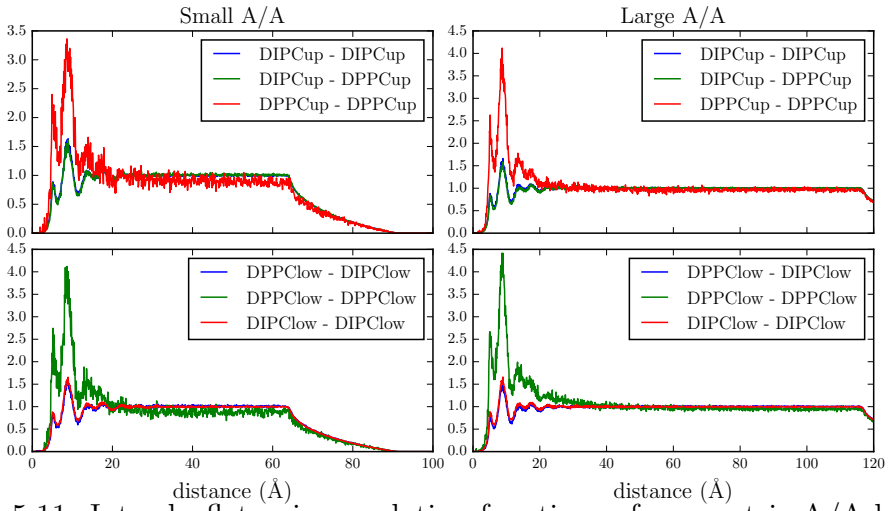


Figure 5.11: Intra-leaflet pair correlation functions of symmetric A/A bilayers

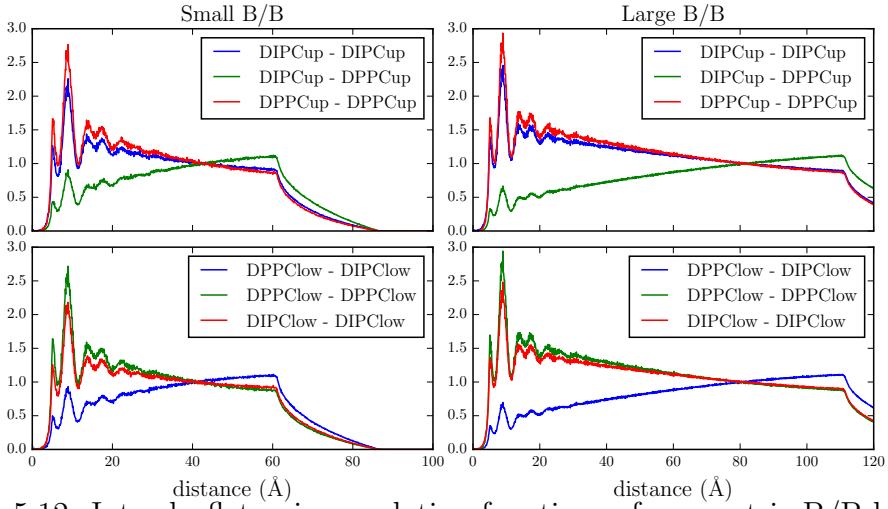


Figure 5.12: Intra-leaflet pair correlation functions of symmetric B/B bilayers

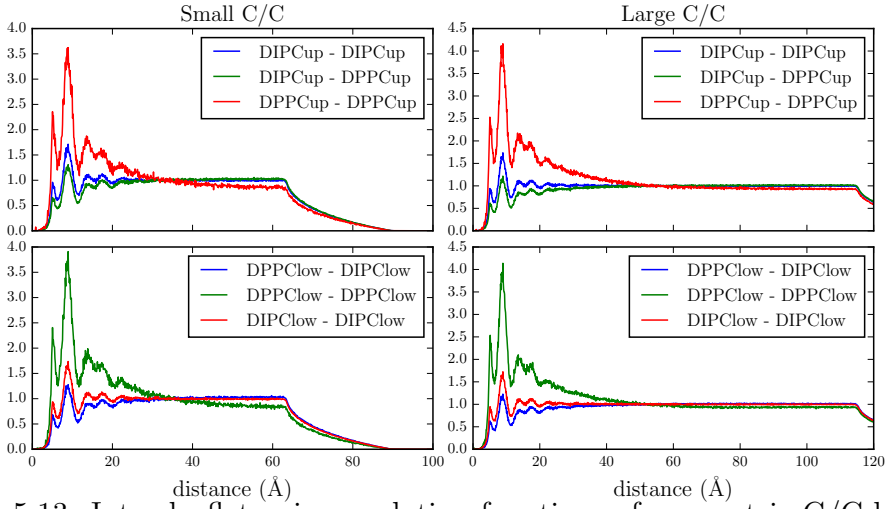


Figure 5.13: Intra-leaflet pair correlation functions of symmetric C/C bilayers

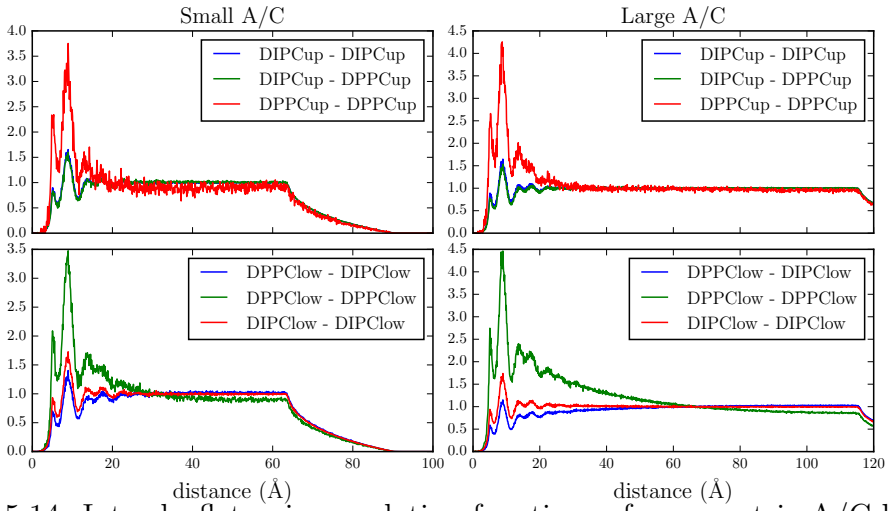


Figure 5.14: Intra-leaflet pair correlation functions of asymmetric A/C bilayers

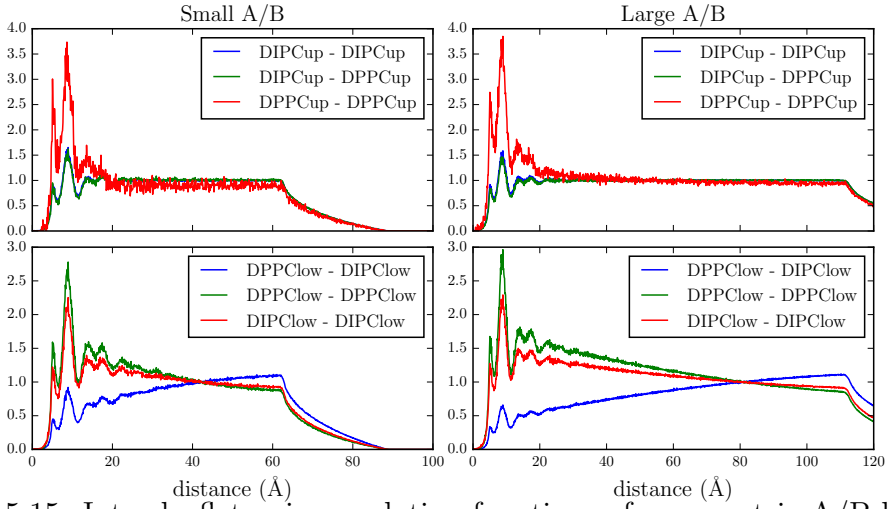


Figure 5.15: Intra-leaflet pair correlation functions of asymmetric A/B bilayers

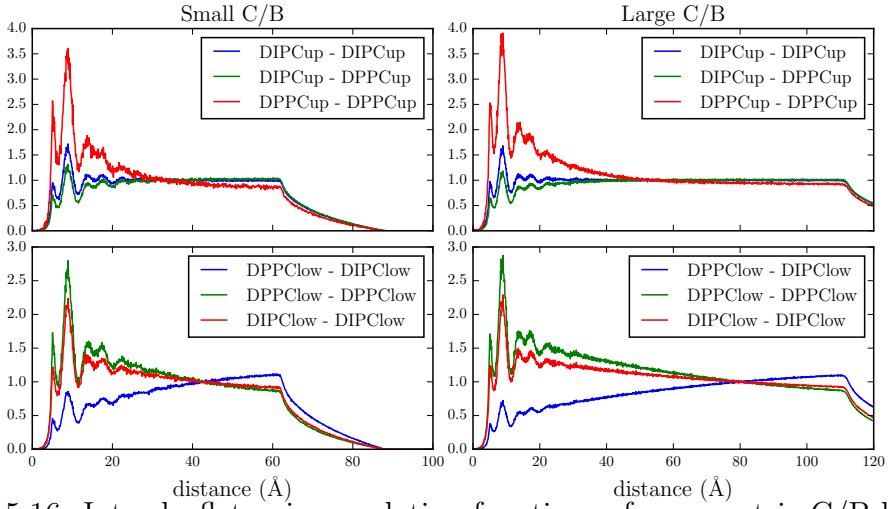


Figure 5.16: Intra-leaflet pair correlation functions of asymmetric C/B bilayers

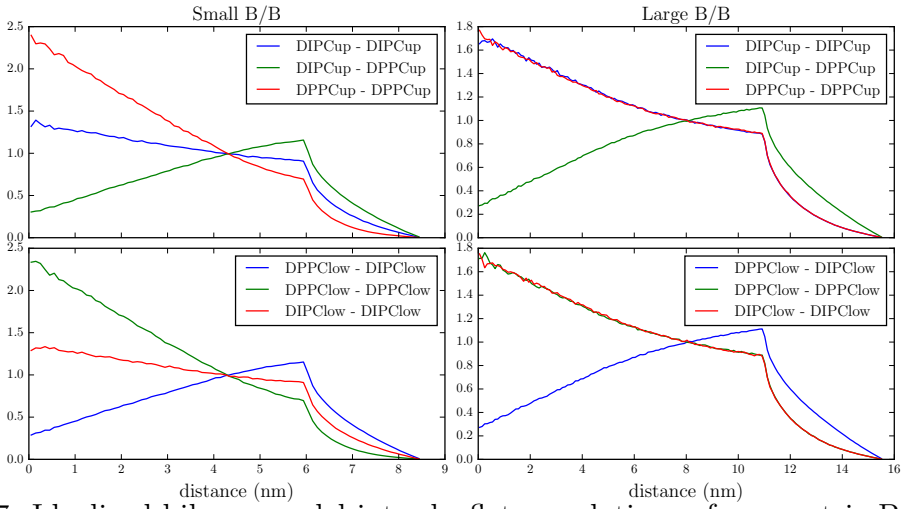


Figure 5.17: Idealized bilayer model inter-leaflet correlations of symmetric B/B bilayers

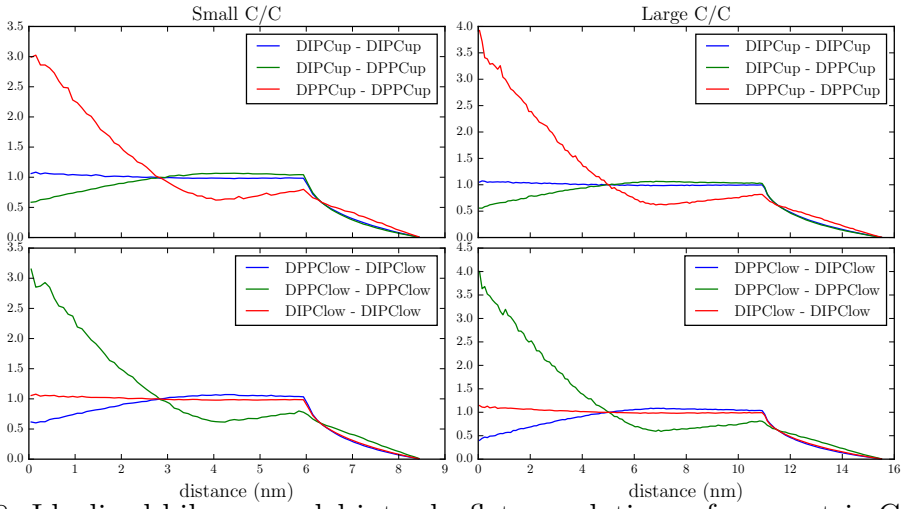


Figure 5.18: Idealized bilayer model inter-leaflet correlations of symmetric C/C bilayers

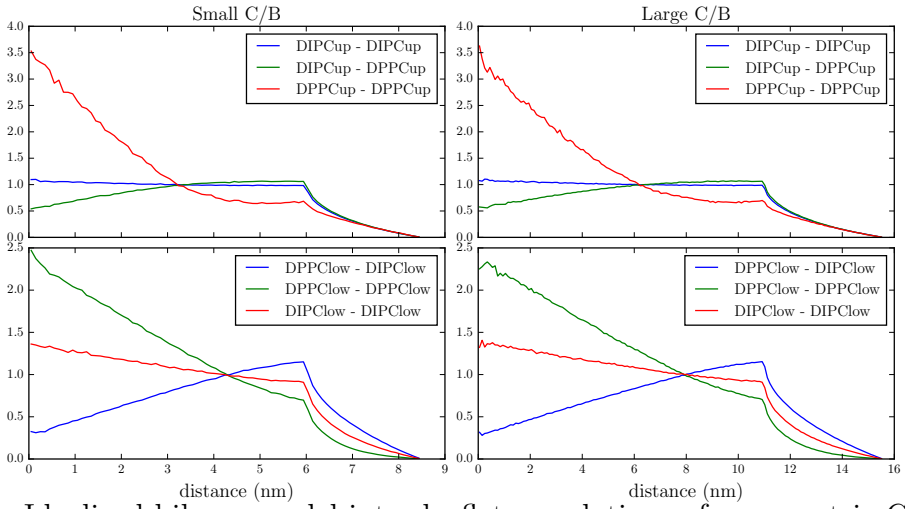


Figure 5.19: Idealized bilayer model inter-leaflet correlations of asymmetric C/B bilayers

# Chapter 6

# SUMMARY AND CONCLUSION

In this dissertation, we have presented our theoretical exploration of various aspects of lateral phase behavior and surface pattern formation of multicomponent lipid-bilayer membranes. In Chapter 2, we explored the lateral phase diagrams of rigid, undeformed spherical surfaces in different sizes. The statistical mechanical tool that we used, the extended Landau-Ginzburg model, was previously used only for the study of an infinitely large planar surface. We applied it to the spherical geometry of intrinsic finite size, which limits the number of domains a vesicle can accommodate on the surface. We calculated ground state phase diagrams in analytical and numerical ways, and used Monte Carlo simulations and phase indicators in spherical harmonic analysis to calculate thermal equilibrium phase diagrams at finite temperature. The effects of thermal fluctuations at finite temperature include the emergence of the heterogeneous microemulsion state, the separation of the triple point in the phase diagrams and the appearance of a new phase transition boundary between the microemulsion and two-phase coexistence, which is similar to a change in the planar surface case. Because of the intrinsic finite radius of a sphere, our new findings also include the finite size effects that significantly affect the phase diagrams, which resemble phase diagrams of the planar geometry when the radius is large and deviate from the planar case most prominently when the radius is small. A small vesicle favors homogeneous states, including a single homogeneous fluid and a coexistence of two homogeneous phases, over heterogeneities such as modulated phases and the microemulsion.

In Chapter 3, we developed a novel, model-free, mathematical relationship between a two-dimensional structure factor of a planar surface, which is usually modeled in simulations of membrane patches, and a three-dimensional structure factor of a spherical surface, which

is usually measured in scattering experiments of vesicles. To examine the validity of this relationship which quantitatively compares structure factors in different dimensionalities, we used a Gaussian model and the equipartition theorem to calculate the two- and three-dimensional structure factors of lipid membranes in planar and spherical geometries. Similar finite size effects as in Chapter 2 were found in the Gaussian model which illustrates either a homogeneous phase or a microemulsion. The mathematical relationship is shown to be exact for an infinitely large spherical surface, and is approximate for spheres of finite radius. We pointed out its limitation at very small system sizes, which should be considered when using this approximate relationship for quantitative comparison.

In Chapter 4, we considered a soft, deformable vesicular surface whose shape is coupled to surface composition. We combined the standard Landau-Ginzburg model and the Helfrich bending model, which was also applied in many previous theoretical studies. The shape-composition coupling in these previous theories, however, were mainly realized by including an additional coupling term in the free energy model. We used a distinct, more physically meaningful tactic, adding the curvature-composition coupling through the bending modulus and spontaneous curvature. We studied ground state phase diagrams of our coupling model which optionally includes a Gaussian bending term, and we found that different computation methods generate similar results, which are comparable to phase diagrams that are provided in existing literature and generated from the tactic of extra coupling term. In the phase diagrams, modulated phases are generated by the bending property mismatches between liquid-ordered and -disordered domains, which overcome the effect of interface line tension. We calculated the interface width and line tension at sample points and compared them with simulation and experimental values. We also discovered the existence of intermediate spiral phases between axisymmetric modulate phases, whose domain sizes and stripe widths change continuously through a spiral phase.

In addition to continuum modeling, in Chapter 5 we used coarse-grained molecular dynamics simulations to study the phase phenomena of asymmetric lipid bilayers, looking for a phase separation in one leaflet induced by the other leaflet. The simulation results showed

a domain anti-registration configuration in a phase-separating symmetric bilayer at a small size, and in-registration configuration at a large size, but we have not observed any visible induced phase separation in the asymmetric bilayers. However, inter-leaflet pair correlation functions revealed the existence of inter-leaflet coupling and an induced tendency of phase separation and domain formation in the naturally non-phase-separating leaflet when it is present in an asymmetric bilayer along with the phase-separating leaflet. This supplementary study, which is separate from the aforementioned modeling of vesicles, supports some previous observations in microscopy experiments and other molecular simulations.

Overall, we have seen how different simple theoretical models are able to describe a large variety of lateral phases and surface patterns, as well as phase transitions between them, in multicomponent lipid bilayers, especially lipid vesicles, as observed in experiments and molecular simulations. We have shown that the intrinsic finite size of a vesicle has a significant effect on the emergence of the phases and the distribution of them in a phase diagram. We stress the comparison between lipid membranes in different geometries (planar or spherical) in both qualitative and quantitative ways, e.g. by developing the approximate model-free mathematical relationship to compare structure factors. We also highlight the effect of curvature-composition coupling on the pattern formation of a vesicular surface, especially the generation of modulated phases in addition to homogeneous fluid and two-phase separation. All of these effects, caused by finite size, geometrical difference or shape-composition coupling, must be addressed whenever lateral phase behaviors of planar membranes, including surface morphological pattern and structure factor, are compared against those of vesicles.

# BIBLIOGRAPHY

[1] R. Phillips, J. Kondev, J. Theriot, and H. Garcia, *Physical Biology of the Cell*. Garland Science, 2nd ed., 2013.

[2] S. J. Singer and G. L. Nicolson, "The fluid mosaic model of the structure of cell membranes," *Science*, vol. 175, no. 4023, pp. 720–731, 1972.

[3] M. Deserno, "Fluid lipid membranes – a primer." https://www.cmu.edu/biolphys/deserno/pdf/membrane_theory.pdf, 2007.

[4] S. L. Veatch and S. L. Keller, "Separation of liquid phases in giant vesicles of ternary mixtures of phospholipids and cholesterol," *Biophys. J.*, vol. 85, pp. 3074–3083, 2003.

[5] S. L. Veatch and S. L. Keller, "Seeing spots: Complex phase behavior in simple membranes," *Biochim. Biophys. Acta – Molecular Cell Research*, vol. 1746, no. 3, pp. 172–185, 2005.

[6] D. Scherfeld, N. Kahya, and P. Schwille, "Lipid dynamics and domain formation in model membranes composed of ternary mixtures of unsaturated and saturated phosphatidylcholines and cholesterol," *Biophys. J.*, vol. 85, no. 6, pp. 3758–3768, 2003.

[7] D. Marsh, "Cholesterol–induced fluid membrane domains: A compendium of lipid–raft ternary phase diagrams," *Biochim. Biophys. Acta – Biomembranes*, vol. 1788, no. 10, pp. 2114–2123, 2009.

[8] J. R. Silvius, D. del Giudice, and M. Lafleur, "Cholesterol at different bilayer concentrations can promote or antagonize lateral segregation of phospholipids of differing acyl chain length," *Biochem.*, vol. 35, no. 48, pp. 15198–15208, 1996.

[9] T.-Y. Wang and J. R. Silvius, "Cholesterol does not induce segregation of liquid–ordered domains in bilayers modeling the inner leaflet of the plasma membrane," *Biophys. J.*, vol. 81, no. 5, pp. 2762–2773, 2001.

[10] S. L. Veatch, I. V. Polozov, K. Gawrisch, and S. L. Keller, "Liquid domains in vesicles investigated by NMR and fluorescence microscopy," *Biophys. J.*, vol. 86, no. 5, pp. 2910–2922, 2004.

[11] J. Zhao, J. Wu, F. A. Heberle, T. T. Mills, P. Klawitter, G. Huang, G. Costanza, and G. W. Feigenson, "Phase studies of model biomembranes: Complex behavior of DSPC/DOPC/Cholesterol," *Biochim. Biophys. Acta – Biomembranes*, vol. 1768, no. 11, pp. 2764–2776, 2007.

[12] F. A. Heberle, J. Wu, S. L. Goh, R. S. Petruzielo, and G. W. Feigenson, "Comparison of three ternary lipid bilayer mixtures: FRET and ESR reveal nanodomains," *Biophys. J.*, vol. 99, no. 10, pp. 3309–3318, 2010.

[13] D. I. Svergun and M. H. J. Koch, "Small–angle scattering studies of biological macromolecules in solution," *Rep. Prog. Phys.*, vol. 66, pp. 1735–1782, 2003.

[14] J. Pencer, T. Mills, V. Anghel, S. Krueger, R. M. Epand, and J. Katsaras, "Detection of submicron–sized raft–like domains in membranes by small–angle neutron scattering," *Eur. Phys. J. E*, vol. 18, no. 4, pp. 447–458, 2005.

[15] V. N. P. Anghel, N. Kučerka, J. Pencer, and J. Katsaras, "Scattering from laterally heterogeneous vesicles. II. the form factor," *J. Appl. Crystallogr.*, vol. 40, pp. 513–525, 2007.

[16] G. Pabst, N. Kučerka, M.-P. Nieh, M. C. Rheinstädter, and J. Katsaras, "Applications of neutron and X-ray scattering to the study of biologically relevant model membranes," *Chemistry and Physics of Lipids*, vol. 163, no. 6, pp. 460–479, 2010.

[17] B. Kollmitzer, P. Heftberger, R. Podgornik, J. F. Nagle, and G. Pabst, "Bending rigidities and interdomain forces in membranes with coexisting lipid domains," *Biophys. J.*, vol. 108, no. 12, pp. 2833–2842, 2015.

[18] D. Marquardt, F. A. Heberle, J. D. Nickels, G. Pabst, and J. Katsaras, "On scattered waves and lipid domains: detecting membrane rafts with X-rays and neutrons," *Soft Matter*, vol. 11, pp. 9055–9072, 2015.

[19] K. Simons and E. Ikonen, "Functional rafts in cell membranes," *Nature*, vol. 387, pp. 569–572, 1997.

[20] D. A. Brown and E. London, "Functions of lipid rafts in biological membranes," *Ann. Rev. Cell Dev. Biol.*, vol. 14, pp. 111–136, 1998.

[21] D. Lingwood and K. Simons, "Lipid rafts as a membrane–organizing principle," *Science*, vol. 327, no. 5961, pp. 46–50, 2010.

[22] A. Radhakrishnan and H. M. McConnell, "Condensed complexes in vesicles containing cholesterol and phospholipids," *Proc. Natl. Acad. Sci. USA*, vol. 102, no. 36, pp. 12662–12666, 2005.

[23] P. F. F. Almeida, "Thermodynamics of lipid interactions in complex bilayers," *Biochim. Biophys. Acta – Biomembranes*, vol. 1788, no. 1, pp. 72–85, 2009.

[24] G. G. Putzel and M. Schick, "Insights on raft behavior from minimal phenomenological models," *J. Phys. Cond. Mat.*, vol. 23, no. 28, p. 284101, 2011.

[25] J. A. Svetlovics, S. A. Wheaten, and P. F. Almeida, "Phase separation and fluctuations in mixtures of a saturated and an unsaturated phospholipid," *Biophys. J.*, vol. 102, no. 11, pp. 2526–2535, 2012.

[26] H. J. Risselada and S. J. Marrink, "The molecular face of lipid rafts in model membranes," *Proc. Natl. Acad. Sci. USA*, vol. 105, no. 45, pp. 17367–17372, 2008.

[27] C. Rosetti and C. Pastorino, "Polyunsaturated and saturated phospholipids in mixed bilayers: A study from the molecular scale to the lateral lipid organization," *J. Phys. Chem. B*, vol. 115, no. 5, pp. 1002–1013, 2011.

[28] C. Rosetti and C. Pastorino, "Comparison of ternary bilayer mixtures with asymmetric or symmetric unsaturated phosphatidylcholine lipids by coarse grained molecular dynamics simulations," *J. Phys. Chem. B*, vol. 116, no. 11, pp. 3525–3537, 2012.

[29] A. J. Sodt, M. L. Sandar, K. Gawrisch, R. W. Pastor, and E. Lyman, "The molecular structure of the liquid–ordered phase of lipid bilayers," *J. Am. Chem. Soc.*, vol. 136, no. 2, pp. 725–732, 2014.

[30] S. Baoukina, D. Rozmanov, and D. P. Tieleman, "Composition fluctuations in lipid bilayers," *Biophys. J.*, vol. 113, no. 12, pp. 2750–2761, 2017.

[31] G. A. Pantelopulos, T. Nagai, A. Bandara, A. Panahi, and J. E. Straub, "Critical size dependence of domain formation observed in coarse–grained simulations of bilayers composed of ternary lipid mixtures," *J. Chem. Phys.*, vol. 147, p. 095101, 2017.

[32] P. B. S. Kumar, G. Gompper, and R. Lipowsky, "Modulated phases in multicomponent fluid membranes," *Phys. Rev. E*, vol. 60, pp. 4610–4618, 1999.

[33] G. W. Feigenson, "Phase diagrams and lipid domains in multicomponent lipid bilayer mixtures," *Biochim. Biophys. Acta – Biomembranes*, vol. 1788, no. 1, pp. 47–52, 2009.

[34] T. M. Konyakhina, S. L. Goh, J. Amazon, F. A. Heberle, J. Wu, and G. W. Feigenson, "Control of a nanoscopic–to–macroscopic transition: Modulated phases in four–component DSPC/DOPC/POPC/Chol giant unilamellar vesicles," *Biophys. J.*, vol. 101, no. 2, pp. L8–L10, 2011.

[35] B. Palmieri and S. A. Safran, "Hybrid lipids increase the probability of fluctuating nanodomains in mixed membranes," *Langmuir*, vol. 29, no. 17, pp. 5246–5261, 2013.

[36] M. C. Rheinstädter and O. G. Mouritsen, "Small–scale structure in fluid cholesterol–lipid bilayers," *Curr. Op. in Coll. & Interf. Sci.*, vol. 18, no. 5, pp. 440–447, 2013.

[37] C. L. Armstrong, D. Marquardt, H. Dies, N. Kučerka, Z. Yamani, T. A. Harroun, J. Katsaras, A.-C. Shi, and M. C. Rheinstädter, "The observation of highly ordered domains in membranes with cholesterol," *PLoS One*, vol. 8, no. 6, p. e66162, 2013.

[38] S. L. Goh, J. J. Amazon, and G. W. Feigenson, "Toward a better raft model: modulated phases in the four–component bilayer, DSPC/DOPC/POPC/CHOL," *Biophys. J.*, vol. 104, no. 4, pp. 853–862, 2013.

[39] T. M. Konyakhina, J. Wu, J. D. Mastroianni, F. A. Heberle, and G. W. Feigenson, "Phase diagram of a 4–component lipid mixture: DSPC/DOPC/POPC/chol," *Biochim. Biophys. Acta – Biomembranes*, vol. 1828, no. 9, pp. 2204–2214, 2013.

[40] L. Toppozini, S. Meinhardt, C. L. Armstrong, Z. Yamani, N. Kučerka, F. Schmid, and M. C. Rheinstädter, "Structure of cholesterol in lipid rafts," *Phys. Rev. Lett.*, vol. 113, p. 228101, 2014.

[41] T. A. Enoki, F. A. Heberle, and G. W. Feigenson, "FRET detects the size of nanodomains for coexisting liquid–disordered and liquid–ordered phases," *Biophys. J.*, vol. 114, no. 8, pp. 1921–1935, 2018.

[42] F. A. Heberle, M. Doktorova, S. L. Goh, R. F. Standaert, J. Katsaras, and G. W. Feigenson, "Hybrid and nonhybrid lipids exert common effects on membrane raft size and morphology," *J. Am. Chem. Soc.*, vol. 135, no. 40, pp. 14932–14935, 2013.

[43] F. A. Heberle, R. S. Petruzielo, J. Pan, P. Drazba, N. Kučerka, R. F. Standaert, G. W. Feigenson, and J. Katsaras, "Bilayer thickness mismatch controls domain size in model membranes," *J. Am. Chem. Soc.*, vol. 135, no. 18, pp. 6853–6859, 2013.

[44] J. D. Nickels, X. Cheng, B. Mostofian, C. Stanley, B. Lindner, F. A. Heberle, S. Perticaroli, M. Feygenson, T. Egami, R. F. Standaert, J. C. Smith, D. A. A. Myles, M. Ohl, and J. Katsaras, "Mechanical properties of nanoscopic lipid domains," *J. Am. Chem. Soc.*, vol. 137, no. 50, pp. 15772–15780, 2015.

[45] D. G. Ackerman and G. W. Feigenson, "Multiscale modeling of four–component lipid mixtures: Domain composition, size, alignment, and properties of the phase interface," *J. Phys. Chem. B*, vol. 119, no. 11, pp. 4240–4250, 2015.

[46] S. He and L. Maibaum, "Identifying the onset of phase separation in quaternary lipid bilayer systems from coarse–grained simulations," *J. Phys. Chem. B*, vol. 122, no. 14, pp. 3961–3973, 2018.

[47] J. J. Amazon, S. L. Goh, and G. W. Feigenson, "Competition between line tension and curvature stabilizes modulated phase patterns on the surface of giant unilamellar vesicles: A simulation study," *Phys. Rev. E*, vol. 87, no. 2, p. 022708, 2013.

[48] J. J. Amazon and G. W. Feigenson, "Lattice simulations of phase morphology on lipid bilayers: Renormalization, membrane shape, and electrostatic dipole interactions," *Phys. Rev. E*, vol. 89, p. 022702, 2014.

[49] K. K. Sreeja, J. H. Ipsen, and P. B. S. Kumar, "Monte Carlo simulations of fluid vesicles," *J. Phys. Cond. Matt.*, vol. 27, p. 273104, 2015.

[50] T. Baumgart, A. T. Hammond, P. Sengupta, S. T. Hess, D. A. Holowka, B. A. Baird, and W. W. Webb, "Large–scale fluid/fluid phase separation of proteins and lipids in giant plasma membrane vesicles," *Proc. Natl. Acad. Sci. USA*, vol. 104, no. 9, pp. 3165–3170, 2007.

[51] S. L. Veatch, P. Cicuta, P. Sengupta, A. Honerkamp-Smith, D. Holowka, and B. Baird, "Critical fluctuations in plasma membrane vesicles," *Chem. Biol.*, vol. 3, no. 5, pp. 287–293, 2008.

[52] K. R. Levental and I. Levental, "Chapter two – giant plasma membrane vesicles: Models for understanding membrane organization," *Current Topics in Membranes*, vol. 75, pp. 25–57, 2015.

[53] S. P. Rayermann, G. E. Rayermann, C. E. Cornell, A. J. Merz, and S. L. Keller, "Hallmarks of reversible separation of living, unperturbed cell membranes into two liquid phases," *Biophys. J.*, vol. 113, no. 11, pp. 2425–2432, 2017.

[54] C. E. Cornell, A. D. Skinkle, S. He, I. Levental, K. R. Levental, and S. L. Keller, "Tuning length scales of small domains in cell–derived membranes and synthetic model membranes," *Biophys. J.*, vol. 115, no. 4, pp. 690–701, 2018.

[55] T. Taniguchi, "Shape deformation and phase separation dynamics of two–component vesicles," *Phys. Rev. Lett.*, vol. 76, pp. 4444–4447, 1996.

[56] Y. Hirose, S. Komura, and D. Andelman, "Concentration fluctuations and phase transitions in coupled modulated bilayers," *Phys. Rev. E*, vol. 86, p. 021916, 2012.

[57] I. A. B. Vidal, C. M. Rosetti, C. Pastorino, and M. Müller, "Measuring the composition–curvature coupling in binary lipid membranes by computer simulations," *J. Chem. Phys.*, vol. 141, p. 194902, 2014.

[58] G. Gueguen, N. Destainville, and M. Manghi, "Mixed lipid bilayers with locally varying spontaneous curvature and bending," *Eur. Phys. J. E*, vol. 37, p. 76, 2014.

[59] L. D. Landau and E. M. Lifshitz, *Statistical physics*, vol. 1. Elsevier, 3rd ed., 1980.

[60] R. J. Baxter, *Exactly Solved Models in Statistical Mechanics*. Academic Press, 1982.

[61] N. Goldenfeld, *Lectures on Phase Transitions and the Renormalization Group*. Perseus Books Publishing, 1992.

[62] S. A. Safran, *Statistical Thermodynamics of Surfaces, Interfaces and Membranes*. Addison–Wesley Publishing, 1994.

[63] A. J. Bray, "Theory of phase–ordering kinetics," *Adv. Phys.*, vol. 43, pp. 357–459, 1994.

[64] R. M. Hornreich, M. Luban, and S. Shtrikman, "Critical behavior at the onset of k-space instability on the lambda line," *Phys. Rev. Lett.*, vol. 35, p. 1678, 1975.

[65] M. Seul and D. Andelman, "Domain shapes and patterns: The phenomenology of modulates phases," *Science*, vol. 267, pp. 476–483, 1995.

[66] M. E. Gracheva, J. M. Rickman, and J. D. Gunton, "Coarse–grained Ginzburg–Landau free energy for Lennard–Jones systems," *J. Chem. Phys.*, vol. 113, no. 9, pp. 3525–3529, 2000.

[67] M. Invernizzi, O. Valsson, and M. Parrinello, "Coarse graining from variationally enhanced sampling applied to the Ginzburg–Landau model," *Proc. Natl. Acad. Sci. USA*, vol. 114, no. 13, pp. 3370–3374, 2017.

[68] M. O. Lavrentovich, E. M. Horsley, A. Radja, A. M. Sweeney, and R. D. Kamien, "First–order patterning transitions on a sphere as a route to cell morphology," *Proc. Natl. Acad. Sci. USA*, vol. 113, no. 19, pp. 5189–5194, 2016.

[69] A. Radja, E. M. Horsley, M. O. Lavrentovich, and A. M. Sweeney, "Pollen cell wall patterns form from modulated phases," *Cell*, vol. 176, no. 4, pp. 856–868, 2019.

[70] R. Shlomovitz, L. Maibaum, and M. Schick, "Macroscopic phase separation, modulated phases, and microemulsions: A unified picture of rafts," *Biophys. J.*, vol. 106, no. 9, pp. 1979–1985, 2014.

[71] K. Sapp, R. Shlomovitz, and L. Maibaum, "Seeing the forest in lieu of the trees: Continuum simulations of cell membranes at large length scales," in *Annual Reports in Computational Chemistry* (R. A. Wheeler, ed.), vol. 10, (Amsterdam), pp. 47–76, Elsevier, 2014.

[72] L. J. Pike, "Rafts defined: A report on the Keystone symposium on lipid rafts and cell function," *J. Lip. Res.*, vol. 47, pp. 1597–1598, 2006.

[73] E. L. Elson, E. Fried, J. E. Dolbow, and G. M. Genin, "Phase separation in biological membranes: Integration of theory and experiment," *Ann. Rev. Biophys.*, vol. 39, p. 207, 2010.

[74] M. Schick, "Membrane heterogeneity: Manifestation of a curvature–induced microemulsion," *Phys. Rev. E*, vol. 85, p. 031902, 2012.

[75] R. Shlomovitz and M. Schick, "Model of a raft in both leaves of an asymmetric lipid bilayer," *Biophys. J.*, vol. 105, pp. 1406–1413, 2013.

[76] S. Komura and D. Andelman, "Physical aspects of heterogeneities in multi–component lipid membranes," *Adv. Colloid Interface Sci.*, vol. 208, pp. 34–46, 2014.

[77] F. Schmid, "Physical mechanisms of micro– and nanodomain formation in multicomponent lipid membranes," *Biochim. Biophys. Acta – Biomembranes*, vol. 1859, no. 4, pp. 509–528, 2017.

[78] K. Binder, "Finite size scaling analysis of Ising model block distribution functions," *Z. Phys. B*, vol. 43, no. 2, pp. 119–140, 1981.

[79] K. K. Mon and K. Binder, "Finite size effects for the simulation of phase coexistence in the Gibbs ensemble near the critical point," *J. Chem. Phys.*, vol. 96, pp. 6989–6995, 1992.

[80] J.-P. Hansen and I. R. McDonald, *Theory of Simple Liquids*. Academic Press, 4th ed., 2013.

[81] J.-M. Y. Carrillo, J. Katsaras, B. G. Sumpter, and R. Ashkar, "A computational approach for modeling neutron scattering data from lipid bilayers," *J. Chem. Theo. Comp.*, vol. 13, no. 2, pp. 916–925, 2017.

[82] J. D. Nickels, M. D. Smith, R. J. Alsop, S. Himbert, A. Yahya, D. Cordner, P. Zolnierczuk, C. B. Stanley, J. Katsaras, X. Cheng, and M. C. Rheinstädter, "Lipid rafts: Buffers of cell membrane physical properties," *J. Phys. Chem. B*, vol. 123, no. 9, pp. 2050–2056, 2019.

[83] W. Helfrich, "Elastic properties of lipid bilayers – Theory and possible experiments," *Z. Naturforsch.*, vol. C 28, pp. 693–703, 1973.

[84] H. Engelhardt, H. P. Duwe, and E. Sackmann, "Bilayer bending elasticity measured by Fourier analysis of thermally excited surface undulations of flaccid vesicles," *J. Physique Lett.*, vol. 46, pp. 395–400, 1985.

[85] S. T. Milner and S. A. Safran, "Dynamical fluctuations of droplet microemulsions and vesicles," *Phys. Rev. A*, vol. 36, pp. 4371–4379, 1987.

[86] F. L. H. Brown, "Elastic modeling of biomembranes and lipid bilayers," *Ann. Rev. Phys. Chem.*, vol. 59, pp. 685–712, 2008.

[87] M. Deserno, "Fluid lipid membranes: From differential geometry to curvature stresses," *Chem. Phys. Lipids*, vol. 185, pp. 11–45, 2015.

[88] H. Jiang and T. R. Powers, "Curvature–driven lipid sorting in a membrane tubule," *Phys. Rev. Lett.*, vol. 101, p. 018103, 2008.

[89] Y. Sakuma, N. Urakami, T. Taniguchi, and M. Imai, "Asymmetric distribution of cone–shaped lipids in a highly curved bilayer revealed by a small angle neutron scattering technique," *J. Phys. Cond. Matt.*, vol. 23, no. 28, p. 284104, 2011.

[90] A. Callan-Jones, B. Sorre, and P. Bassereau, "Curvature–driven lipid sorting in biomembranes," *Cold Spring Harb. Perspect. Biol*, vol. 3, no. 2, p. a004648, 2011.

[91] T. Baumgart, S. T. Hess, and W. W. Webb, "Imaging coexisting fluid domains in biomembrane models coupling curvature and line tension," *Nature*, vol. 425, pp. 821–824, 2003.

[92] S. F. Shimobayashi, M. Ichikawa, and T. Taniguchi, "Direct observations of transition dynamics from macro- to micro-phase separation in asymmetric lipid bilayers induced by externally added glycolipids," *Europhys. Lett.*, vol. 113, no. 5, p. 56005, 2016.

[93] T. Kawakatsu, D. Andelman, K. Kawasaki, and T. Taniguchi, "Phase transitions and shapes of two component membranes and vesicles I: strong segregation limit," *J. Phys. II (France)*, vol. 3, pp. 971–997, 1993.

[94] T. Taniguchi, K. Kawasaki, D. Andelman, and T. Kawakatsu, "Phase transitions and shapes of two component membranes and vesicles II: weak segregation limit," *J. Phys. II (France)*, vol. 4, no. 8, pp. 1333–1362, 1994.

[95] O. Schönborn and R. C. Desai, "Phase–ordering kinetics on curved surfaces," *Physica A*, vol. 239, pp. 412–419, 1997.

[96] A. Saxena and T. Lookman, "Kinetics of phase separation on curved manifolds: soft matter," *Physica D*, vol. 133, no. 1–4, pp. 416–426, 1999.

[97] V. Kiessling, C. Wan, and L. K. Tamm, "Domain coupling in asymmetric lipid bilayers," *Biochim. Biophys. Acta*, vol. 1788, no. 1, pp. 64–71, 2009.

[98] L. Tayebi, Y. Ma, D. Vashaee, G. Chen, S. K. Sinha, and A. N. Parikh, "Long–range interlayer alignment of intralayer domains in stacked lipid bilayers," *Nature Materials*, vol. 11, pp. 1074–1080, 2012.

[99] T. Hoshino, S. Komura, and D. Andelman, "Correlated lateral phase separations in stacks of lipid membranes," *J. Chem. Phys.*, vol. 143, p. 243124, 2015.

[100] F. A. Heberle, D. Marquardt, M. Doktorova, B. Geier, R. F. Standaert, P. Heftberger, B. Kollmitzer, J. D. Nickels, R. A. Dick, G. W. Feigenson, J. Katsaras, E. London, and G. Pabst, "Subnanometer structure of an asymmetric model membrane: Interleaflet coupling influences domain properties," *Langmuir*, vol. 32, no. 20, pp. 5195–5200, 2016.

[101] I. S. Vinklárek, L. Vel'as, P. Riegerová, K. Skála, I. Mikhalyov, N. Gretskaya, M. Hof, and R. Šachl, "Experimental evidence of the existence of interleaflet coupled nanodomains: An MC–FRET study," *J. Phys. Chem. Lett.*, vol. 10, no. 9, pp. 2024–2030, 2019.

[102] J. D. Perlmutter and J. N. Sachs, "Interleaflet interaction and asymmetry in phase separated lipid bilayers: Molecular dynamics simulations," *J. Am. Chem. Soc.*, vol. 133, no. 17, pp. 6563–6577, 2011.

[103] P. W. Fowler, J. J. Williamson, M. S. P. Sansom, and P. D. Olmsted, "Roles of interleaflet coupling and hydrophobic mismatch in lipid membrane phase–separation kinetics," *J. Am. Chem. Soc.*, vol. 138, no. 36, pp. 11633–11642, 2016.

[104] M. D. Collins and S. L. Keller, "Tuning lipid mixtures to induce or suppress domain formation across leaflets of unsupported asymmetric bilayers," *Proc. Natl. Acad. Sci. USA*, vol. 105, no. 1, pp. 124–128, 2008.

[105] M. D. Weiner and G. W. Feigenson, "Molecular dynamics simulations reveal leaflet coupling in compositionally asymmetric phase–separated lipid membranes," *J. Phys. Chem. B*, vol. 123, no. 18, pp. 3968–3975, 2019.

[106] Y. Luo and L. Maibaum, "Phase diagrams of multicomponent lipid vesicles: Effects of finite size and spherical geometry," *J. Chem. Phys.*, vol. 149, p. 174901, 2018.

[107] Q. Wang, O. Ronneberger, and H. Burkhardt, "Fourier analysis in polar and spherical coordinates," 2008. Technical Report 1, IIF-LMB, Computer Science Department, University of Freiburg.

[108] R. N. Bracewell, *The Fourier Transform and Its Applications*. McGraw–Hill, 3rd ed., 2000.

[109] Y. Luo and L. Maibaum, "Relating the structure factors of two–dimensional materials in planar and spherical geometries," *Soft Matter*, vol. 14, pp. 5686–5692, 2018.

[110] "NIST digital library of mathematical functions." http://dlmf.nist.gov/, Release 1.0.18 of 2018–03–27. F. W. J. Olver, A. B. Olde Daalhuis, D. W. Lozier, B. I. Schneider, R. F. Boisvert, C. W. Clark, B. R. Miller and B. V. Saunders, eds.

[111] M. A. Wieczorek, M. Meschede, E. S. de Andrade, I. Oshchepkov, B. Xu, and A. Walker, "SHTOOLS: Version 4.2, Zenodo." doi:10.5281/zenodo.1067108, 2017.

[112] S. A. Brazovskii, "Phase transition of an isotropic system to a nonuniform state," *Zh. Eksp. Teor. Fiz.*, vol. 68, no. 1, pp. 175–185, 1975.

[113] N. A. Gross, M. Ignatiev, and B. Chakraborty, "Kinetics of ordering in fluctuation–driven first–order transitions: Simulation and theory," *Phys. Rev. E*, vol. 62, no. 5, p. 6116, 2000.

[114] G. Gompper and M. Schick, "Correlation between structural and interfacial properties of amphiphilic systems," *Phys. Rev. Lett.*, vol. 65, no. 9, pp. 1116–1119, 1990.

[115] E. D. Mitra, S. C. Whitehead, D. Holowka, B. Baird, and J. P. Sethna, "Computation of a theoretical membrane phase diagram and the role of phase in lipid–raft–mediated protein organization," *J. Phys. Chem. B*, vol. 122, no. 13, pp. 3500–3513, 2018.

[116] C. E. Cornell, N. L. C. McCarthy, K. R. Levental, I. Levental, N. J. Brooks, and S. L. Keller, "n-alcohol length governs shift in Lo–Ld mixing temperatures in synthetic and cell–derived membranes," *Biophys. J.*, vol. 113, no. 6, pp. 1200–1211, 2017.

[117] C. Esposito, A. Tian, S. Melamed, C. Johnson, S.-Y. Tee, and T. Baumgart, "Flicker spectroscopy of thermal lipid bilayer domain boundary fluctuations," *Biophys. J.*, vol. 93, no. 9, pp. 3169–3181, 2007.

[118] P. B. Canham, "The minimum energy of bending as a possible explanation of the biconcave shape of the red blood cell," *J. Theor. Biol.*, vol. 26, pp. 61–81, 1970.

[119] D. J. Smith, J. B. Klauda, and A. J. Sodt, "Simulation best practices for lipid membranes [article v1.0]," *Living J. Comp. Mol. Sci.*, vol. 1, no. 1, p. 5966, 2019.

[120] S. J. Marrink, H. J. Risselada, S. Yefimov, D. P. Tieleman, and A. H. de Vries, "The MARTINI force field: Coarse grained model for biomolecular simulations," *J. Phys. Chem. B*, vol. 111, no. 27, pp. 7812–7824, 2007.

[121] "Gromacs Molecular Dynamics package." http://www.gromacs.org.

[122] C. Arnarez, J. J. Uusitalo, M. F. Masman, H. I. Ingolfsson, D. H. de Jong, M. N. Melo, X. Periole, A. H. de Vries, and S. J. Marrink, "Dry Martini, a coarse–grained force field for lipid membrane simulations with implicit solvent," *J. Chem. Theo. Comp.*, vol. 11, no. 1, pp. 260–275, 2015.

[123] A. Srivastava and G. A. Voth, "Hybrid approach for highly coarse–grained lipid bilayer models," *J. Chem. Theo. Comp.*, vol. 9, no. 1, pp. 750–765, 2013.

[124] J.-M. Drouffe, A. C. Maggs, and S. Leibler, "Computer simulations of self–assembled membranes," *Science*, vol. 254, no. 5036, pp. 1353–1356, 1991.

[125] A. Pasqua, L. Maibaum, G. Oster, D. A. Fletcher, and P. L. Geissler, "Large–scale simulations of fluctuating biological membranes," *J. Chem. Phys.*, vol. 132, p. 154107, 2010.